eman ta zabal zazu

Universidad del País Vasco
Euskal Herriko Unibertsitatea

Computational methods to solve many-body problems from first principles: a focus on the electron-phonon interaction

A thesis submitted to the
University of the Basque Country
to obtain the degree of Doctor in Physics by

Jon Lafuente Bartolomé

Supervised by

Dr. Asier Eiguren Goienetxea
and
Dr. Idoia García de Gurtubay Gálligo

October 2020

Contents

Introduction

Computational physics is the scientific discipline that creates, develops and implements numerical algorithms to solve problems in Physics for which a quantitative theory already exists.

The fundamental physical theory which describes the behavior of matter at the microscopic scale is quantum mechanics. The problem of determining a given property of a material, once its chemical composition is known, can be formally traced back to the problem of solving the corresponding many-body Schrödinger equation for the interacting electrons and nuclei. In this respect, the fundamental theory underlying any many-body problem exists and is known.

Both the difficulty and the beauty in this kind of problems lie in its *many* constituents. Most of the properties that we observe result from the interactions among the huge number of electrons and nuclei by which a macroscopic piece of any material is formed. Nonetheless, it is its microscopic atomic composition what ultimately shapes its behavior. Therefore, a completely general method which aims to predict the characteristics of any material has to begin from the quantum mechanical description of its underlying atomic structure, that is, from first principles. However, even if a complete understanding of the isolated atom is at hand, it is hopeless to try and deduce from that knowledge only, for instance, whether the corresponding elemental solid will be an insulator, a metal or a superconductor at a given temperature. The interactions among the atomic constituents have to be included in the theory, and this makes the direct solution of the problem impossible.

In this context, it is the task of computational condensed-matter physicists to develop theoretical schemes in which these many-body interactions are converted into tractable problems, and to provide algorithms which numerically solve these problems as efficiently as possible. From the practical implementation and execution of these algorithms, insight into already measured experimental phenomena can be gained, new interesting emergent physical effects can be predicted, and eventually novel materials with interesting properties can be virtually designed on a computer, before they are actually synthesized in a laboratory.

The enormous progress that this field has witnessed during the last years can hardly be overstated. This is mainly due to the outstanding methodological advances that have been put forward to describe materials properties at the quantum-mechanical level, together with the exponential increase of computing power provided by the modern hardware and software technologies. At present, first principles calculations are routinely performed on a daily basis, providing accurate predictions about complex properties of diverse materials. However, the more intricate the interactions in the system one wants to analyze are, the more challenging the prediction of its properties is, since it becomes more difficult to adopt simplifying assumptions that account for those interactions while maintaining a quantitative accuracy.

In this respect, a detailed description of the coupling between the electrons and the atomic vibrations — i.e. the electron-phonon interaction — stands for one of the biggest challenges in the history of computational condensed-matter physics. The crucial role played by the electron-phonon interaction in diverse observable phenomena such as the temperature dependence of carrier mobility and the optical absorption in semiconductors, or the electrical resistivity and even the conventional superconductivity in metals, has led to a persistent effort to model this physical process ever since the early days of the quantum theory of solids [1, 2]. However, although a rigorous field-theoretical formalism accounting for this many-body interaction was already developed more than half a century ago [3–6], it has been only very recently possible to include electron-phonon interactions in quantitative first principles calculations of complex materials properties [7], owing to the large computational effort required to accurately model this process.

The efficient numerical methods developed during the last years [8–11] have boosted tremendously the accuracy of theoretical studies on electron-phonon driven phenomena measured in experiments, such as quasiparticle renormalization signatures in angle resolved photoemission spectra [12–14], non-adiabatic corrections to phonon dispersions [15–18], or gap anisotropy in phonon-mediated superconductors [19, 20]. However, as the comparison between theory and experiment gets more refined, and with the ambition of exploring novel effects involving electron-phonon interactions in increasingly complex materials, new theoretical and methodological advances are still much needed in this field.

In this thesis, we develop and implement several numerical methods to solve, from first principles, different many-body problems related to the electron-phonon interaction in solids. Our methods allow us to get detailed physical insight into existing experimental results, and occasionally even to predict new effects, at a remarkably reduced computational effort as compared to state-of-the-art approaches. Most importantly, as the range of applicability of the developed techniques goes beyond what is explored in this thesis, this work opens interesting prospects in different branches of computational many-body physics.

The main part of this thesis is organized as follows. Chapter 1 reviews the general theoretical framework on which the developed methods and the discussed physics are based, namely the self-consistent many-body theory of electron-phonon interactions through Green's function techniques and Density Functional Theory. Short notes on the extension of the formalism to describe the superconducting state are given in Appendix A.

From this many-body formalism it appears clear that the self-consistent response of the electron density to the atomic displacements plays a crucial role in the theory of the electron-phonon interaction. In Chapter 2, we analyze in more detail several generally overlooked aspects of the electronic response. For that purpose, we implement an interpolation technique to efficiently compute the density-response function at surfaces and low dimensional systems, focusing on the real-space structure of the possible electronic collective excitations that may exist in the system. Our scheme allows us to study numerically, for the first time, the general spinorial structure of the electronic response induced by the spin-orbit coupling at surfaces with strong relativistic corrections. Moreover, by applying our methodology to the Tl/Si(111) surface, we show the existence of a novel coupled spin-charge plasmon localized at surfaces with spin-polarized states.

In Chapter 3, we dig into the subtleties of the renormalization of electron quasiparticles driven by their interaction with phonons. We start from a rigorous account of the definition of quasiparticles within the Green's function formalism, showing the mathematical complexities of the determination of their renormalized energies and spectral weights on the complex-energy plane. Then, starting from simplified models, we extend existing approaches by which the analytic continuation of a general self-energy can be numerically obtained, a necessary step to properly solve the quasiparticle equation. We apply our methodology to the doped monolayer MoS2, and unambiguously identify strongly renormalized quasiparticles that underpin the intricate spectral features reported in very recent experimental measurements performed on this system.

The electron-phonon interaction is usually anisotropic in momentum space, but is restricted to a narrow energy window around the Fermi surface. This poses a particularly challenging problem from a numerical point of view, since conventional techniques require samplings of up to millions of points in the Brillouin zone to accurately describe this many-body interaction. In Chapter 4, we demonstrate the potential of the Helmholtz Fermi Surface Harmonics basis set to reduce, in several orders of magnitude, the computational effort to solve electron-phonon problems defined on the Fermi surface. In the first part of the chapter, we implement a numerical procedure to incorporate the symmetries of the crystal in the basis set. In the second part, we apply the methodology to solve the anisotropic Eliashberg equations of superconductivity in this new representation, showing that the anisotropic superconducting gap and transition temperature of phonon-mediated super-

conductors can be accurately determined by a handful of symmetric elements of the set. The results reported in this chapter pave the way towards the application of the Helmholtz Fermi Surface Harmonics basis set in diverse problems involving many-body interactions on the Fermi surface.

On a final note, in Chapter 5 we review the main results obtained in this thesis and draw the most important conclusions. We also outline a number research directions opened by combining the methodologies developed in the different chapters and beyond.

Chapter 1

Theoretical background

In this first chapter, we introduce the general theoretical concepts and methods on which the next chapters rely. The theoretical formulation of the electron-phonon problem has a long history of development, and has been the subject of several authoritative books and review articles [6, 7, 21, 22]. It is not our aim here to add new pieces to the existing formulation, but to cover the main points as comprehensively and concisely as possible. More detailed derivations and discussions can be found in the references cited above.

Following the spirit of this thesis, we will start from the most general presentation of the problem, and go through the necessary steps and approximations to get to the final expressions, which will be ultimately implemented in the actual calculations presented in the next chapters.

1.1 General Hamiltonian for solids

The most general non-relativistic Hamiltonian for a system of interacting electrons and nuclei can be written as[1],

$$\hat{H} = \hat{T}_{\rm e} + \hat{T}_{\rm n} + \hat{U}_{\rm ee} + \hat{U}_{\rm nn} + \hat{U}_{\rm en} \ , \tag{1.1}$$

where the separate contributions are: *i)* the electronic kinetic energy,

$$\hat{T}_{\rm e} = -\frac{1}{2} \int d\mathbf{x}\, \hat{\Psi}^{\dagger}(\mathbf{x})\, \nabla^2\, \hat{\Psi}(\mathbf{x}) \ , \tag{1.2}$$

ii) the nuclear kinetic energy,

$$\hat{T}_{\rm n} = -\sum_{\kappa\alpha p} \frac{1}{2M_\kappa} \frac{\partial^2}{\partial \tau^2_{\kappa p\alpha}} \ , \tag{1.3}$$

[1] Unless otherwise stated, Hartree atomic units will be used throughout this thesis, i.e. $m_{\rm e} = e = \hbar = 4\pi\epsilon_0 = 1$.

iii) the electron-electron interaction,

$$\hat{U}_{\rm ee} = \frac{1}{2}\int d\mathbf{r}\int d\mathbf{r}'\, \hat{n}_{\rm e}(\mathbf{r})\left[\hat{n}_{\rm e}(\mathbf{r}') - \delta(\mathbf{r}-\mathbf{r}')\right] v(\mathbf{r},\mathbf{r}')\ , \tag{1.4}$$

iv) the nucleus-nucleus interaction,

$$\hat{U}_{\rm nn} = \frac{1}{2}\sum_{\kappa' p' \neq \kappa p} Z_\kappa Z_{\kappa'}\, v(\boldsymbol{\tau}^0_{\kappa p} + \Delta\hat{\boldsymbol{\tau}}_{\kappa p}, \boldsymbol{\tau}^0_{\kappa' p'} + \Delta\hat{\boldsymbol{\tau}}_{\kappa' p'})\ , \tag{1.5}$$

v) and the electron-nucleus interaction,

$$\hat{U}_{\rm en} = \int d\mathbf{r}\int d\mathbf{r}'\, \hat{n}_{\rm e}(\mathbf{r})\hat{n}_{\rm n}(\mathbf{r}')v(\mathbf{r},\mathbf{r}')\ . \tag{1.6}$$

In the above expressions, $v(\mathbf{r},\mathbf{r}') = 1/|\mathbf{r}-\mathbf{r}'|$ is the Coulomb interaction, the integrals $\int d\mathbf{x} = \sum_\sigma \int d\mathbf{r}$ denote sum over spin and integration over space, and the spatial integrals are over the entire crystal. α represents a spatial coordinate, and κ denotes a nucleus in the unit cell p, whose atomic number is Z_κ. The equilibrium coordinates of the nuclei are represented by $\boldsymbol{\tau}^0_{\kappa p}$, and the displacement of nuclei with respect to the equilibrium positions is considered as a dynamical variable, whose quantization yields the operator $\Delta\hat{\boldsymbol{\tau}}$. The electronic field creation and destruction operators are represented by $\hat{\Psi}^\dagger(\mathbf{r})$ and $\hat{\Psi}(\mathbf{r})$ respectively. Finally, the electron and nuclear density operators are defined, respectively, as,

$$\hat{n}_{\rm e}(\mathbf{r}) = \sum\nolimits_\sigma \hat{\Psi}^\dagger(\mathbf{r})\hat{\Psi}(\mathbf{r}), \tag{1.7}$$

$$\hat{n}_{\rm n}(\mathbf{r}) = -\sum\nolimits_{\kappa p} Z_\kappa\, \delta(\mathbf{r} - \boldsymbol{\tau}^0_{\kappa p} - \Delta\hat{\boldsymbol{\tau}}_{\kappa p})\ . \tag{1.8}$$

We now introduce the first important approximation used throughout this thesis, in which it is assumed that the displacements of the nuclei with respect to the equilibrium positions are small. In this way, we can expand the delta functions in Eq. (1.8) to second order in the displacements $\Delta\hat{\boldsymbol{\tau}}_{\kappa p}$, so that the nuclear density operator of Eq. (1.8) takes the form,

$$\begin{aligned}\hat{n}_{\rm n}(\mathbf{r}) \approx\ & n^0_{\rm n}(\mathbf{r}) + \sum\nolimits_{\kappa p} Z_\kappa\, \Delta\hat{\boldsymbol{\tau}}_{\kappa p}\cdot\nabla\delta(\mathbf{r}-\boldsymbol{\tau}^0_{\kappa p}) \\ & - \frac{1}{2}\sum\nolimits_{\kappa p} Z_\kappa\, \Delta\hat{\boldsymbol{\tau}}_{\kappa p}\cdot\nabla\nabla\delta(\mathbf{r}-\boldsymbol{\tau}^0_{\kappa p})\cdot\Delta\hat{\boldsymbol{\tau}}_{\kappa p},\end{aligned} \tag{1.9}$$

where $n^0_{\rm n}(\mathbf{r})$ is the density of nuclear point charges at the classical equilibrium positions $\boldsymbol{\tau}^0_{\kappa p}$. Plugging this expression into Eqs. (1.5),(1.6), we obtain the complete electron-nuclei Hamiltonian in the so-called harmonic approximation.

1.2 Many-body theory: electron and phonon Green's functions

The Hamiltonian presented in Eq. (1.1) contains the whole many-body problem of solids. If one was able to solve its corresponding Schrödinger equation, all the information about the system under study would be in principle contained in its eigenfunctions and eigenvalues. Unfortunately, it is well-known that this problem is impossible to solve directly except for extremely simple systems. Moreover, even if the complete many-body wave functions were available, emergent properties such as phonon modes or the superconducting state would be hopelessly hidden in the complicated solution.

The development of many-body physics has shown that it is much more convenient to work with the Green's functions drawn from quantum field theory, as they contain most of the relevant information related to observable properties in experiments. For example, the ground state energy, the spin and charge densities, and the excitation spectrum of the system can be directly determined from the single-particle Green's function [23].

The time-ordered one-electron Green's function is formally defined at zero temperature as,

$$G(\mathbf{x}t, \mathbf{x}'t') = -i\langle\, \hat{T}\, \hat{\Psi}(\mathbf{x}t)\hat{\Psi}^\dagger(\mathbf{x}'t')\,\rangle\ , \tag{1.10}$$

where brackets indicate an average over the many-body ground state, and $\hat{T}$ is the time-ordering operator, so that Eq. (1.10) can be separated in two contributions [23],

$$G(\mathbf{x}t, \mathbf{x}'t') = -\, i\theta(t-t')\langle\, \hat{\Psi}(\mathbf{x}t)\hat{\Psi}^\dagger(\mathbf{x}'t')\,\rangle \tag{1.11a}$$

$$+\, i\theta(t'-t)\langle\, \hat{\Psi}^\dagger(\mathbf{x}'t')\hat{\Psi}(\mathbf{x}t)\,\rangle\ . \tag{1.11b}$$

Physically, Eq. (1.11a) gives the probability amplitude for finding an electron in the position $\mathbf{x}$ and time t, after having added an electron in position $\mathbf{x}'$ and time t'. Similarly, Eq. (1.11b) describes the propagation of an extra hole from position $\mathbf{x}$ to $\mathbf{x}'$ in the time lapse from t to t'.

The exact Green's functions are not easier to determine than the original wave functions. However, it is much simpler to make physically transparent approximations — and in particular perturbative expansions — for their practical calculation. In this thesis, we follow the functional differentiation technique [24], applied for the first time to the interacting electron-phonon problem in the seminal works by Hedin [25] and Baym [4], and reviewed in Ref. [6] and more recently in Ref. [7].

The main idea behind this technique is to add an external probing field to the system which will be set to zero at the end of the derivation. The

Description	Expression	
Equation of motion, electrons	$\left[i\partial/\partial t_1 + \nabla^2(1)/2 - V_{\rm tot}(1)\right] G(12)$ $- \int d3\, \Sigma(13) G(32) = \delta(12)$	(1.12)
Electron self-energy	$\Sigma(12) = i \int d(34)\, G(13)\, \Gamma(324)$ $\times \left[W_{\rm e}(41^+) + W_{\rm ph}(41^+)\right]$	(1.13)
Vertex function	$\Gamma(123) = \delta(12)\delta(13) + \int d(4567)$ $\times \left[\partial\Sigma(12)/\partial G(45)\right] G(46) G(75) \Gamma(673)$	(1.14)
Screened Coulomb, phonons	$W_{\rm ph}(12) = \sum_{\kappa\alpha p, \kappa'\alpha' p'} \int d(34) \epsilon_{\rm e}^{-1}(13) \nabla_{3,\alpha} V_\kappa(\mathbf{r}_3 - \boldsymbol{\tau}^0_{\kappa p})$ $\times D_{\kappa\alpha p, \kappa'\alpha' p'}(t_3 t_4)$ $\times \epsilon_{\rm e}^{-1}(24) \nabla_{4,\alpha'} V_{\kappa'}(\mathbf{r}_4 - \boldsymbol{\tau}^0_{\kappa' p'})$	(1.15)
Screened Coulomb, electrons	$W_{\rm e}(12) = v(12) + \int d(34)\, v(13) P_{\rm e}(34) W_{\rm e}(42)$	(1.16)
Electronic polarization	$P_{\rm e}(12) = -i\hbar \sum_{\sigma_1} \int d(34)\, G(13)\, G(41^+)\, \Gamma(342)$	(1.17)
Electronic dielectric matrix	$\epsilon_{\rm e}(12) = \delta(12) - \int d(3) v(13) P_{\rm e}(32)$	(1.18)

Table 1.1. Hedin equations for electrons in a vibrating lattice. Additional equations for the displacement-displacement correlation function D are needed to obtain the full self-consistent Hedin-Baym equations. Adapted from Ref. [7] .

functional derivatives with respect to the probing field, however, may be nonzero, and appear very useful to derive a set of coupled nonlinear equations starting from the equation of motion for the electron and displacement operators. The derivation is rather lengthy and will not be followed here. Instead, we summarize in Table 1.1 the set of equations which determine the electron Green's function[2]. In Eq. (1.12), $V_{\rm tot}(1) = \int d2\, v(12)\, \langle \hat{n}(2) \rangle$ is the total electrostatic potential, where $\langle \hat{n}(2) \rangle = \langle \hat{n}_{\rm e}(2) \rangle + \langle \hat{n}_{\rm n}(2) \rangle$ is the expectation value of the total density operator.

The phonon contribution to the electron self-energy, a central theme in this thesis, is contained in Eq. (1.15). Here, $V_\kappa(\mathbf{r}) = -Z_\kappa/|\mathbf{r}|$ is the bare Coulomb potential of a nucleus κ. Most importantly, we introduced a displacement-displacement correlation function,

$$D_{\kappa p\alpha,\kappa' p'\alpha'}(t,t') = -i \langle\, \hat{T}\, \Delta\hat{\tau}_{\kappa p\alpha}(t)\, \Delta\hat{\tau}_{\kappa' p'\alpha'}(t') \,\rangle \;, \tag{1.19}$$

which provides all the relevant information about the phonon excitations in the system. In order to obtain a full self-consistent set of equations for the coupled electron-phonon system, an equation of motion and a self-energy have to be introduced for D, similar to Eqs. (1.12),(1.13) for G [4, 26]. As the focus of this thesis is put on electronic properties, we will not pursue this full self-consistency, and an adiabatic approximation will be used for the determination of D.

Within this approximation, the phonon self-energy is equivalent to the interatomic force constants one obtains through the Hellman-Feynman theorem [8]. As a result, the Fourier transform of the adiabatic displacement-displacement correlation function takes a particularly simple form in terms of the eigenvalues $\omega_{\mathbf{q}\nu}$ and the eigenvectors $e_{\kappa\alpha,\mathbf{q}\nu}$ of the dynamical matrix [6],

$$D^{\rm A}_{\kappa p\alpha,\kappa' p'\alpha'}(\omega) = \sum_\nu \int \frac{d\mathbf{q}}{\Omega_{\rm BZ}}\, \frac{D^{\rm A}_{\mathbf{q}\nu\nu'}(\omega)}{2M_\kappa \omega_{\mathbf{q}\nu}}\, e_{\kappa\alpha,\mathbf{q}\nu}\, e^*_{\kappa'\alpha',\nu}(\mathbf{q})\, e^{i\mathbf{q}\cdot(\mathbf{R}_p - \mathbf{R}_{p'})} \;, \tag{1.20}$$

where $\mathbf{R}_p$ denotes the lattice vector of the unit cell p, and where we have defined,

$$D^{\rm A}_{\mathbf{q}\nu\nu'}(\omega) = \frac{2\,\omega_{\mathbf{q}\nu}}{\omega^2 - \omega^2_{\mathbf{q}\nu}} \delta_{\nu\nu'} \;. \tag{1.21}$$

Finally, the inverse Fourier transform of Eq. (1.21) can be directly identified with a phonon Green's function, similar to Eq. (1.10),

$$D^{\rm A}_{\mathbf{q}\nu\nu'}(tt') = -i\langle \hat{T}\, [\hat{a}^\dagger_{\mathbf{q}\nu}(t)\hat{a}_{\mathbf{q}\nu}(t') + \hat{a}_{-\mathbf{q}\nu}(t)\hat{a}^\dagger_{-\mathbf{q}\nu}(t')]\rangle \delta_{\nu\nu'} \;, \tag{1.22}$$

where $\hat{a}^\dagger_{\mathbf{q}\nu}$ and $\hat{a}_{\mathbf{q}\nu}$ are the phonon creation and annihilation operators, respectively [27].

[2] A compact notation has been used, where $(\mathbf{x}t)$ or $(\mathbf{r}t) \to 1$, $(\mathbf{x}'t')$ or $(\mathbf{r}'t') \to 2$, $(\mathbf{r}t{+}\eta) \to 1^+$, and so on.

1.3 The phonon contribution to the electron self-energy

The Hedin-Baym Eqs. (1.12)–(1.18) summarized in Table 1.1 incorporate the effects of the electron-electron and the electron-phonon interactions on the electron Green's function on an equal footing. For the sake of clarity, it is convenient to separate both contributions. This can be achieved by setting $D = 0$ in a first step, which corresponds to considering the nuclei as classical particles rigidly fixed in their equilibrium positions, so that $\langle \hat{n}_{\rm n}(\mathbf{r}) \rangle \approx n^0_{\rm n}(\mathbf{r})$. The equation of motion for the electron Green's function at such rigid-nuclei configuration reads

$$\left[i \frac{\partial}{\partial t_1} + \frac{\nabla^2(1)}{2} - V^{\rm rn}_{\rm tot}(1) \right] G^{\rm rn}(12) - \int d3\, \Sigma^{\rm rn}_{\rm e}(13) G^{\rm rn}(32) = \delta(12) \ , \quad (1.23)$$

where $\Sigma^{\rm rn}_{\rm e}$ represents the electron-electron self-energy evaluated at rigid nuclei,

$$\Sigma(12) = i \int d(34)\, G^{\rm rn}(13)\, \Gamma^{\rm rn}(324) W^{\rm rn}_{\rm e}(41^+) \ . \quad (1.24)$$

Combining Eqs. (1.23),(1.24) with Eqs. (1.14),(1.16), one recovers the set of equations originally derived by Hedin [25], which neglected nuclear displacements altogether. Their implementation in actual calculations almost invariably assume $\Gamma^{\rm rn}(324) \approx \delta(13)\delta(23)$. This leads to the so-called GW method, which is the most common procedure to incorporate dynamical electron-electron interactions in first principles calculations [28–30].

The complete equation of motion Eq. (1.12) can be retrieved by means of the following Dyson equation,

$$G(12) = G^{\rm rn}(12) + \int d(34)\, G^{\rm rn}(13)\, \Sigma^{\rm ep}(34)\, G(42) \ , \quad (1.25)$$

where $G^{\rm rn}$ plays the role of the non-interacting Green's function. All the electron-phonon interactions are encoded in the self-energy $\Sigma^{\rm ep}$, which is conveniently separated in three terms [7]:

$$\Sigma^{\rm ep} = \Sigma^{\rm FM} + \Sigma^{\rm DW} + \Sigma^{\rm dGW} \ , \quad (1.26)$$

where the first term is the so-called dynamical Fan-Migdal self-energy,

$$\Sigma^{\rm FM}(12) = i\hbar \int d(34)\, G(13)\, \Gamma(324)\, W_{\rm ph}(41^+) \ , \quad (1.27)$$

the second term is the so-called static Debye-Waller self-energy,

$$\Sigma^{\rm DW}(12) = \int d3\, v(13) \left[\langle \hat{n}(3) \rangle - \langle \hat{n}^{\rm rn}(3) \rangle \right] \delta(12) \ , \quad (1.28)$$

and the third term is the correction to the electron-electron self-energy of Eq. (1.24) due to the fact that the full G, Γ and $W_{\rm e}$ are different from those evaluated in a situation where ions constitute a rigid crystal,

$$\Sigma^{\rm dGW}(12) = \Sigma_{\rm e}(12) - \Sigma^{\rm rn}_{\rm e}(12) \ . \tag{1.29}$$

This last term has not been investigated in this thesis, nor in any other work in the literature to the best of out knowledge [7]. As an original contribution of this thesis, some new aspects of the Debye-Waller term Eq. (1.28) related to the polaron problem will be discussed in Chapter 3. In the following, we focus on the dynamical Fan-Migdal self-energy, Eq. (1.27), which is responsible for most of the physical phenomena related to the electron-phonon interaction that are discussed in this thesis.

1.4 Practical approximations

The equations presented so far determine the electron Green's function exactly within the harmonic approximation. However, the full self-consistent solution of these equations is still not feasible in practice. In order to arrive to computable expressions, several approximations have to be made, which are briefly described in this section.

1.4.1 Migdal approximation

First of all, it is convenient to transform Eq. (1.15) from the canonical $\kappa p\alpha$ coordinates to the normal mode coordinates $\mathbf{q}\nu$ as in Eq. (1.20), so that we have [7],

$$\begin{aligned}\Sigma^{\rm FM}(12) = i\sum_{\nu\nu'}\int \frac{d\omega}{2\pi}\frac{d\mathbf{q}}{\Omega_{\rm BZ}} d(34) e^{-i\omega(t_4-t_1^+)} \\ \times G(13)\,\Gamma(324)\, g^{\rm cc}_{\mathbf{q}\nu}(\mathbf{r}_4,\omega)\, D_{\mathbf{q}\nu\nu'}(\omega)\, g_{\mathbf{q}\nu'}(\mathbf{r}_1,\omega) \ ,\end{aligned} \tag{1.30}$$

where the momentum-integral is over the Brillouin zone whose volume is $\Omega_{\rm BZ}$, and where we have defined [6],

$$\begin{aligned}g_{\mathbf{q}\nu}(\mathbf{r},\omega) = \sum_{\kappa p}\frac{1}{(2M_\kappa\omega_{\mathbf{q}\nu})^{1/2}}\int d\mathbf{r}'\ \epsilon^{-1}_{\rm e}(\mathbf{r},\mathbf{r}',\omega) \\ \times \mathbf{e}_{\kappa,\mathbf{q}\nu}\cdot\boldsymbol{\nabla}' V_\kappa(\mathbf{r}'-\boldsymbol{\tau}^0_{\kappa p}-\mathbf{R}_p)\, e^{i\mathbf{q}\cdot\mathbf{R}_p} \ ,\end{aligned} \tag{1.31a}$$

$$\begin{aligned}g^{\rm cc}_{\mathbf{q}\nu}(\mathbf{r},\omega) = \sum_{\kappa p}\frac{1}{(2M_\kappa\omega_{\mathbf{q}\nu})^{1/2}}\int d\mathbf{r}'\ \epsilon^{-1}_{\rm e}(\mathbf{r},\mathbf{r}',\omega) \\ \times \mathbf{e}^*_{\kappa,\mathbf{q}\nu}\cdot\boldsymbol{\nabla}' V_\kappa(\mathbf{r}'-\boldsymbol{\tau}^0_{\kappa p}-\mathbf{R}_p)\, e^{-i\mathbf{q}\cdot\mathbf{R}_p} \ .\end{aligned} \tag{1.31b}$$

Writing the self-energy in the form of Eq. (1.30) makes its intepretation in terms of Feynman diagrams more transparent, as represented in Fig. 1.1(a).

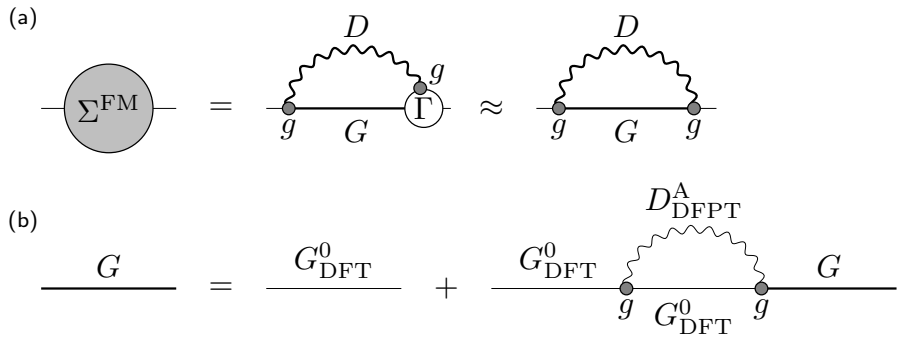

Figure 1.1. Diagrammatic representation of the approximations used for the electron-phonon self-energy. (a) Migdal approximation. (b) Dyson equation with the final approximated self-energy. Bold (thin) lines represent full interacting (non-interacting) propagators.

In this picture, Eqs. (1.31) represent the probability amplitude for an electron to emit or absorb a phonon, and the Fan-Migdal self-energy includes all the possible processes of this kind. In particular, all the multi-phonon processes are contained in the vertex function Γ of Eq. (1.14).

This interpretation also leads us to an important approximation we will use thorughout this thesis: the so-called Migdal approximation [3]. The essence of this approximation is to consider only the lowest-order diagram in the Fan-Migdal self-energy, so that $\Gamma(123) \approx \delta(13)\delta(23)$, as shown schematically in Fig. 1.1(b). This approximation corresponds to a second-order expansion in perturbation theory. It is equivalent to the GW method discussed in the context of electron-electron interactions. However, in this case the approximation is justified in most cases, since as Migdal showed [3], all the higher-order terms are smaller than the lowest-order term by a factor of ω_D/ε_F for normal metals, where ω_D is the so-called Debye frequency —typically a few meV—, and ε_F is the Fermi energy —typically a few eV.

Certainly, some interesting cases lie outside the range of validity of this approximation [22]. Unfortunately, the computational workload associated with the self-consistent calculation of the vertex function Eq. (1.14) has turned the numerical exploration of new physics beyond this approximation extremely challenging so far. To the best of our knowledge, it has never been achieved in the context of first principles calculations, and it has not been pursued in this thesis either.

1.4.2 Static electronic screening

As can be inferred from Eq. (1.31), the potential induced by an atomic displacement as a result of a phonon excitation will be screened by the electrons through the dielectric function $\epsilon_{\rm e}^{-1}(\mathbf{r},\mathbf{r}',\omega)$.

It is noteworthy that the frequency dependence of D (see Eq. (1.21)) will show structures only at small energies of the order of phonon frequencies $\omega_{\mathbf{q}\nu}$, which are much smaller than the typical electronic energies at which the frequency dependence of $\epsilon_{\rm e}^{-1}(\mathbf{r},\mathbf{r}',\omega)$ becomes important. As a result, it is usually a good approximation to assume $\epsilon_{\rm e}^{-1}(\mathbf{r},\mathbf{r}',\omega) \approx \epsilon_{\rm e}^{-1}(\mathbf{r},\mathbf{r}',0)$ in Eq. (1.31). Physically, this corresponds to assuming that the electrons respond instantaneously to the slow atomic displacements induced by phonons.

This approximation is almost invariably used in practical electron-phonon calculations, and will be adopted in this thesis as well. Nonetheless, given the key role that the electronic screening plays in the many-body theory of the electron-phonon interaction, in Chapter 2 we will analyze in more detail several aspects of the dielectric function $\epsilon_{\rm e}^{-1}(\mathbf{r},\mathbf{r}',\omega)$, and explore systems in which its frequency dependence might become important.

1.4.3 Density functional theory

Density Functional Theory (DFT) [31, 32] has been one of the most important methodological developments of the last decades towards the solution of many-body problems in actual materials from first principles. Along the same lines, it has also marked an extremely fruitful path from the early theoretical formulations of the electron-phonon problem in idealized models [33–35], to their application in realistic systems.

In the following, we briefly review the main aspects of DFT which make the general expressions derived in this chapter amenable for practical calculations. Detailed discussions related to the foundations of DFT, and more practical aspects involving actual calculations within this approach can be found, for example, in Refs. [36–38].

DFT is a mean-field theory, which effectively translates the problem of N interacting electrons into a set of Schrödinger equations for N independent electrons immersed in an effective potential incorporating *in principle* all the electron-electron interactions. The single-particle states — so-called Kohn-Sham (KS) states— obtained in this way provide a legitimate basis in which the equations presented in the previous sections can be rewritten. Due to the periodicity of the crystal lattice, the single-particle KS states can be labeled with the crystal momentum index $\mathbf{k}$, and the band index n. Born-Von Karman boundary conditions will be used, considering a generic supercell of N_p unit cells. In this way, the single-particle KS energies will be denoted by $\varepsilon_{n\mathbf{k}}$ and the wave functions will obey the Bloch theorem [39],

$$\varphi_{n\mathbf{k}}(r) = u_{n\mathbf{k}}(r)\, e^{i\mathbf{k}\cdot\mathbf{r}} \ , \tag{1.32}$$

where $u_{n\mathbf{k}}(r)$ has the periodicity of the crystal lattice.

Although DFT is strictly a ground-state theory, experience has shown that in the majority of cases KS states also provide a good representation of the excitation spectra at rigid nuclei. Corrections beyond this approximation can be incorporated, for example, through Eqs. (1.23),(1.24). Significant deviations have been found mainly in the band structure of strongly-correlated systems such as oxides or heavy-fermion materials, and in the band-gap of semiconductors and insulators, which are aspects that have not been studied in this thesis. We have therefore used G^0_{DFT} as the non-interacting Green's function in the Dyson equation Eq. (1.25), making the approximation $G^{\mathrm{rn}} \approx G^0_{\mathrm{DFT}}$. Moreover, it can be shown [6] that the Fourier transform of G^0_{DFT} takes a particularly simple form in the basis of the KS states,

$$G^0_{\mathrm{DFT},nn'\mathbf{k}\mathbf{k}'}(\omega) = \frac{\delta_{nn'}\,\delta_{\mathbf{k}\mathbf{k}'}}{(\omega - \varepsilon_{n\mathbf{k}} \pm i\eta)} \ , \tag{1.33}$$

where the positive and negative signs correspond to occupied and unoccupied states, respectively, being $\eta = 0^+$.

Similarly, the extension of DFT to treat external perturbations, namely Density Functional Perturbation Theory (DFPT) [8], has proven to be an extremely efficient and accurate method to describe lattice dynamics in real materials. We have used this method to compute phonon frequencies $\omega_{\mathbf{q}\nu}$, and thus the adiabatic phonon Green's function Eq. (1.21), throughout this thesis. In fact, as discussed in Sec. 1.2, non-adiabatic renormalization effects on phonons have not been explored in this thesis, so that we have effectively used the approximation $D \approx D^{\mathrm{A}}_{\mathrm{DFPT}}$ throughout the dissertation.

Besides phonon frequencies, DFPT also provides the self-consistent variation of the effective KS potential with respect to the atomic displacements induced by a phonon mode, that is,

$$\Delta_{\mathbf{q}\nu} V^{\mathrm{KS}}(\mathbf{r}) = \sum_{\kappa p \alpha} \frac{1}{(2M_\kappa \omega_{\mathbf{q}\nu})^{1/2}}\, e_{\kappa\alpha,\mathbf{q}\nu}\, \frac{\partial V^{\mathrm{KS}}}{\partial \tau_{\kappa\alpha}}\Big|_{\mathbf{r}-\mathbf{R}_p} \exp(i\mathbf{q}\cdot\mathbf{R}_p) \ . \tag{1.34}$$

This variation of the potential can be identified in Eq. (1.31) after approximating the many-body electronic screening of Eq. (1.18) by the one obtained within DFT, that is $\epsilon^{-1}_{\mathrm{e}}(\mathbf{r},\mathbf{r}',0) \approx \epsilon^{-1}_{\mathrm{DFT}}(\mathbf{r},\mathbf{r}',0)$, since one can show that $\partial V^{\mathrm{KS}}/\partial\tau_{\kappa\alpha} = \epsilon^{-1}_{\mathrm{DFT}}\,\partial V_\kappa/\partial\tau_{\kappa\alpha}$ (see, for example, Ref. [7] Sec. III.4).

Finally, the matrix elements of Eq. (1.31) in the single-particle KS basis are usually referred to as the electron-phonon matrix elements,

$$g^\nu_{mn}(\mathbf{k},\mathbf{q}) = \langle \varphi_{m\mathbf{k}+\mathbf{q}} | \Delta_{\mathbf{q}\nu} V^{\mathrm{KS}} | \varphi_{n\mathbf{k}} \rangle \ , \tag{1.35}$$

which gives the probability amplitude for the scattering of an electron from the KS state $n\mathbf{k}$ to the KS state $m\mathbf{k}+\mathbf{q}$ through the emission or absorption of a phonon mode $\mathbf{q}\nu$.

1.4.4 One-shot Green's function and diagonal self-energy

Another important approximation that we will adopt is to replace G by G^0_{DFT} in the electron self-energy Eq. (1.30), relaxing in this way the self-consistency between Eq. (1.25) and Eq. (1.30). This approximation amounts to neglecting all the non-crossing multiple-phonon diagrams in the Dyson equation, as represented in Fig. 1.1(b), and it is sometimes referred to as the *one-shot* Migdal approximation. We note that the nature of the Dyson equation itself still results in a summation of an infinite amount of single-phonon diagrams. The full self-consistency of the Green's function on the electron self-energy will be accounted for in the study of superconductivity, as discussed in Appendix A. This numerically challenging condition can be mitigated efficiently by the method described in Chapter 4.

Assuming that the crystal periodicity has to be maintained in the electron-phonon processes, the electron self-energy has to be invariant under spatial translation, so that $\Sigma(\mathbf{r}+\mathbf{R}_p, \mathbf{r}'+\mathbf{R}_p) = \Sigma(\mathbf{r},\mathbf{r}')$ for all values of p. As a result, its off-diagonal $\mathbf{k} \neq \mathbf{k}'$ Fourier components vanish, and the Dyson equation becomes a diagonal matrix equation in $\mathbf{k}$-representation. Deviations from this assumption in relation with the polaron problem will be discussed in Sec. 3.4.

As a last approximation, if we neglect the possibility of band hybridization induced by the electron-phonon interaction, the electron self-energy — and thus the Dyson equation — takes a diagonal matrix form in the KS basis. In this way, we arrive at the final expression for the electron self-energy most commonly used in the literature,

$$\Sigma_{n\mathbf{k}}(\omega) = \sum_{m\nu} \int \frac{d\mathbf{q}}{\Omega_{\mathrm{BZ}}} |g^{\nu}_{mn}(\mathbf{k},\mathbf{q})|^2 \times \Big[\frac{1 - f_{m\mathbf{k}+\mathbf{q}}}{\omega - \varepsilon_{m\mathbf{k}+\mathbf{q}} - \omega_{\mathbf{q}\nu} + i\eta} + \frac{f_{m\mathbf{k}+\mathbf{q}}}{\omega - \varepsilon_{m\mathbf{k}+\mathbf{q}} + \omega_{\mathbf{q}\nu} - i\eta} \Big] , \tag{1.36}$$

where $\eta \to 0^+$, and $f_{n\mathbf{k}}$ is the Fermi-Dirac occupation factor for the KS state $n\mathbf{k}$. Since up to now we are working strictly at zero temperature we have $f_{n\mathbf{k}} = 1$ for occupied KS states and zero otherwise[3].

Finally, by rewriting the Dyson Eq. (1.25) in the KS basis the matrix inversion becomes trivial, and the electron-phonon driven renormalization of the non-interacting KS states can be obtained through the self-energy of Eq. (1.36),

$$G^{-1}_{n\mathbf{k}}(\omega) = (\omega - \varepsilon_{n\mathbf{k}} \pm i\eta) - \Sigma_{n\mathbf{k}}(\omega) . \tag{1.37}$$

[3]The extension of this expression to finite temperatures involves the use of the Matsubara formalism [27] followed by an analytic continuation from the discrete imaginary Matsubara frequencies to the real-axis [40]. In this way we arrive to an expression for the so-called retarded self-energy [23], which is similar to Eq. (1.36) but with a positive sign in the infinitesimals at both denominators, and inluding bosonic phonon occupation factors in the numerators [7].

The solution of Eqs. (1.36)–(1.37) form the basis to study most of the physical effects introduced by electron-phonon interaction in solids from first-principles. In Chapter 3 we will analyze in detail the renormalization of electron quasiparticles driven by this interaction. In Appendix. A, we derive the extension of these equations needed to describe the phonon-mediated superconducting phase transition, which are efficiently solved numerically in Chapter 4.

Chapter 2

Coupled spin-charge plasmons at surfaces with strong relativistic effects

The spin is an intrinsic angular momentum degree of freedom and a fundamental property of the electrons. The possibility of controlling an manipulating spin currents and densities in solid-state systems gives rise to the field of *spintronics* [41].

A necessary condition for reaching this goal is to lift the spin degeneracy of electronic states present in most solids. Traditionally, this has been achieved through the breaking of time-reversal symmetry by the exchange interaction in magnetic systems [42]. A novel direction in spintronics exploits the relativistic spin-orbit coupling in non-magnetic materials, because in crystals without inversion-symmetry, such as surfaces or interfaces, the electronic energy-bands are spin-split by this interaction [43]. This gives rise to a plethora of novel effects, the study of which has just started [44].

On the other hand, as a matter of fact, the external perturbations in solids are screened by the electrons. This becomes apparent in the equations presented in Table. 1.1, where the many-body interactions of Eqs. (1.15)–(1.16) are mediated by the screened Coulomb potentials. In particular, the electron-phonon interaction, a central topic in this thesis, takes place through the change of the potential induced by the atomic displacements, which is screened by the electronic response (see Eq. (1.34) and discussion below). Thus, it appears crucial to understand the effects of the spin-orbit interaction in the electronic response if one aims to understand the dynamics of spins in a many-body environment.

In this chapter, we will implement a Wannier interpolation procedure to compute efficiently the density-response function at surfaces from first

principles. This will allow us to study, for the first time, the effects of the spinorial nature of the electrons in the response properties of complex relativistic surfaces. In particular, we will analyze the effects introduced by the spin-orbit coupling in the self-sustained collective modes that might exist in the system. As we will show, the electronic response of systems with spin-orbit coupling will be of a mixed spin-charge character, giving rise to a novel collective excitation which we name *coupled spin-charge plasmon*. We will illustrate the existence of this new excitation in realistic materials by performing first principles calculations in the Tl/Si(111) surface.

2.1 Spin-orbit coupling in the electronic response

In this section, we will review the main aspects needed to compute the electronic response function from first principles, and we will incorporate the spinorial nature of the electron wave functions in the formalism. Moreover, we will outline a procedure to characterize the real space and spin-charge structure of self-sustained collective modes from the knowledge of the generalized dielectric response function.

2.1.1 Linear response theory and TDDFT

We are interested in studying the response of the electronic density to a small external potential, δV^{ext}. In this regime, the change in the density, δn, can be considered to be linear and given by:

$$\delta n(\mathbf{r},t) = \int dt' \int d^3\mathbf{r}\ \chi(\mathbf{r},\mathbf{r}',t-t')\,\delta V^{\text{ext}}(\mathbf{r}',t')\ , \tag{2.1}$$

where χ is the so-called density-response function, which is only finite for positive time differences.

The formalism used in this thesis to compute the density-response function has been the Time-Dependent Density Functional Theory (TDDFT) [45–47]. As in ordinary DFT, the problem of the many-body interacting system is solved using an auxiliary non-interacting system. In this case, the response of the full interacting system can be related to the response of the non-interacting Kohn-Sham system by the following Dyson equation [46, 47],

$$\begin{aligned}\chi(\mathbf{r},\mathbf{r}',t-t') = \chi^{\text{KS}}(\mathbf{r},\mathbf{r}',t-t') + \int dt_1\,dt_2 \int d^3r_1\,d^3r_2\ \chi^{\text{KS}}(\mathbf{r},\mathbf{r}_1,t-t_1) \\ \times \left[\frac{\delta(t_1-t_2)}{\mathbf{r}_1-\mathbf{r}_2} + f^{\text{xc}}(\mathbf{r}_1,\mathbf{r}_2,t_1-t_2)\right]\ \chi(\mathbf{r}_2,\mathbf{r}',t_2-t')\ ,\end{aligned} \tag{2.2}$$

where χ^{KS} is the so-called non-interacting Kohn-Sham response function, and f_{xc} is the so-called exchange-correlation kernel evaluated at the ground-state density,

$$f^{\text{xc}}(\mathbf{r}_1,\mathbf{r}_2,t_1-t_2) = \left.\frac{\delta V^{\text{xc}}(\mathbf{r}_1,t_1)}{\delta n(\mathbf{r}_2,t_2)}\right|_{n=n_{\text{GS}}}\ , \tag{2.3}$$

being δV^{xc} the exchange-correlation potential [36, 37].

Similar to the exchange-correlation potential in regular DFT, the exact form of the kernel in Eq. (2.3) is not known, and approximated expressions have to be used. In this thesis, we have adopted the Adiabatic Local Density Approximation (ALDA) of f_{xc} [47, 48].

In order to study the excitation energies of periodic solids, it is convenient to consider the Fourier transform of Eq. (2.2) to frequency and momentum variables,

$$\chi_{\mathbf{G},\mathbf{G}'}(\mathbf{q},\omega) = \chi^{\mathrm{KS}}_{\mathbf{G},\mathbf{G}'}(\mathbf{q},\omega) + \sum_{\mathbf{G}_1,\mathbf{G}_2} \chi^{\mathrm{KS}}_{\mathbf{G},\mathbf{G}_1}(\mathbf{q},\omega) \times \left[\frac{4\pi}{|\mathbf{q}+\mathbf{G}_1|^2}\delta_{\mathbf{G}_1,\mathbf{G}_2} + f^{\mathrm{xc}}_{\mathbf{G}_1,\mathbf{G}_2}(\mathbf{q},\omega)\right] \chi_{\mathbf{G}_2,\mathbf{G}'}(\mathbf{q},\omega) \ , \quad (2.4)$$

where the non-interacting response is given by the well-known expression in terms of the single-particle KS states as [49–51],

$$\chi^{\mathrm{KS}}_{\mathbf{G},\mathbf{G}'}(\mathbf{q},\omega) = \frac{1}{N_{\mathbf{k}}\Omega}\sum_{\mathbf{k}}^{1\mathrm{BZ}}\sum_{nm}\frac{(f_{n\mathbf{k}} - f_{m\mathbf{k}+\mathbf{q}})}{\omega + (\varepsilon_{n\mathbf{k}} - \varepsilon_{m\mathbf{k}+\mathbf{q}}) + i\eta} \times \langle\varphi_{n\mathbf{k}}|e^{-i(\mathbf{q}+\mathbf{G})\mathbf{r}}|\varphi_{m\mathbf{k}+\mathbf{q}}\rangle\,\langle\varphi_{m\mathbf{k}+\mathbf{q}}|e^{i(\mathbf{q}+\mathbf{G}')\mathbf{r}}|\varphi_{n\mathbf{k}}\rangle \ , \quad (2.5)$$

being $N_{\mathbf{k}}$ the number of points in the first Brillouin zone (1BZ), Ω the volume of the unit cell, $f_{n\mathbf{k}}$ are the Fermi-Dirac occupation factors for the KS states, $\mathbf{G}$ represents a reciprocal lattice vector and $\eta \to 0^+$.

Within the framework of TDDFT, the dielectric response function of Eq. (1.18) can be obtained as,

$$\epsilon_{\mathbf{G},\mathbf{G}'}(\mathbf{q},\omega) = \delta_{\mathbf{G},\mathbf{G}'} - \sum_{\mathbf{G}''}\chi^{\mathrm{KS}}_{\mathbf{G},\mathbf{G}''}(\mathbf{q},\omega)\,F^{\mathrm{xc}}_{\mathbf{G}'',\mathbf{G}'}(\mathbf{q},\omega), \quad (2.6)$$

where F^{xc} is the term within brackets in Eq. (2.4). The dielectric function relates the external potential and the total change in the self-consistent potential ($\delta V^{\mathrm{sc}} = \delta V^{\mathrm{ext}} + \delta V^{\mathrm{KS}}$) by,

$$\delta V^{\mathrm{ext}}_{\mathbf{G}}(\mathbf{q},\omega) = \sum_{\mathbf{G}'}\epsilon_{\mathbf{G},\mathbf{G}'}(\mathbf{q},\omega)\,\delta V^{\mathrm{sc}}_{\mathbf{G}'}(\mathbf{q},\omega) \ , \quad (2.7)$$

where δV^{KS} is the change in the Kohn-Sham potential induced by the external perturbation.

From Eq. (2.7) it can be deduced that self-sustained oscillations ($\delta V^{\mathrm{sc}} \neq 0$ and $\delta V^{\mathrm{ext}} = 0$) can exist only if the following condition is satisfied:

$$\det\left[\epsilon_{\mathbf{G},\mathbf{G}'}(\mathbf{q},\omega)\right] = 0 \ . \quad (2.8)$$

Thus, the $\mathbf{q}$ and ω for which solutions of Eq.(2.8) are found define the dispersion relation of the collective excitations in the system.

2.1.2 Spinorial structure of the response function

Under the presence of the spin-orbit interaction, the KS states have to be generalized to two-component spinors,

$$\Psi_{\mathbf{k}n}(\mathbf{r}) = \begin{pmatrix} \varphi^{\uparrow}_{\mathbf{k}n}(\mathbf{r}) \\ \varphi^{\downarrow}_{\mathbf{k}n}(\mathbf{r}) \end{pmatrix} \ , \tag{2.9}$$

where $\varphi^{\uparrow}_{\mathbf{k},n}(\mathbf{r})$ and $\varphi^{\downarrow}_{\mathbf{k},n}(\mathbf{r})$ represent the up/down components for a given direction. The components of the spinor wave function satisfy a set of two coupled KS equations [52] in which the effective scalar potential (V^{KS}) is replaced by a spin-dependent one ($V^{\mathrm{KS}}_{\alpha\beta}$), and the ordinary electron density becomes a four component spin-density matrix,

$$\mathbf{n}^{\alpha\beta}(\mathbf{r}) = \frac{1}{N_{\mathbf{k}}} \sum_{\mathbf{k}n}^{\mathrm{occ}} \varphi^{\alpha}_{\mathbf{k},n}(\mathbf{r}) \left(\varphi^{\beta}_{\mathbf{k},n}(\mathbf{r})\right)^{*} \ . \tag{2.10}$$

By extension, the relation given by Eq. (2.1) has to be generalized to account for the spin-density response. The KS response function of Eq. (2.5) is directly generalized to a 4×4 matrix by,

$$\begin{aligned} \chi^{\mathrm{KS},\alpha\beta\alpha'\beta'}_{\mathbf{G},\mathbf{G}'}(\mathbf{q},\omega) = \frac{1}{N_{\mathbf{k}}\Omega} \sum_{\mathbf{k}}^{1\mathrm{BZ}} \sum_{nm} \frac{(f_{n\mathbf{k}} - f_{m\mathbf{k}+\mathbf{q}})}{\omega + (\varepsilon_{n\mathbf{k}} - \varepsilon_{m\mathbf{k}+\mathbf{q}}) + i\eta} \\ \times \langle \varphi^{\beta}_{n\mathbf{k}} | e^{-i(\mathbf{q}+\mathbf{G})\mathbf{r}} | \varphi^{\alpha}_{m\mathbf{k}+\mathbf{q}} \rangle \langle \varphi^{\alpha'}_{m\mathbf{k}+\mathbf{q}} | e^{i(\mathbf{q}+\mathbf{G}')\mathbf{r}} | \varphi^{\beta'}_{n\mathbf{k}} \rangle \ , \end{aligned} \tag{2.11}$$

and the Dyson equation of Eq. (2.4) is now given by a matrix inversion in both space ($\mathbf{G}, \mathbf{G}'$) and spin ($\alpha\beta$) variables, which formally reads

$$\boldsymbol{\chi} = [\mathbf{1} - \boldsymbol{\chi}_{\mathrm{KS}} \ \mathbf{F}_{\mathrm{xc}}]^{-1} \ \boldsymbol{\chi}_{\mathrm{KS}} \ . \tag{2.12}$$

A clearer physical interpretation can be obtained by means of the Pauli matrices $\boldsymbol{\sigma}^{\mu} \equiv (\boldsymbol{\sigma}^0, \boldsymbol{\sigma}^x, \boldsymbol{\sigma}^y, \boldsymbol{\sigma}^z)$,

$$\mathbf{n}^{\mu} = \sum_{\alpha\beta} \boldsymbol{\sigma}^{\mu}_{\alpha\beta} \mathbf{n}^{\beta\alpha} \ , \tag{2.13}$$

$$\boldsymbol{\chi}^{\mu\nu} = \sum_{\alpha\beta\alpha'\beta'} \boldsymbol{\sigma}^{\mu}_{\beta\alpha} \ \boldsymbol{\chi}^{\alpha\beta\alpha'\beta'} \boldsymbol{\sigma}^{\nu}_{\alpha'\beta'} \ , \tag{2.14}$$

where $\mathbf{n}^{\mu}$ represents the four-component density vector $\mathbf{n}^{\mu} = (\rho, m_x, m_y, m_z)$, ρ being the scalar charge-density and $\mathbf{m}$ the vectorial spin-density. In this way, we arrive at the generalized linear spin-charge density response equation,

$$\delta\mathbf{n}^{\mu}(\mathbf{r},\omega) = \sum_{\nu} \int d^3r' \boldsymbol{\chi}^{\mu\nu}(\mathbf{r},\mathbf{r}',\omega) \ \delta\boldsymbol{V}^{\nu(\mathrm{ext})}(\mathbf{r}',\omega) \ , \tag{2.15}$$

which relates the induced charge and spin densities, and the external electromagnetic field, $\delta\boldsymbol{V}^{\nu(\mathrm{ext})} = (\delta V_0^{(\mathrm{ext})}, \delta B_x^{(\mathrm{ext})}, \delta B_y^{(\mathrm{ext})}, \delta B_z^{(\mathrm{ext})})$.

2.1.3 Coupled spin-charge plasmons in real space

Similar to Eq. (2.15), the relation of Eq. (2.7) can be generalized to relate 4-component external and total self-consistent potentials,

$$\delta \boldsymbol{V}^{\mu,\mathbf{G}\,(\mathrm{ext})} = \sum_{\nu} \sum_{\mathbf{G}'} \boldsymbol{\varepsilon}^{\mu\nu,\mathbf{G}\mathbf{G}'}\, \delta \boldsymbol{V}^{\nu,\mathbf{G}'\,(\mathrm{sc})} \ , \tag{2.16}$$

where $\boldsymbol{\varepsilon}^{\mu\nu,\mathbf{G}\mathbf{G}'}$ is obtained from Eq. (2.6), Eq. (2.11) and Eq. (2.14).

In this case, the plasmon condition of Eq. (2.8) holds provided that the determinant is evaluated accounting for both the space and the spin degrees of freedom. Indeed, we can express Eq. (2.16) as an eigenvalue equation, in a similar way as in Ref. [53] but including spin,

$$\sum_{\nu} \sum_{\mathbf{G}'} \boldsymbol{\varepsilon}^{\mu\nu,\mathbf{G}\mathbf{G}'}(\mathbf{q},\omega)\ \delta \boldsymbol{V}_i^{\nu,\mathbf{G}'}(\mathbf{q},\omega) = \epsilon_i(\mathbf{q},\omega)\ \delta \boldsymbol{V}_i^{\mu,\mathbf{G}}(\mathbf{q},\omega) \ , \tag{2.17}$$

so that the condition imposed in Eq. (2.8) is satisfied for the solution of Eq. (2.17) with a vanishing eigenvalue ($\epsilon_i(\mathbf{q},\omega) = 0$).

The eigenvector corresponding to such a solution will be composed by four elements for each reciprocal lattice vector $\mathbf{G}$,

$$\delta \boldsymbol{V}_i^{\mu,\mathbf{G}}(\mathbf{q},\omega) = \begin{pmatrix} \delta V_0^{\mathbf{G}}(\mathbf{q},\omega) \\ \delta B_x^{\mathbf{G}}(\mathbf{q},\omega) \\ \delta B_y^{\mathbf{G}}(\mathbf{q},\omega) \\ \delta B_z^{\mathbf{G}}(\mathbf{q},\omega) \end{pmatrix}_i \ , \tag{2.18}$$

and the real space representation of the oscillation can be then obtained by a Fourier transformation,

$$\delta \boldsymbol{V}_i^{\mu}(\mathbf{r};\mathbf{q},\omega) = \sum_{\mathbf{G}} \ e^{-i(\mathbf{q}+\mathbf{G})\cdot\mathbf{r}}\ \delta \boldsymbol{V}_i^{\mu,\mathbf{G}}(\mathbf{q},\omega) \ , \tag{2.19}$$

where $\delta \boldsymbol{V}_i^{\mu}(\mathbf{r};\mathbf{q},\omega)$ describes the real space structure of the self-sustained spin-charge oscillations with momentum $\mathbf{q}$ at the resonance frequency ω .

2.2 Wannier interpolation

The formalism described in Sec. 2.1 provides a general roadmap to compute the dispersion and the real space structure of the possible spin-charge collective excitations that may exist in a given system.

However, the energy scale of plasmons at surfaces and two-dimensional materials is known to be much smaller than in conventional three-dimensional crystals [54]. This poses a practical challenge from the computational point of view, as can be deduced from the expression for the KS response given by Eq. (2.5). The $(\varepsilon_{n\mathbf{k}} - \varepsilon_{m\mathbf{k}+\mathbf{q}})$ energy difference on the denominator shows that the frequency resolution that one can obtain will be limited by the

density of **k**-points considered in the 1BZ sum. A possibility is to choose to converge the sums faster by considering a larger smearing parameter η, but in that case the possible spectral features of similar order of magnitude to η would be blurred. In fact, in order to be able to distinguish low-energy features in the response function, one should choose η as small as possible and sample the 1BZ as densely as possible.

This issue is well-known in the electron-phonon problem, where the low-energy scale of phonons makes an extremely fine sampling of the 1BZ mandatory to obtain converged self-energies through Eq. (1.36). A strategy to solve this issue which has proven to be extremely successful in this field has been the so-called Wannier interpolation technique [9, 10]. This technique will be applied in Chapter 3 and Chapter 4 to interpolate the electron-phonon matrix elements of Eq. (1.35).

In this thesis, we have implemented a similar procedure for the efficient interpolation of the **k**-dependent matrix elements entering the 1BZ sum in Eq. (2.5). For simplicity, we will describe the scalar case, as the application to the spin-generalized case of Eq. (2.11) is straightforward.

2.2.1 Maximally localized Wannier functions

We start by briefly reviewing the general aspects of the Wannier functions [55] in the context of first principles calculations. Detailed derivations and discussions can be found, for example, in Refs. [56–58]

The general relation between a set of Bloch functions, such as the KS states of Eq. (1.32), and the corresponding Wannier functions at the cell R_p is given by the following generalized Fourier transform [56],

$$w_{m\mathbf{R}_p}(\mathbf{r}) = \frac{1}{N_\mathbf{k}} \sum_\mathbf{k} e^{-i\mathbf{k}\cdot\mathbf{R}_p} \sum_n U_{mn\mathbf{k}}\, \varphi_{n\mathbf{k}}(\mathbf{r}) \ , \tag{2.20}$$

and inversely by,

$$\varphi_{n\mathbf{k}}(\mathbf{r}) = \sum_p e^{i\mathbf{k}\cdot\mathbf{R}_p} \sum_m U^\dagger_{mn\mathbf{k}}\, w_{m\mathbf{R}_p}(\mathbf{r}) \ , \tag{2.21}$$

where $U_{mn\mathbf{k}}$ is an arbitrary unitary matrix. The arbitrariness in the definition of the Wannier functions can be exploited in the following way: it is a basic property of Fourier transforms that the smoother a reciprocal-space object is, the sharper (more localized) the transformed real space object is. Inversely, if one is able to construct Wannier functions which are localized in space, the corresponding Bloch functions given by Eq. (2.21) will be smooth — and therefore amenable for interpolation — in **k**-space.

The most popular procedure to obtain such maximally localized Wannier functions was put forward in Ref. [56], and generalized to deal with entangled bands found in metals in Ref. [57]. The main idea is to minimize the quadratic spread functional of the Wannier functions in real space, starting from an

inital set of Bloch states with arbitrary phase as obtained from a conventional DFT calculation. In this way, one is able to obtain the Wannier functions that are maximally localized in real space, and from there deduce the unitary matrices $\tilde{U}_{mn\mathbf{k}}$ with which the initial Bloch states have to be multiplied in order to obtain the so-called maximally smooth Bloch functions, which we will denote by,

$$\tilde{\varphi}_{n\mathbf{k}}(\mathbf{r}) = \sum_m \tilde{U}_{mn\mathbf{k}}\, \varphi_{n\mathbf{k}}(\mathbf{r}) \ . \tag{2.22}$$

For a single isolated band, Eq. (2.22) corresponds to choosing a gauge in which the phase of the wave functions changes smoothly in $\mathbf{k}$-space. Note that in the case of multiple bands, in general the $\tilde{\varphi}_{n\mathbf{k}}$ functions will not be eigenstates of the original Hamiltonian.

2.2.2 Interpolation of the electron band structure

From the knowledge of the unitary matrices needed to obtain the maximally smooth Bloch functions over the Brillouin zone, we can obtain the Hamiltonian in the so-called Wannier gauge,

$$\tilde{H}^{\mathrm{KS}}_{nm}(\mathbf{k}) = \langle \tilde{\varphi}_{m\mathbf{k}} | \hat{H}^{\mathrm{KS}} | \tilde{\varphi}_{n\mathbf{k}} \rangle = [\tilde{U}^{\dagger}_{\mathbf{k}}\, H^{\mathrm{KS}}(\mathbf{k})\, \tilde{U}_{\mathbf{k}}]_{nm} \ , \tag{2.23}$$

where $H^{\mathrm{KS}}_{nm}(\mathbf{k}) = \varepsilon_{n\mathbf{k}}\delta_{nm}$ is a diagonal matrix composed by the KS energies in the initial mesh of $\mathbf{k}$-points. We can Fourier transform Eq. (2.23) to obtain the representation of the Hamiltonian in the basis of the maximally localized Wannier functions,

$$\tilde{H}^{\mathrm{KS}}_{nm}(\mathbf{R}_p) = \langle \tilde{w}_{m\mathbf{0}} | \hat{H}^{\mathrm{KS}} | \tilde{w}_{n\mathbf{R}_p} \rangle = \frac{1}{N_{\mathbf{k}}} \sum_{\mathbf{k}}^{1\mathrm{BZ}} e^{-i\mathbf{k}\cdot\mathbf{R}_p}\, \tilde{H}^{\mathrm{KS}}_{nm}(\mathbf{k}) \ . \tag{2.24}$$

Due to their localization property, the Hamiltonian in the basis of the Wannier functions will decay rapidly with $\mathbf{R}_p$. Thus, an accurate interpolation of $\tilde{H}^{\mathrm{KS}}_{nm}(\mathbf{k}')$ can be obtained to $\mathbf{k}'$-points outside the inital mesh by the Fourier transform,

$$\tilde{H}^{\mathrm{KS}}_{nm}(\mathbf{k}') = \sum_p e^{i\mathbf{k}'\cdot\mathbf{R}_p}\, \tilde{H}^{\mathrm{KS}}_{nm}(\mathbf{R}_p) \ . \tag{2.25}$$

Finally, $\tilde{H}^{\mathrm{KS}}_{nm}(\mathbf{k}')$ can be diagonalized to obtain the interpolated electron energies as,

$$[P^{\dagger}_{\mathbf{k}'} \tilde{H}^{\mathrm{KS}}(\mathbf{k}') P_{\mathbf{k}'}]_{mn} = \delta_{mn}\, \varepsilon_{n\mathbf{k}'} \ . \tag{2.26}$$

In this way, very fine samplings of the energies and occupancies entering Eq. (2.5) can be obtained.

Similarly, the interpolation of the electron velocities — given by the $\mathbf{k}$-derivatives of the energies — that we will need in Chapter 4 can be obtained by taking the derivatives analytically in the right-hand side of Eq. (2.25),

$$\tilde{H}^{\mathrm{KS}}_{nm,\alpha}(\mathbf{k}') = \sum_p^{N_p} iR_{p,\alpha}\, e^{i\mathbf{k}'\cdot\mathbf{R}_p}\, \tilde{H}^{\mathrm{KS}}_{nm}(\mathbf{R}_p) \tag{2.27}$$

and diagonalizing the resulting matrix [59],

$$v_{n\mathbf{k}',\alpha} = [P^{v\,\dagger}_{\mathbf{k}'}\, \tilde{H}^{\mathrm{KS}}_{\alpha}(\mathbf{k}')\, P^{v}_{\mathbf{k}'}]_{nn} \ . \tag{2.28}$$

2.2.3 Interpolation of the matrix elements

We now extend the procedure described in the previous section in order to interpolate the matrix elements appearing in Eq. (2.5),

$$Z_{\mathbf{k},mn}(\mathbf{q},\mathbf{G}) = \langle \varphi_{m\mathbf{k}+\mathbf{q}} | e^{i(\mathbf{q}+\mathbf{G})\cdot\mathbf{r}} | \varphi_{n\mathbf{k}} \rangle \tag{2.29}$$

which are the major bottleneck in the computation of the response function.

For that purpose, we can use the unitary matrices $\tilde{U}_{mn\mathbf{k}}$ of Eq. (2.22) to rotate the original matrix elements computed in a coarse mesh of $\mathbf{k}$-points as,

$$\tilde{Z}_{\mathbf{k},mn}(\mathbf{q},\mathbf{G}) = [\tilde{U}^{\dagger}_{\mathbf{k}+\mathbf{q}}\, Z_{\mathbf{k}}(\mathbf{q},\mathbf{G})\, \tilde{U}_{\mathbf{k}}]_{mn} \tag{2.30}$$

Similar to Eq. (2.25), a reliable Fourier interpolation of $\tilde{Z}_{\mathbf{k},mn}(\mathbf{q},\mathbf{G})$ can now be performed,

$$\tilde{Z}_{\mathbf{k}',mn}(\mathbf{q},\mathbf{G}) = \sum_{p} e^{i\mathbf{k}'\cdot\mathbf{R}_p} \frac{1}{N_{\mathbf{k}}} \sum_{\mathbf{k}} e^{-i\mathbf{k}\cdot\mathbf{R}_p}\, \tilde{Z}_{\mathbf{k},mn}(\mathbf{q},\mathbf{G}) \ , \tag{2.31}$$

from which the interpolated matrix elements can finally be obtained using the unitary matrices of Eq. (2.26),

$$Z_{\mathbf{k}',mn}(\mathbf{q},\mathbf{G}) = [P^{\dagger}_{\mathbf{k}'}\, \tilde{Z}_{\mathbf{k}'}(\mathbf{q},\mathbf{G})\, P_{\mathbf{k}'}]_{mn} \ . \tag{2.32}$$

By following this procedure, we are able to obtain very dense samplings of all the $\mathbf{k}$-dependent quantities entering Eq. (2.5) — and thus converged summations for small values of η — for a given $\mathbf{q}$ at a reasonable cost, in which the expensive explicit computation of the matrix elements and energies is limited to an initial coarse mesh.

Finally, in order to obtain a smooth $\mathbf{q}$-dependent momentum dispersion of the response matrix, we can directly interpolate the smooth Bloch wave function of Eq. (2.22) in its real space representation to an arbitrary $\mathbf{k}' = \mathbf{k} + \mathbf{q}'$ point,

$$\tilde{\varphi}_{n\mathbf{k}+\mathbf{q}'}(\mathbf{r}) = \sum_{p} e^{i(\mathbf{k}+\mathbf{q}')\cdot\mathbf{R}_p} \frac{1}{N_{\mathbf{k}''}} \sum_{\mathbf{k}''} e^{-i\mathbf{k}''\cdot\mathbf{R}_p}\ \tilde{\varphi}_{n\mathbf{k}''}(\mathbf{r}) \ . \tag{2.33}$$

Then, after computing the matrix elements,

$$\tilde{Z}_{\mathbf{k},mn}(\mathbf{q}',\mathbf{G}) = \langle \tilde{\varphi}_{m\mathbf{k}+\mathbf{q}'} | e^{i(\mathbf{q}'+\mathbf{G})\cdot\mathbf{r}} | \tilde{\varphi}_{n\mathbf{k}} \rangle \ , \tag{2.34}$$

we can follow the very same procedure for the interpolation in $\mathbf{k}$ through Eqs. (2.31)–(2.32), as $\tilde{Z}$ is maximally smooth now.

In the case of the electron-phonon matrix elements of Eq. (1.35), the change in the potential is periodic in momentum-space, $\Delta_{\mathbf{q}+\mathbf{G},\nu}V^{\mathrm{KS}} = \Delta_{\mathbf{q},\nu}V^{\mathrm{KS}}$, so that one can compute its Fourier transform to obtain the phonon counterpart of the Wannier functions [10]. In this way, a simultaneous Fourier interpolation on both $\mathbf{k}$ and $\mathbf{q}$ variables can be performed [9], allowing for very dense samplings of the Brillouin zone at a reasonable cost.

2.3 Coupled spin-charge plasmon at Tl/Si(111)

After the first measurement of the spin-orbit induced splitting on the surface states of Au(111) [60], there have been many instances of this effect in clean surfaces of heavy-element crystals [61–63], and in heavy-atom adlayers on semiconducting substrates [64–66].

Moreover, the development of spin-resolved photoemission (SARPES) has permitted the characterization of intricate spin-textures on these spin-split surface states [67–69], beyond the simplified picture of the Rashba model in which the spin-polarization is restricted to be circular on the surface plane [43]. In this respect, fully relativistic DFT calculations have been proven to provide accurate spin-textures in diverse systems in agreement with experimental results [70–74].

Among the different materials mentioned above, the Tl/Si(111) surface stands out as a perfect candidate in which the effects of the spin-orbit coupling can be studied and exploited. It presents a giant spin-splitting in both occupied and unoccupied surface states, clearly located at the band-gap of the semiconducting bulk substrate [72]. Due to the particular symmetry of the interface, the spin-polarization of the occupied surface states acquire a complex Rashba-like circular polarization around the $\bar{\Gamma}$-point and an out-of plane polarization at the $\bar{K}$-point [67, 72]. Moreover, the unoccupied states form oppositely polarized valleys at the $\bar{K}, \bar{K}'$ points [72, 75], which can be doped to obtain a fully spin-polarized Fermi surface so that the backscattering is strongly supressed [76, 77].

The interplay between the electron-phonon scattering and the complex spin-texture of the surface states in this system has been analyzed in detail in Ref. [78]. In this thesis, we study the effects of the non-collinear spin-polarization in the response properties of this surface, applying for the first time in first principles calculations the full 4×4 formalism described in Sec. 2.1.

2.3.1 Ground-state calculations

The Tl/Si(111) surface was simulated considering a slab system consisting of 10 Si layers with a Tl adlayer and a vacuum space of 27 Å between the repeated slabs. On the other side of the slab a hydrogen adlayer was introduced in order to saturate the dangling bonds. The ground state

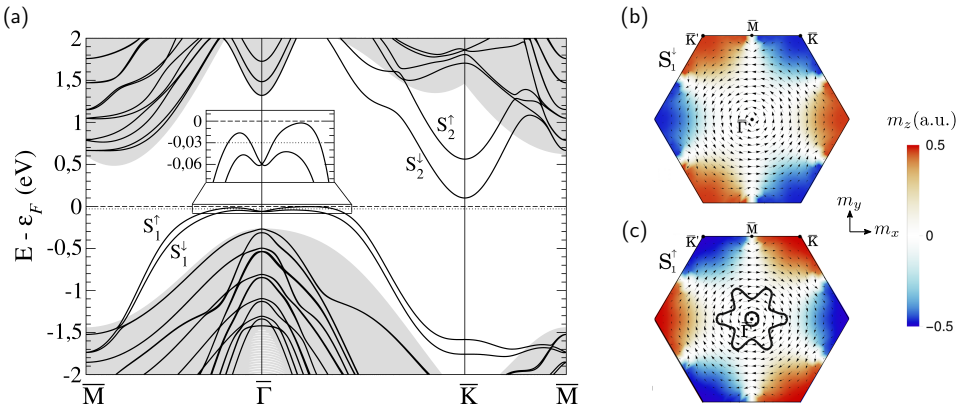

Figure 2.1. Ground state electronic structure of the Tl/Si(111) surface. (a) Calculated band structure. Energies are given with respect to Fermi energy, which is represented by the dashed line. The dotted line shows the shifted Fermi level used in the response function calculations. The light gray background represents the bulk band projection. The inset shows a zoom of the $S_1^{\downarrow}$ and $S_1^{\uparrow}$ surface bands near the $\bar{\Gamma}$ point. (b) and (c) Momentum dependent spin polarization of the two occupied surface states $S_1^{\downarrow}$ and $S_1^{\uparrow}$, respectively, over the whole first surface Brillouin zone. Arrows represent the in-plane spin polarization components, whereas the color code represents the out-of-plane spin polarization component. The Fermi contour corresponding to the Fermi level shifted by -0.03 eV is represented by the black solid line in (c).

calculations were performed using the all-electron LAPW method [38] as implemented in the ELK code [79], considering a 24×24×1 **k**-point grid and the non-collinear LSDA approximation for the exchange-correlation energy [48]. Spin-orbit interaction has been included self-consistently in all the ground state calculations.

We show in Fig. 2.1 the essential information about the electronic band structure and spin polarization of the Tl/Si(111) surface, as obtained by means of our relativistic ground state calculations. In Fig. 2.1(a), the solid black lines correspond to the slab bands, while the continuous grey background represents the projected band structure of bulk silicon. Fig. 2.1(b)–(c) display the calculated momentum-dependent spin textures of the occupied surface bands $S_1^{\downarrow}$ and $S_1^{\uparrow}$, defined as the expectation value of the Pauli matrices,

$$\mathbf{m}_n(\mathbf{k}) = \frac{1}{\Omega} \int d^3r \, \Psi^{\dagger}_{n\mathbf{k}}(\mathbf{r}) \, \boldsymbol{\sigma} \, \Psi_{n\mathbf{k}}(\mathbf{r}) \ , \tag{2.35}$$

where Ω represents the volume of the unit-cell. Our results for the non-collinear spinor structure compare well with previous spin DFT calculations

based on the pseudopotential method [72], as well as with angle and spin resolved photoemission experiments [67, 75].

In order to study possible plasmon excitations in the system, we consider a moderate hole-doping of 30 meV (see dotted-line in the inset of Fig. 2.1(a)). This results in a fully spin-polarized Fermi surface with chiral spin texture, with only the upper spin-split subband $S_1^{\uparrow}$ crossing the Fermi level. However, since the splitting of bands $S_1^{\uparrow}$ and $S_1^{\downarrow}$ remains almost constant in the vicinity of the $\bar{\Gamma}$ point, the band structure of this surface near this point deviates substantially from that of the pure Rashba-like systems.

2.3.2 Spin-charge density-response matrix

We now move to the computation of the generalized spin-charge response matrix, following the procedure described in Secs. 2.1.1–2.1.2. The non-interacting 4×4 component response function has been obtained evaluating the summation of Eq. (2.11) over a dense 840×840 **k**-point grid, in which all the **k**-dependent elements have been interpolated using the Wannier-interpolation technique, as described in Sec. 2.2. This procedure allows to achieve converged results considering a damping parameter as small as $\eta = 1$ meV, and permits to obtain a smooth **q**-dependent map of the response functions.

In Fig. 2.2 we show the macroscopic contributions ($\mathbf{G} = 0, \mathbf{G}' = 0$) of all the 16 elements of the generalized non-interacting spin-charge density response matrix at the hole-doped (−30 meV) Tl/Si(111) surface. For the sake of simplicity, we have focused on a momentum **q** along the $\bar{\Gamma} - \bar{\mathrm{M}}$ direction, which corresponds to the y axis in our coordinate system. Therefore, from now on we refer to the coordinate x as the transverse direction.

We note that in non-magnetic systems with spin-degenerate bands and negligible spin-orbit coupling, only the diagonal elements (χ_{00}, χ_{xx}, χ_{yy}, χ_{zz}) are non-zero. In the case of collinear magnetic systems, and taking the magnetization axis as the z-coordinate, only the diagonal elements and the transverse-spin/transverse-spin elements (χ_{xy}, χ_{yx}) are non-zero [80]. In systems with pure Rasba-like spin-orbit coupling and completely in-plane chiral spin texture, taking the momentum transfer vector **q** in the direction of the y coordinate, we would have eight non-zero elements (χ_{00}, χ_{0x}=χ_{x0}, χ_{xx}, χ_{yy}, χ_{yz}=-χ_{zy}, χ_{zz}) [81]. Therefore, the charge/spin correlations only appear due to the non-collinear nature of the wave functions in systems with significant spin-orbit coupling. However, the response matrix still appears decoupled into charge/transverse-spin and longitudinal-spin/perpendicular-spin block matrices.

Fig. 2.2 shows that in the case of the Tl/Si(111) surface, the response roughly follows the case of a pure Rashba-like system. Nevertheless, due to the anisotropy of the Fermi surface and the non-zero perpendicular component of the spin-polarization of the surface states, we can appreciate a non-zero

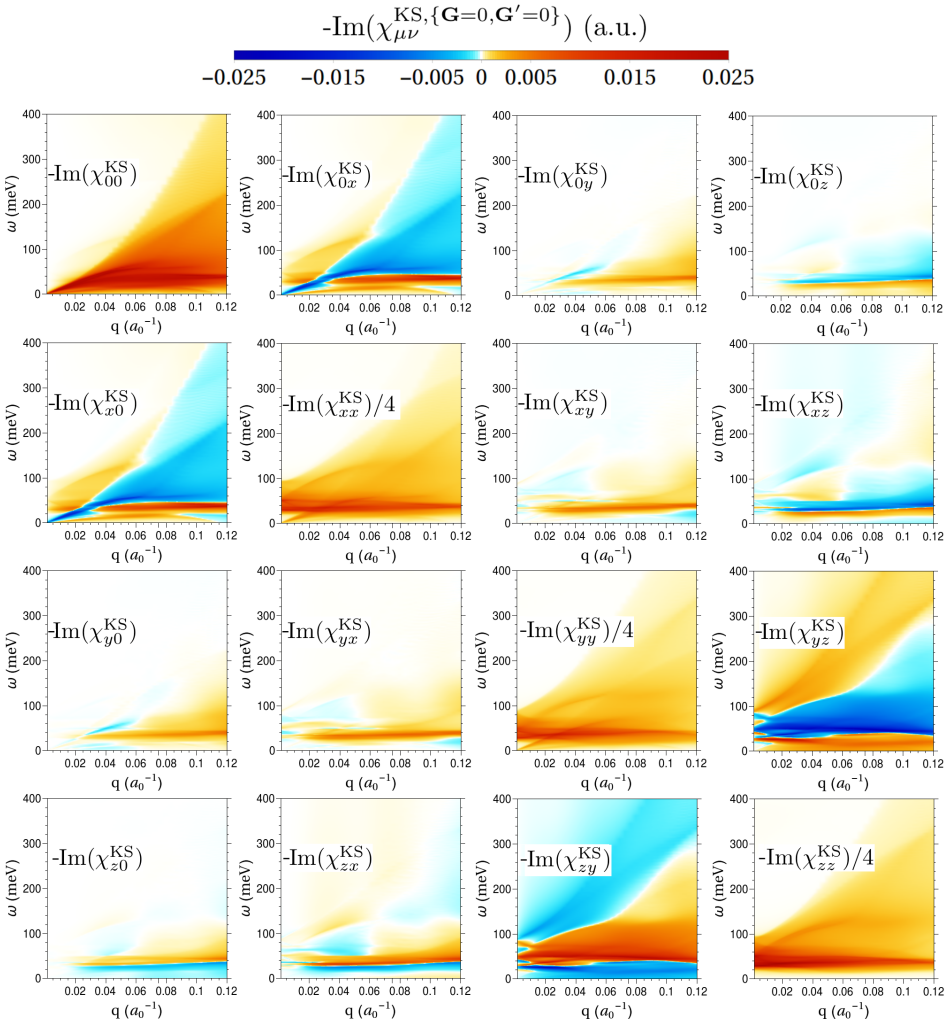

Figure 2.2. First-principles calculation of the 16 components of the non-interacting spin-charge density response matrix at the hole-doped Tl/Si(111) surface in the $\omega \in (0, 400)$ meV energy and $|\mathbf{q}| \in (0, 0.12)$ a_0^{-1} momentum range, with $\mathbf{q}$ along the $\bar{\Gamma} - \bar{M}$ direction (cartesian y axis in our coordinate system). The color code represents the imaginary part of the macroscopic contribution ($\mathbf{G} = 0, \mathbf{G}' = 0$) of the response in atomic units.

(though considerably smaller) intensity in the off-diagonal χ^{KS}_{y0}, χ^{KS}_{0y}, χ^{KS}_{z0}, χ^{KS}_{0z}, χ^{KS}_{xy}, χ^{KS}_{yx}, χ^{KS}_{xz} and χ^{KS}_{zx} responses.

In general terms, colored regions in Fig. 2.2 define the regions of the ($\mathbf{q}$, ω) space where the possible collective modes of the system may suffer from damping due to single-particle excitations [82]. The intraband single-particle excitation continuum can be noticed in all the components of the non-interacting response matrix. Moreover, the interband excitation continuum

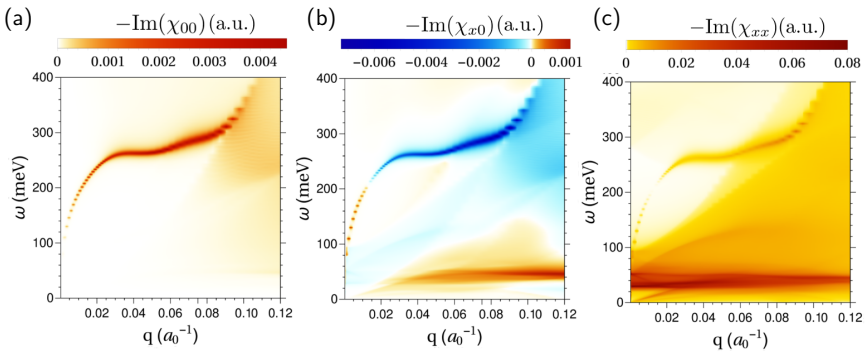

Figure 2.3. Selected components of the interacting spin-charge response matrix on the Tl/Si(111) surface. (a),(b),(c) Calculated charge/charge, transverse-spin/charge and transverse-spin/transverse-spin response functions, respectively, for **q** along the $\bar{\Gamma} - \bar{\mathrm{M}}$ direction (corresponding to y in our coordinate system).

— also called "Rashba" continuum [81] — is also visible in the $\mathrm{Im}(\chi^{\mathrm{KS}}_{x0})$ and $\mathrm{Im}(\chi^{\mathrm{KS}}_{xx})$ components. Interestingly, we find that interband transitions carry a change of sign in $\mathrm{Im}(\chi^{\mathrm{KS}}_{x0})$ with respect to the intraband transitions, originating from the opposite spin orientation of the two spin-split subbands. Finally, we note that interband transitions in $\mathrm{Im}(\chi^{\mathrm{KS}}_{yz})$ and $\mathrm{Im}(\chi^{\mathrm{KS}}_{zy})$ will not allow for collective excitations to exist in this response channels. In the following, we focus on the most significant χ_{00}, χ_{0x}=χ_{x0} and χ_{xx} components.

The full interacting response has been obtained by direct inversion of Eq. (2.12), keeping the local field effects from which the most important contributions correspond to the **G**-vectors perpendicular to the surface plane. We use the LSDA approximation of the exchange-correlation kernel [48], and we consider a truncation of the Coulomb potential in the direction perpendicular to the surface in order to avoid artificial interaction between the slabs [83].

Fig. 2.3 shows our results for the interacting spin-charge response matrix. A prominent peak on the charge/charge response component $\mathrm{Im}(\chi_{00})$ is observable in Fig. 2.3(a), which lies well above the single-particle excitation continuum up to $|\mathbf{q}| \sim 0.08$ a_0^{-1}. The dispersion of this peak clearly resembles the $\omega_q \sim \sqrt{q}$ dispersion of a quasi-2D charge plasmon [54, 84, 85]. Remarkably, the spin-charge interplay in the response introduced by the spin-texture of the surface states becomes manifest when we evaluate $\mathrm{Im}(\chi_{x0})$ and $\mathrm{Im}(\chi_{xx})$, as in both of these functions a similar peak is observed with exactly the same dispersion (see Fig. 2.3(b)–(c)), together with the single-particle excitation background in the case of $\mathrm{Im}(\chi_{xx})$.

As for $\mathrm{Im}(\chi_{x0})$, we observe a sign change and an intensity enhancement for low values of **q**. This effect comes from the aforementioned sign change of the $\mathrm{Im}(\chi^{\mathrm{KS}}_{x0})$ function, and is in principle also present in conventional pure

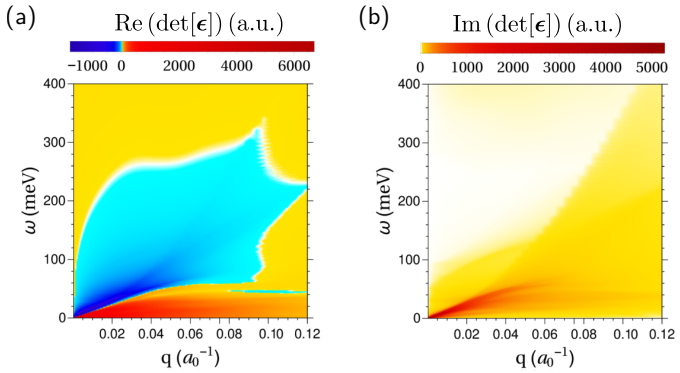

Figure 2.4. Plasmon dispersion on the Tl/Si(111) surface. (a),(b) Real and imaginary parts of the determinant of the spin-charge dielectric response matrix, respectively, which are relevant for determining the presence of possible collective modes and their real space details (see Eqs.(2.16)–(2.19) and discussion therein).

Rashba-like systems. However, when considering the response of a realistic surface such as Tl/Si(111) from first principles new features arise. The almost constant splitting between the subbands near Γ (see inset of Fig. 2.1(a)), makes the interband continuum to remain at low energies in the considered momentum range, allowing for a well-defined collective excitation — free from decaying into single-particle excitations — in the region of interest. In addition, for larger momentum transfers, another almost constantly dispersive peak starting at $|\mathbf{q}| \sim 0.03$ a_0^{-1} appears in $\mathrm{Im}(\chi_{x0})$ (see Fig. 2.3(f)), coming from the low-energy interband transitions as well. For the sake of conciseness, from now on we will focus on the $\omega_q \sim \sqrt{q}$ dispersing mode.

2.3.3 Two-dimensional coupled spin-charge plasmon

In order to get further insight in the nature of the excitation, we compute the real space structure of the eigenmode giving a zero eigenvalue for each $(\mathbf{q}, \omega)$ point in which $\det[\boldsymbol{\varepsilon}] = 0$ is fulfilled, as described in Sec. 2.1.3,

Firstly, we show in Figs. 2.4(a)–(b) the calculated imaginary and real parts of $\det[\boldsymbol{\varepsilon}^{\mu\nu,\mathbf{GG'}}](\mathbf{q}, \omega)$, respectively, in the same momentum and frequency range as in Fig. 2.3(a)–(c). We can recognize the peaks in $\mathrm{Im}(\chi_{00})$, $\mathrm{Im}(\chi_{x0})$ and $\mathrm{Im}(\chi_{xx})$ as zeros of the function $\mathrm{Re}(\det[\boldsymbol{\varepsilon}(\mathbf{q}, \omega)])$ which lie in regions with vanishingly small $\mathrm{Im}(\det[\boldsymbol{\varepsilon}(\mathbf{q}, \omega)])$. This unambiguously identifies the excitation as a well defined self-sustained collective oscillation.

Next, we show in Fig. 2.5 the real space structure of the self-sustained oscillation as a function of $\mathbf{q}$ and z, being the latter the real space coordinate perpendicular to the surface. The ordinary charge part (δV_0) and transverse-magnetic component (δB_x) of the oscillation are represented in Fig. 2.5(a) and

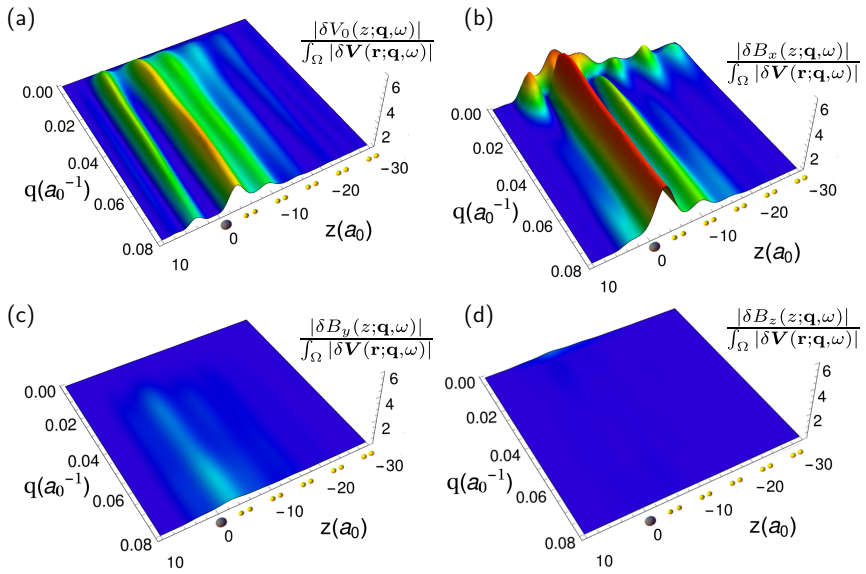

Figure 2.5. Real space configuration and **q** dependence of the coupled spin-charge collective oscillation at the Tl/Si(111) surface. (a) Magnitude of the induced charge potential oscillation and (b)–(d) induced magnetic field oscillation of the self-sustained excitation, where $|\delta A|^2 = \int_\omega d^3r \sum_\mu (\delta\boldsymbol{\phi}(\mathbf{r})^\mu)^* \delta\boldsymbol{\phi}(\mathbf{r})^\mu$. The z coordinate corresponds to the direction perpendicular to the surface, with negative values indicating penetration into the bulk. Orientative positions of the first thallium and silicon atomic layers are represented by big gray and small yellow spheres, respectively.

Fig. 2.5(b), respectively. The longitudinal (δB_y) and surface perpendicular (δB_z) magnetic components are negligible in comparison, and are shown in Fig. 2.5(c) and Fig. 2.5(d), respectively. For simplicity, we keep only the z dependence by averaging the amplitudes in the surface-plane directions.

The quasi-2D character of the mode is confirmed as both components remain localized within the first five atomic layers (∼12 a_0) close to the surface area. Most importantly, this figure reveals that the amplitude of the transverse-magnetic component δB_x is of a similar order of magnitude and even larger than the amplitude of the charge part over the considered momentum range. We also observe that the real space configuration of this mode is almost independent of the momentum except for the $\mathbf{q}\to 0$ limit, where we find a strong enhancement of the magnetic component relative to the charge part.

These results explicitly demonstrates the mixed spin-charge character of the collective excitations at surfaces with strong spin-orbit coupling.

2.4 Conclusion

In conclusion, in this chapter we have presented a new first-principles treatment of the generalized spin-charge density response tensor, and applied our methodology to the Tl/Si(111) surface. An efficient calculation of the response matrix has been performed through the implementation of Wannier interpolation methods.

Our calculations demonstrate the appearance of a coupled spin-charge collective mode localized at the first few atomic layers close to the surface, which, as a direct consequence of the chiral spin texture of the Fermi contour, is composed by a transverse-spin density oscillation in addition to the usual charge density oscillation. We resolve the real space details of this collective mode and show that the order of magnitude of both amplitudes is similar. This coupled spin-charge plasmon should be understood as a general phenomenon, as long as the relevant electron band structure is circularly spin polarized. Moreover, the first principles character of our approach allows to explore other surface systems with more complex Fermi surfaces and spin textures, setting the ground to find novel types of collective spin-charge excitations in realistic materials.

Chapter 3

Complex quasiparticle renormalization driven by the electron-phonon interaction

The *quasiparticle* concept, introduced by Landau [86], encompasses all the elementary excitations of condensed matter systems that can be somehow rationalized as particles with definite effective properties such as energy, momentum or mass. Some quasiparticles, such as phonons, do not have analog isolated particles outside the many-body environment. Some others do, but due to their interactions with all the other quasiparticles present in the system, their properties are said to be *renormalized* with respect to the free non-interacting particles. The notion of quasiparticles has been extremely useful providing a more intuitive understanding of emergent phenomena in many-body physics.

In this chapter, we analyze in detail the renormalization of the electron properties due to their interaction with phonons. We pay particular attention to the energy-momentum dispersion relation of electronic excitations, that is, to the electron quasiparticle band structure. We will see that in order to properly account for the lifetime and spectral weight of quasiparticles under the electron-phonon interaction, an analytic continuation of the self-energies and Green's functions from real to complex energies is required. This poses a challenging problem also from the computational point of view. We review the existing methods developed in the literature to achieve this task, introducing some improvements that increase their numerical stability and expand their range of operation. As an application, we rationalize the recently measured photoemission spectra of doped monolayer MoS_2 [87] in terms of long-living electron quasiparticles with strongly renormalized properties. Finally, as an outlook, we present a Green's function formulation

for the description of the phonon-mediated localization of electrons, giving rise to *polaron* quasiparticles.

3.1 Quasiparticles within the Green's function formalism

In most experiments on materials properties one excites the sample in one way or another and measures its response. For example, in Angle Resolved Photoemission Spectroscopy (ARPES) electrons are ejected from the material upon irradiation with light. By measuring the kinetic energy of the photoemitted electrons for different emission angles, one can access the momentum-resolved one-electron removal spectra of the material under study [88].

The Green's function formalism presented in Sec. 1.2 provides a solid mathematical framework in which this spectra can be described and interpreted from a theoretical point of view. In Chapter 1 we have reviewed a procedure by which the Green's function of an interacting electron-phonon system can be calculated. In this section, we describe how to identify the quasiparticle excitations from the knowledge of such a Green's function. A thorough analysis of the mathematical concepts involved in this section can be found in Ref. [89].

To start with, by introducing a complete set of eigenstates s of the $(N+1)$-particle and $(N-1)$-particle many-body system, that is $|N+1,s\rangle$ and $|N-1,s\rangle$, in Eq. (1.11a) and Eq. (1.11b), respectively, and by performing a Fourier transform from time to frequency variables, we arrive to the so-called Lehmann representation of the Green's function [6, 90],

$$G(\mathbf{x},\mathbf{x}';\omega) = \sum_s \frac{f_s(\mathbf{x})\, f_s^*(\mathbf{x}')}{\omega - [\varepsilon_s + i\eta\,\mathrm{sgn}(\mu-\varepsilon_s)]}\ , \tag{3.1}$$

where,

$$f_s(\mathbf{x}) = \langle\, N \,|\, \hat{\Psi}(\mathbf{x}) \,|\, N+1, s \,\rangle \qquad \text{for} \quad \varepsilon_s \geq \mu\ , \tag{3.2a}$$

$$f_s(\mathbf{x}) = \langle\, N-1, s \,|\, \hat{\Psi}(\mathbf{x}) \,|\, N \,\rangle \qquad \text{for} \quad \varepsilon_s < \mu\ , \tag{3.2b}$$

and,

$$\varepsilon_s = E_{N+1,s} - E_N \qquad \text{for} \quad \varepsilon_s \geq \mu\ , \tag{3.3a}$$

$$\varepsilon_s = E_N - E_{N-1,s} \qquad \text{for} \quad \varepsilon_s < \mu\ , \tag{3.3b}$$

being $E_{N\pm1,s}$ is the energy corresponding to the $|N\pm1,s\rangle$ eigenstate, and E_N the ground state energy. Inspecting the denominator of Eq. (3.1), we see that the poles of the Green's function in the Lehmann representation,

which lie infinitesimally close to the real axis, give the electron addition and removal energies of the many-body system.

Using the identity $(\omega \pm i\eta)^{-1} = \mathcal{P}(\omega^{-1}) \pm i\pi\delta(\omega)$, where $\mathcal{P}$ denotes a Cauchy principal value, the so-called spectral function can be defined from Eq. (3.1) [6],

$$\begin{aligned} A(\mathbf{x}, \mathbf{x}'; \omega) &= \frac{1}{\pi} \operatorname{sgn}(\mu - \varepsilon_s) \operatorname{Im}\left[G(\mathbf{x}, \mathbf{x}'; \omega)\right] \\ &= \sum_s f_s(\mathbf{x})\, f_s^*(\mathbf{x}')\, \delta(\omega - \varepsilon_s) \ , \end{aligned} \tag{3.4}$$

which can be interpreted as a local density of states. Due to the periodicity of the crystal lattice, its spatial Fourier transform will be diagonal in momentum $\mathbf{k}$, and indeed it can be shown that $A_{\mathbf{k}}(\omega)$ defines the one-electron removal spectra that one can probe with ARPES [88].

Let us assume for a moment that our many-body state is formed by non-interacting single-particle states, like for example, the Kohn-Sham states discussed in Sec. 1.4.3. In that case, the electron addition and removal energies are just the KS eigenvalues $\varepsilon_{n\mathbf{k}}$, the amplitudes of Eq. (3.2) are the KS orbitals $\varphi_{n\mathbf{k}}(\mathbf{x})$, and we recover the non-interacting Green's function of Eq. (1.33). In this scenario, the spectral-function $A^0_{\mathbf{k}}(\omega)$ will be just a delta function for each of the KS energies, and the Green's function will have a simple pole at the real axis, as shown schematically in Fig. 3.1(a).

In the general case, however, the many-body system will be formed by interacting particles. Therefore, the single-electron excitations, such as $\hat{c}^\dagger_{\mathbf{k}} |N\rangle$, will not be eigenstates of the system, and their evolution involves overlaps with all the possible excited states with $N+1$ electrons. Given that $G(\omega)$ is the sum over the possible s configurations in the Lehmann representation — see Eq. (3.1) —, this gives rise to a set of singularities on the real axis, as shown schematically in Fig. 3.1(b). In turn, the spectral function $A_{\mathbf{k}}(\omega)$ is composed by a superposition of delta functions at the excitation energies. In the thermodynamic limit ($N \to \infty$), the singularities form a branch-cut in the real axis and the spectral function takes a continuous structure, as represented by the dashed line of Fig. 3.1(b).

Intuitively, one can still recognize prominent peaks in the spectra of many interacting systems. This motivates the search for an alternative interpretation of the spectral function, not as a combination of an infinite amount of many-body configurations, but as the excitation of an emergent *quasiparticle*. Formally, this interpretation can be achieved through the Dyson equations (see Eqs. (1.23),(1.25)). It can be shown [89, 91], that the Green's function admits an alternative representation to Eq. (3.1), which is the so-called biorthonormal representation,

$$\widetilde{G}(\mathbf{x}, \mathbf{x}'; z) = \sum_m \frac{\psi_m(\mathbf{x}; z)\, \tilde{\psi}^*_m(\mathbf{x}'; z)}{z - \widetilde{E}_m(z)} \ . \tag{3.5}$$

Both the Lehmann and the biorthonormal representations are exact and therefore give the same spectral function. In Eq. (3.5), ψ_m, $\tilde{\psi}^*_m$ and $\widetilde{E}_m$ are the m-th right-eigenvector, left-eigenvector and eigenvalue, respectively, of the non-hermitian so-called quasiparticle Hamiltonian,

$$\hat{\mathcal{H}}^{\mathrm{qp}}(z) = \hat{H}^0 + \hat{\Sigma}(z) \ , \tag{3.6}$$

where $\hat{H}^0$ is the hamiltonian defining the non-interacting Green's function G^0 in each case, and $\hat{\Sigma}$ the corresponding self-energy giving the full interacting Green's function through the Dyson equation. In our case, $\hat{H}^0$ will be the DFT hamiltonian corresponding to a rigid arrangement of the nuclei, and $\hat{\Sigma}$ will be the electron-phonon self-energy of Eq. (1.36), where a proper analytic continuation to complex frequencies z has to be considered, as discussed in the next section.

From Eq. (3.5) it is recognized that the poles of the Green's function in the biorthonormal representation are given by the complex frequencies fulfilling $z = \tilde{E}_n(z)$, that is

$$\det\left(zI - \hat{H}^0 - \hat{\Sigma}(z)\right) = 0 \ . \tag{3.7}$$

Equation (3.7) is sometimes referred to as the quasiparticle equation. As discussed in Sec. 1.4.4, in the most common approximation one assumes that the self-energy is diagonal in the single-particle KS basis. In this way, the quasiparticle equation Eq. (3.7) takes a simpler form, and the quasiparticle energies $\widetilde{E}^{\mathrm{qp}}_m = \varepsilon^{\mathrm{qp}}_m - i\,\Gamma^{\mathrm{qp}}_m$ can be obtained from the self-consistent solution of the following equation on the complex plane [92, 93],

$$\widetilde{E}^{\mathrm{qp}}_m - \varepsilon_{n\mathbf{k}} - \widetilde{\Sigma}_{n\mathbf{k}}(\widetilde{E}^{\mathrm{qp}}_m) = 0 \rightarrow \left\{ \begin{array}{c} \varepsilon^{\mathrm{qp}}_m - \varepsilon_{n\mathbf{k}} - \mathrm{Re}\left(\widetilde{\Sigma}_{n\mathbf{k}}(\varepsilon^{\mathrm{qp}}_m - i\,\Gamma^{\mathrm{qp}}_m)\right) = 0 \\ \Gamma^{\mathrm{qp}}_m + \mathrm{Im}\left(\widetilde{\Sigma}_{n\mathbf{k}}(\varepsilon^{\mathrm{qp}}_m - i\,\Gamma^{\mathrm{qp}}_m)\right) = 0 \end{array} \right\} . \tag{3.8}$$

Two aspects of this equation are noteworthy, which are the possibility of finding more than one solution as a result of its non-linearity, and the complex nature of its solutions as a result of the complex self-energy.

From the solutions of Eq. (3.8) the quasiparticle approximation follows. This approximation assumes that the interacting Green's function can be described by the sum of the first order Laurent expansions around the simple poles at the quasiparticle energies, so that,

$$\widetilde{G}_{n\mathbf{k}}(z) \approx G^{\mathrm{qp}}_{n\mathbf{k}}(z) = \sum_m \frac{\mathbb{Z}^{\mathrm{qp}}_m}{z - \widetilde{E}^{\mathrm{qp}}_m} \ , \tag{3.9}$$

where $\mathbb{Z}^{\mathrm{qp}}_m = \left(1 - \widetilde{\Sigma}'(\widetilde{E}^{\mathrm{qp}}_m)\right)^{-1}$ is the so-called renormalization factor, given by the residue of each pole. The real part of $\mathbb{Z}^{\mathrm{qp}}_m$ reflects the spectral weight of each quasiparticle state, and its imaginary part rotates the ideal Lorentzian

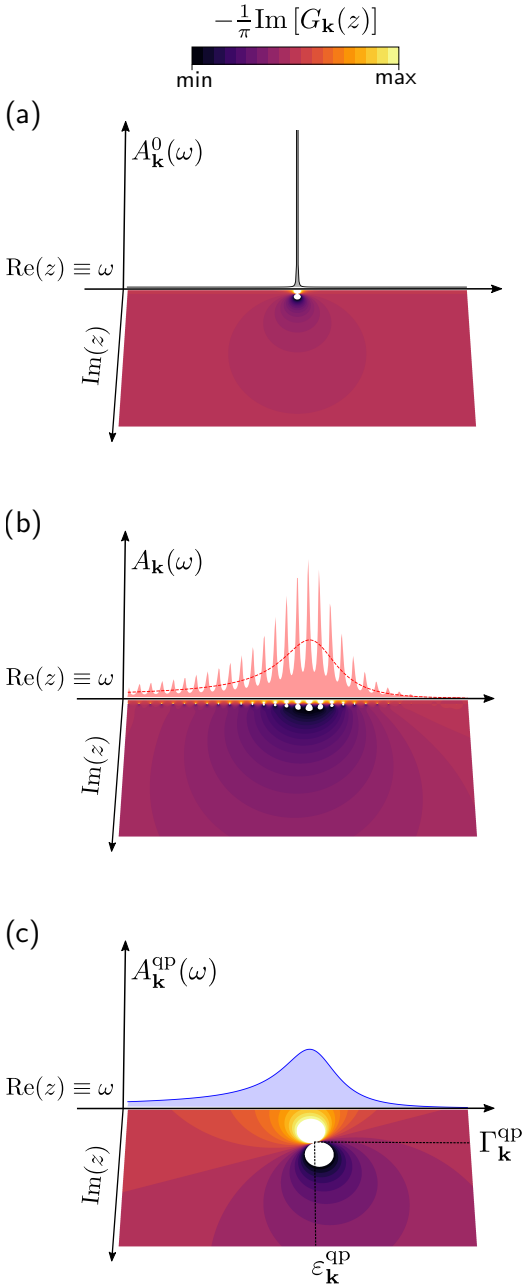

Figure 3.1. Schematic representation of the complex-plane analytic structure of (a) the non-interacting Green's function, (b) the interacting Green's function in the Lehmann representation and (c) the quasiparticle approximation of the interacting Green's function in the biorthonormal representation. The quasiparticle energies ($\varepsilon^{\mathrm{qp}}_{\mathbf{k}}$) and inverse-lifetimes ($\Gamma^{\mathrm{qp}}_{\mathbf{k}}$) are identified in (c). The projections on the vertical planes represent the spectral function $A_{\mathbf{k}}(\omega)$ corresponding to each case.

shape of the contribution of each pole on the spectral function [93]. The analytic structure of Eq. (3.9) and its corresponding spectral function are shown schematically in Fig. 3.1(c), for the case of a single quasiparticle pole.

Physically, Eq. (3.9) can be more easily interpreted by taking the Fourier transform to time variables, which for a single pole reads

$$G^{\rm qp}_{n\mathbf{k}}(t-t') = -i\,\mathbb{Z}^{\rm qp}_{n\mathbf{k}}\, e^{-i\,\varepsilon^{\rm qp}_{n\mathbf{k}}\,(t-t')}\, e^{-\Gamma^{\rm qp}_{n\mathbf{k}}\,(t-t')}\ , \tag{3.10}$$

clearly describing the propagation of a particle with energy $\varepsilon^{\rm qp}$ that decays with a lifetime $\tau = (2\Gamma^{\rm qp})^{-1}$. In the next section, we discuss numerical methods to determine accurately the quasiparticle energies and lifetimes for interacting electron-phonon systems.

3.2 Analytic continuation of the electron-phonon self-energy

The self-consistent solution of Eq. (3.8) determines the energies and lifetimes of electron and hole quasiparticles given by $\widetilde{E}^{\rm qp}_m = \varepsilon^{\rm qp}_m - i\,\Gamma^{\rm qp}_m$. All the many-body interactions are encoded in the self-energy, which is in general a complex function of complex arguments. From Eq. (3.10) follows that a physically meaningful decaying quasiparticle should have $\Gamma^{\rm qp}_m > 0$ [1], that is, the poles of the Green's function in Eq. (3.9) should be located in the lower-half of the complex plane.

However, a closer inspection of Eqs. (1.36) and (1.37) reveals that simply replacing $\omega \to z$ to account for complex arguments in these expressions gives functions with the reflection property $\Sigma(z^*) = \Sigma^*(z)$ and $G(z^*) = G^*(z)$, which are bounded except for possible branch-cut discontinuities along the real-axis (see Fig. 3.1(b)). This, in turn, implies that no solution of the quasiparticle equation Eq. (3.8) can be found in this way which satisfies causality [89].

Thus, the solution of Eq. (3.8) requires the analytic continuation of the self-energy accross the branch-cut from the upper-half to the so-called *unphysical* Riemann sheet on the-lower half of the complex plane [89], which we will denote by $\widetilde{\Sigma}(z)$. However, the analytic continuation process is well-known to be an extremely difficult problem from the numerical point of view. In this section, we review and improve on the existing numerical methods to achieve this task within the electron-phonon problem. We will start from simple models [5], which form the basis for the more general methods able to determine the complex quasiparticle energies in realistic materials.

[1] For simplicity, we only consider positive time differences $t-t' > 0$. This implies the use of the so-called *retarded* Green's functions [23], which are related to the spectral function by $G^R(\omega) = \int_{-\infty}^{\infty} \frac{d\omega'}{2\pi} \frac{A(\omega)}{\omega' - (\omega + i\eta)}$. In practice, this means that the sign of the infinitesimals $i\eta$ in Eqs. (1.33),(1.36) and (1.37) are set to $+$, so that the poles of the Green's functions lie in the lower-half of the complex plane for both occupied and unoccupied states.

Moreover, we generalize existing approaches [93] in order to treat more complicated systems beyond the approximations considered in conventional electron-phonon problems.

3.2.1 The Einstein model

The Einstein model is the simplest and most fundamental scenario in the context of electron-phonon interactions. It describes the coupling between free electrons and a single optical phonon with a fixed frequency ω_0, through a constant electron-phonon matrix element g_0. It is further assumed that the electrons disperse linearly close to the Fermi energy, so that the electronic density of states is constant. This simple model was analyzed in detail by Engelsberg and Schrieffer in their seminal work [5], which represents one of the first applications of field-theoretical methods to study the electron-phonon problem. As we will see in the next sections, this simple model results extremely helpful to develop general procedures able to describe the quasiparticle properties of complex systems. Moreover, it serves as a simple example to illustrate the concepts discussed in the previous sections.

Under the assumptions mentioned above, a closed analytical expression for the electron self-energy within the Einstein model can be obtained directly from Eq. (1.36) [2, 5, 27]. However, in order to obtain a proper analytic continuation of the self-energy which is continuous across the real-axis, it is useful to perform the integral of Eq. (1.36) at finite temperature and then take the $T \to 0$ limit at a later step. Defining $\lambda \equiv \frac{|g_0|^2}{\omega_0}$, the final result reads [93]

$$\widetilde{\Sigma}^{\mathrm{E}}(z,\omega_0) = \frac{\lambda\,\omega_0}{2}\left[-i\pi + \mathrm{Log}\left(\,i\omega_0 - iz\,\right) - \mathrm{Log}\left(\,-i\omega_0 - iz\,\right)\right] \tag{3.11}$$

whose real and imaginary parts on the real axis $z \to \omega + i\eta$ are shown for $\lambda = 1$ in Fig. 3.2(a) and (b), respectively. Its analytic structure on the whole complex plane is shown in Figs. 3.2(c) and (d), where it is appreciated that indeed $\widetilde{\Sigma}^{\mathrm{E}}(z)$ represents the analytic continuation of $\Sigma^{\mathrm{E}}(\omega)$ which is continuous across the real axis. The branch-cuts at $-\omega_0$ and ω_0 will be discussed further in Sec. 3.2.3.

The spectral function corresponding to the Einsteing model can be easily obtained from Eqs. (1.37),(3.4),(3.11),

$$\begin{aligned} A^{\mathrm{E}}_{\mathbf{k}}(\omega) &= -\frac{1}{\pi}\mathrm{Im}\left(\widetilde{G}^{\mathrm{E}}_{\mathbf{k}}(\omega)\right) \\ &= \frac{-(1/\pi)\,\mathrm{Im}\left(\widetilde{\Sigma}^{\mathrm{E}}(\omega,\omega_0)\right)}{\left[\omega - \varepsilon^0_{\mathbf{k}} - \mathrm{Re}\left(\widetilde{\Sigma}^{\mathrm{E}}(\omega,\omega_0)\right)\right]^2 + \left[\mathrm{Im}\left(\widetilde{\Sigma}^{\mathrm{E}}(\omega,\omega_0)\right)\right]^2}\,, \end{aligned} \tag{3.12}$$

where $\varepsilon^0_{\mathbf{k}} \propto (|\mathbf{k}| - |\mathbf{k}_F|)$ are the bare electron energies. We show in Fig. 3.3(a) the spectral function for $\varepsilon^0_{\mathbf{k}} = 1.5\,\omega_0$, where a prominent peak and a broad structure can be recognized.

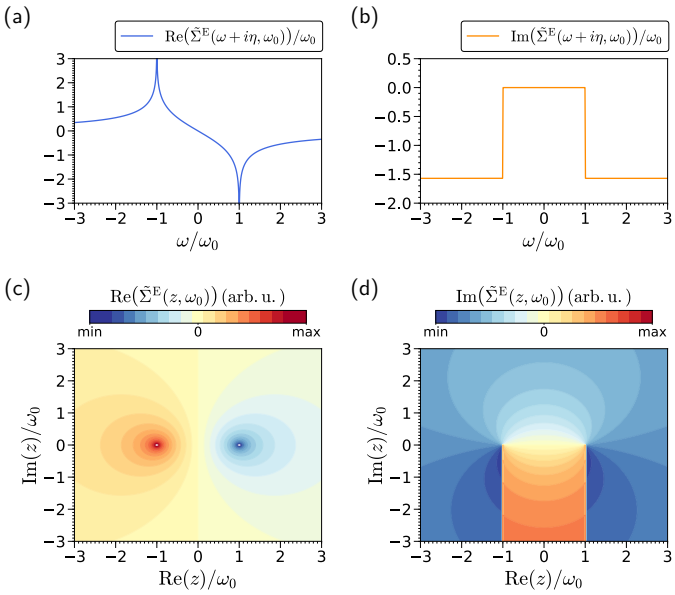

Figure 3.2. Electron-phonon self-energy in the Einstein model. (a),(b) Real and imaginary parts of the self-energy $\widetilde{\Sigma}^{\mathrm{E}}$, respectively, evaluated at the real-energy axis $z \to \omega + i\eta$. (c),(d) Real and imaginary parts of the analytic continuation of the self-energy to the non-physical Riemann sheet on the complex plane z.

The closed expression for the self-energy given by Eq. (3.11) allows us to represent $-\mathrm{Im}\left(\widetilde{G}^{\mathrm{E}}_{\mathbf{k}}(z)\right)$ on the whole complex plane by simply substituting $\omega \to z$ in Eq. (3.12), as shown in Fig. 3.3(b). Clearly, the main contributions to the spectral function can be identified to have their origin in two different poles, in line with the quasiparticle interpretation discussed in Sec. 3.1.

To formalize this interpretation, we can solve Eq. (3.8) for a set of **k**-points, as shown in Fig. 3.4. For example, for the **k**-point shown in Fig. 3.3 we find two solutions at the two poles of $\widetilde{G}^{\mathrm{E}}_{\mathbf{k}}(z)$. In Fig. 3.4(a), we show the real part of each quasiparticle pole $\varepsilon^{\mathrm{qp}}_{m\mathbf{k}}$, which gives the quasiparticle energy with respect to momentum **k**. The spectral weight, that is, the real part of the residue $\mathbb{Z}^{\mathrm{qp}}_{m\mathbf{k}}$ of each pole is represented by the length of the bars, and the imaginary part of the residue is represented by the rotation of the bars with respect to the vertical line, $\mathrm{Im}\left(\mathbb{Z}^{\mathrm{qp}}_{m\mathbf{k}}\right) = 1$ giving a rotation of $\theta = \pi$ radians. Finally, the imaginary part of the quasiparticle poles $\Gamma^{\mathrm{qp}}_{m\mathbf{k}}$, which gives quasiparticle lifetime broadening, is shown in Fig. 3.4(b) with respect to the quasiparticle energy $\varepsilon^{\mathrm{qp}}_{m\mathbf{k}}$. In this way, Fig. 3.4 represents the full complex quasiparticle band structure within the Einstein model.

The quasiparticle picture facilitates the understanding of the effects driven by the electron-phonon in the electronic band structures, which even in the case of the simplest Einstein model are profound. From Fig. 3.4 we infer that the spectral weight corresponding to a single electron band

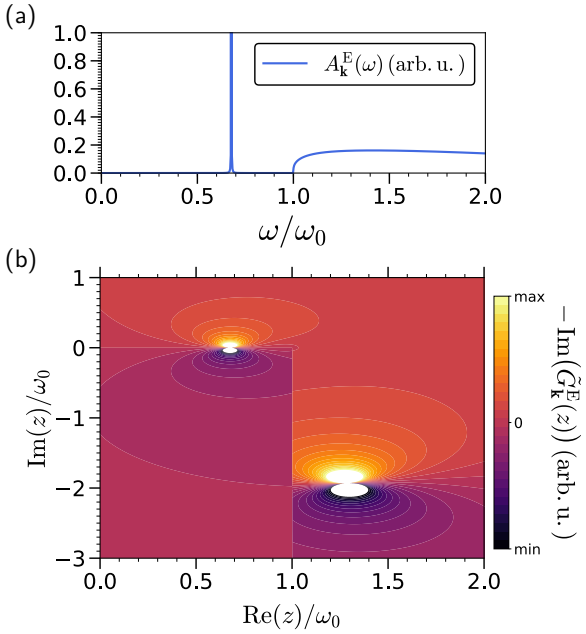

Figure 3.3. Electron spectral function in the Einstein model. (a) Spectral function $A^{\mathrm{E}}_{\mathbf{k}}(\omega)$, given by Eq. (3.12), for $\varepsilon^0_{\mathbf{k}} = 1.5\omega_0$. (b) Analytic structure of $\widetilde{G}^{\mathrm{E}}_{\mathbf{k}}(z)$ on the complex plane z, whose imaginary part evaluated at the real axis gives the spectral function. The color code represents $-\mathrm{Im}\left(\widetilde{G}^{\mathrm{E}}_{\mathbf{k}}(z)\right)$ in arbitrary units.

splits into two separate quasiparticle bands. Below the phonon frequency ω_0, the electrons do not have sufficient energy for emitting any phonon, and therefore they appear infinitely long lived. However, they are allowed to emit and reabsorb phonons in virtual processes, which produces a phonon cloud around electrons having the effect of augmenting their effective mass and flatten their dispersion. For electrons above ω_0, on the other hand, the emission of real phonons is energetically allowed, which leads to a decrease of their lifetime. The probability of virtual emission and absorption processes is smaller for energies far from ω_0, so that the dispersion of the quasiparticles resembles the one of the non-interacting electrons. For bare electron energies close to ω_0 both processes are possible, and the total spectral weight splits into the two states.

In the next sections, we will see that this idealized picture qualitatively holds in the general case where more intricate electron band structures, phonon dispersions and electron-phonon interactions are present.

3.2.2 The Debye model and piecewise polynomial method

The simplifications adopted in the previous section allowed us to obtain a closed expression for the electron-phonon self-energy also in the non-physical

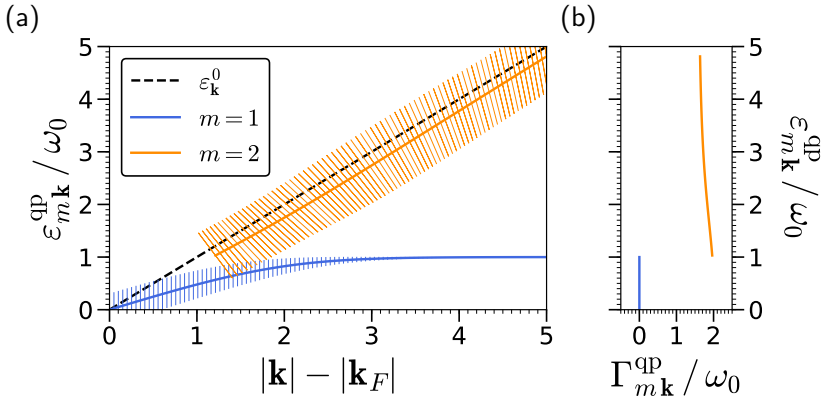

Figure 3.4. Quasiparticle band structure in the Einstein model. (a) Real part of the quasiparticle poles, that is, the quasiparticle energies $\varepsilon^{\mathrm{qp}}_m$, for different values of the magnitude of the momentum $\mathbf{k}$ with respect to the Fermi momentum $\mathbf{k}_F$. The bare electron energy $\varepsilon^0_{\mathbf{k}}$ is represented by the dashed black line, and the two solutions for the quasiparticle equation Eq. (3.8) are represented by the blue and orange lines, respectively. The length of the bars represents the real part of the residue of each pole, $\mathrm{Re}\,(\mathbb{Z}^{\mathrm{qp}}_m)$, which gives the spectral weight corresponding to each quasiparticle. The imaginary part of the residues is represented by the rotation of the bars, $\mathrm{Im}\,(\mathbb{Z}^{\mathrm{qp}}_m) = 1$ giving a rotation of $\theta = \pi$ radians. (b) Negative of the imaginary part of the quasiparticle poles, that is, the inverse quasiparticle lifetime Γ^{qp}_m, with respect to the quasiparticle energies. The color code is the same as in (a).

Riemann sheet, which provided the proper analytic continuation needed to determine the complex quasiparticle energies. However, the Einstein model represents a highly idealized situation, and in the general case complicated phonon dispersions and electron-phonon coupling matrix elements have to be considered.

Still, for most metals, some reasonable approximations can be made to simplify Eq. (1.36). Given the notable difference between the electronic energy scales ($\sim$ eV) and the energy scale of phonons ($\sim$ meV), the strongest renormalization of electronic states driven by the electron-phonon interaction will happen on a narrow window around the Fermi energy. The density of states can be considered to be constant within this narrow window, and, moreover, the energy-dependence of the electron-phonon matrix elements can be neglected while keeping the momentum dependence [22]. In this way, the electron-phonon self-energy for an electronic state $n\mathbf{k}$ can be rewritten as [22, 93],

$$\widetilde{\Sigma}_{n\mathbf{k}}(z) = \int_0^\infty d\omega\, \alpha^2 F_{n\mathbf{k}}(\omega)\, \left[-i\pi + \mathrm{Log}\,(\,i\omega - iz\,) - \mathrm{Log}\,(\,-i\omega - iz\,)\right]\ , \tag{3.13}$$

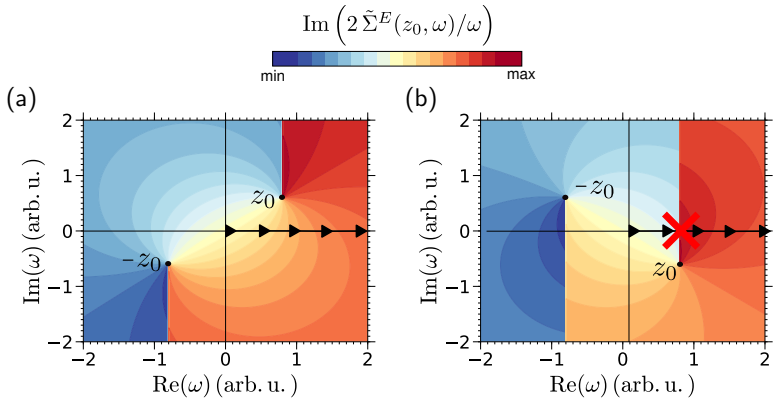

Figure 3.5. Schematic representation of the integral of Eq. (3.13). The color code represents the imaginary part of the integrand on the complex ω-plane for different values of z in which the self-energy is evaluated. (a) For $\mathrm{Im}\,(z) > 0$, the contour along the real-axis allows for a direct numerical evaluation of the integral. (b) For $\mathrm{Im}\,(z) < 0$, the numerical integral along the real-axis is not well defined, as the branch cut of the integrand crosses the real-axis.

where we have defined the so-called Eliashberg function [2],

$$\alpha^2 F_{n\mathbf{k}}(\omega) = \sum_{m\nu} \int \frac{d\mathbf{q}}{\Omega_{\mathrm{BZ}}} \left|g^{\nu}_{mn}(\mathbf{k},\mathbf{q})\right|^2 \delta(\varepsilon_{n\mathbf{k}} - \varepsilon_{m\mathbf{k}-\mathbf{q}})\,\delta(\omega - \omega_{\mathbf{q}\nu})\ . \tag{3.14}$$

Remarkably, the Einstein self-energy of Eq. (3.11) can be recognized in the term within brackets of Eq. (3.13). Thus, the general self-energy may be interpreted as the superposition of effective Einstein modes of frequency ω, where $\alpha^2 F_{n\mathbf{k}}(\omega)$ represents the interaction strength of the state $n\mathbf{k}$ with each effective mode [93].

Given that the analytic structure of the term within brackets is known, and since the Eliashberg function of Eq. (3.14) can be numerically computed from first principles (see Sec. 1.4.3), Eq. (3.13) provides a way to obtain the analytic continuation of the electron self-energy from the upper to the lower half of the complex plane for any arbitrary system. Nevertheless, a close inspection of the integrand shows that the branch-cut discontinuities introduced by the logarithm terms make the direct numerical integration (i.e. a Riemann summation) of Eq. (3.13) inappropriate for values of z with $\mathrm{Im}(z) < 0$, as shown schematically in Fig. 3.5. A possible strategy to overcome this difficulty is to solve the integral analytically.

The simplest case in which this can be done — beyond the Einstein model $\alpha^2 F^E(\omega) \equiv \frac{\lambda\omega_0}{2}\delta(\omega - \omega_0)$) — is the so-called Debye model [2, 5], which describes the coupling of electrons to a linearly dispersing acoustic phonon mode through a constant matrix element. Thus, the corresponding Eliashberg function is defined to be proportional to the phonon density of

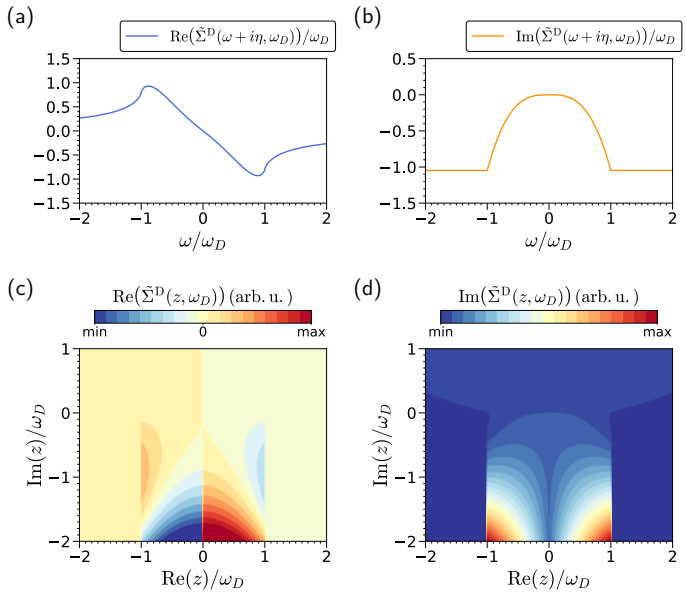

Figure 3.6. Electron-phonon self-energy in the Debye model. (a),(b) Real and imaginary parts of the self-energy $\widetilde{\Sigma}^{\mathrm{D}}$, respectively, evaluated at the real-energy axis $z \to \omega + i\eta$. (c),(d) Real and imaginary parts of the analytic continuation of the self-energy to the non-physical Riemann sheet on the complex plane z.

states,

$$\alpha^2 F^D(\omega) \equiv \frac{\lambda\,\omega^2}{2\,\omega_D^2}\,\theta(\omega_D - \omega)\ , \tag{3.15}$$

where θ is the Heaviside step function, and ω_D is the so-called Debye frequency, giving the maximum frequency of the acoustic mode. The polynomial character of the Eliashberg function allows for the analytical integration of Eq. (3.13) by parts. For completeness we give the result, which reads [93]

$$\begin{aligned}\widetilde{\Sigma}^{\mathrm{D}}(z,\omega_D) = \frac{\lambda\,\omega_D}{3}\Bigg[&-i\pi - \frac{z}{\omega_D} + \frac{2\,z^3\,\mathrm{Log}\left(-\frac{iz}{2}\right)}{\omega_D^3} \\ &+ \left(1 - \frac{z^3}{\omega_D^3}\right)\mathrm{Log}\left(\frac{i}{2}(\omega_D - z)\right) \\ &- \left(1 + \frac{z^3}{\omega_D^3}\right)\mathrm{Log}\left(-\frac{i}{2}(\omega_D + z)\right)\Bigg]\ .\end{aligned} \tag{3.16}$$

We represent in Fig. 3.6 the analytic structure of the electron self-energy within the Debye model, given by the evaluation Eq (3.16). As it is appreciated in this figure, Eq. (3.16) indeed gives the analytic continuation of the self-energy which is continuous across the real-axis.

Most importantly, the Debye model provides a roadmap for a possible numerical strategy to obtain the proper analytic continuation of the self-energy.

If the frequency-dependence of the Eliashberg function is approximated by a piecewise-polynomial function, the integral of Eq. (3.13) can be split into intervals, and solved analytically for each interval [93]. The sum of the analytic contributions of each interval will give the proper analytic continuation of the full self-energy. A practical implementation of this procedure will be detailed in Sec. 3.3.

3.2.3 Deformed contour integral and multiple Riemann sheets

As discussed throughout this chapter, the electron self-energy is a multivalued function on the complex plane. As shown in Secs. 3.2.1 and 3.2.2, it is possible to obtain the analytic continuation of the self-energy which is continuous across the real-axis to the so-called unphysical Riemann sheet, which does provide solutions of the quasiparticle equation Eq. (3.8) on the lower-half of the complex plane. However, from Fig. 3.2 it appears clear that the self-energy still displays branch-cut discontinuities on the lower-half of the complex plane, which make the quasiparticle band structure discontinuous (see Fig. 3.4). These discontinuities may in turn reproduce themselves in the general self-energies through the evaluation of Eq. (3.13), as it is appreciated in Fig. 3.6 for the Debye self-energy. Nonetheless, it is not obvious how one could have access to all the Riemann sheets that may give a contribution to the spectral function on the real-axis.

One possible approach can be deduced from the interpretation of Eq. (3.13) as a line integral over the real-axis on the complex ω-plane, as shown schematically in Fig. 3.5. Instead of restricting the line integral to the real-axis, and the values of the integrand to its principal branch, one can deform the integration contour to move continuously through the different sheets of the multivalued integrand.

We illustrate this procedure in the Debye model. In Fig. 3.7(a) we show the imaginary part of the integrand in Eq. (3.13), that is basically the Einstein self-energy of Fig. 3.2 composed by multivalued logarithm terms. Thus, at the ending point of the integral, which is the Debye frequency ω_D on the real-axis of the ω-plane, the integrand can take multiple values. As already discussed in Fig. 3.5, considering only the principal branch of the integrand makes the integration on the real-axis impossible for values of z with $\mathrm{Im}(z) < 0$, as a branch cut crosses the real-ω-axis in this case. However, taking into account its multivaluedness, it is possible to define different deformed integration contours which, although finishing at the same point in the ω-plane — ω_D in this case —, move continuously through the different sheets of the integrand. For example, two contours passing below and above the branch-point at $\omega = z_0$ are represented by $\mathcal{C}^1_{\{0,\omega_D\}}$ and $\mathcal{C}^2_{\{0,\omega_D\}}$, respectively, in Fig. 3.7(a).

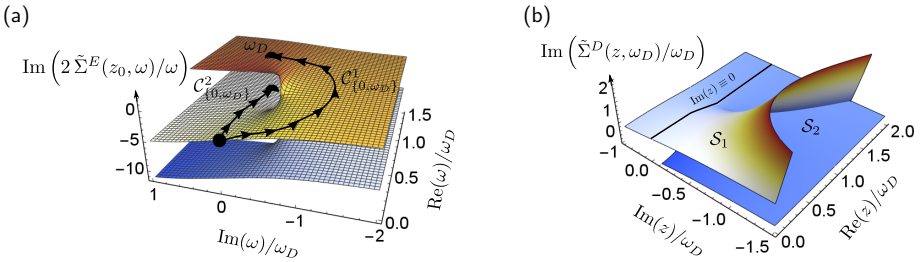

Figure 3.7. Multiple Riemann sheets in the self-energy. (a) Imaginary part of the multivalued term within brackets of the integrand of Eq. (3.13) on the complex ω-plane. Two possible contours which are continuous from $\omega = 0$ to $\omega = \omega_D$ through the different sheets are represented by $\mathcal{C}^1_{\{0,\omega_D\}}$ and $\mathcal{C}^2_{\{0,\omega_D\}}$, respectively. (b) The corresponding multivalued self-energy $\tilde{\Sigma}(z)$, obtained through the evaluation of Eq. (3.13) on the complex z-plane. The different Riemann sheets corresponding to the contours $\mathcal{C}^1_{\{0,\omega_D\}}$ and $\mathcal{C}^2_{\{0,\omega_D\}}$ are represented by $\mathcal{S}_1$ and $\mathcal{S}_2$, respectively. Each sheet is continuous across a particular region of the real-z-axis, highlighted by the black line.

Clearly, the evaluation of Eq. (3.13) through the different contours will result in multiple values of $\tilde{\Sigma}(z)$ for the same z. We illustrate in Fig. 3.7(b) the multivalued self-energy obtained in the Debye model from the contours $\mathcal{C}^1_{\{0,\omega_D\}}$ and $\mathcal{C}^2_{\{0,\omega_D\}}$ of Fig. 3.7(a), where the corresponding different Riemann sheets are denoted by $\mathcal{S}_1$ and $\mathcal{S}_2$, respectively. As it can be appreciated in this figure, both sheets are continuous towards the upper-half plane across a region of the real-z-axis, highlighted by a black line in Fig. 3.7(b). The upper $\mathcal{S}_1$ sheet is continuous for $\mathrm{Re}(z) < \omega_D$, and the lower $\mathcal{S}_2$ sheet is continuous for $\mathrm{Re}(z) > \omega_D$. By picturing the integrand for changing values of $\mathrm{Im}(z)$ from positive to negative, one sees that indeed the contours $\mathcal{C}^1_{\{0,\omega_D\}}$ and $\mathcal{C}^2_{\{0,\omega_D\}}$ are the ones that keep the value of the integrand at ω_D on the same sheet as in $\mathrm{Im}(z) > 0$ for each case. We note that for each region of $\mathrm{Re}(z)$, the corresponding continuous sheet to the lower-half of the complex plane gives the same result as obtained by the analytical integration of Eq. (3.16) (see Fig. 3.6).

Considering only the branch of the self-energy which is continuous across the real-axis, as in Figs. 3.2 and 3.6, will be typically sufficient to obtain a good approximation of the spectral function through the solutions of the quasiparticle equation Eq. (3.8) sought in this branch. However, in some cases, looking for extra poles in the multiple Riemann sheets discussed above will be useful to obtain a continuous quasiparticle band structure.

One of such cases within the Debye model is shown in Fig. 3.8. In Fig. 3.8(a), we represent the full spectral function for $\varepsilon_{\mathbf{k}_0} = 0.8\,\omega_D$ by a gray line, which displays a clear peak at $\omega \sim 0.5\,\omega_D$ and a bump at $\omega \sim 1.1\,\omega_D$. In Fig. 3.8(b), we show the analytic continuation of the Green's function

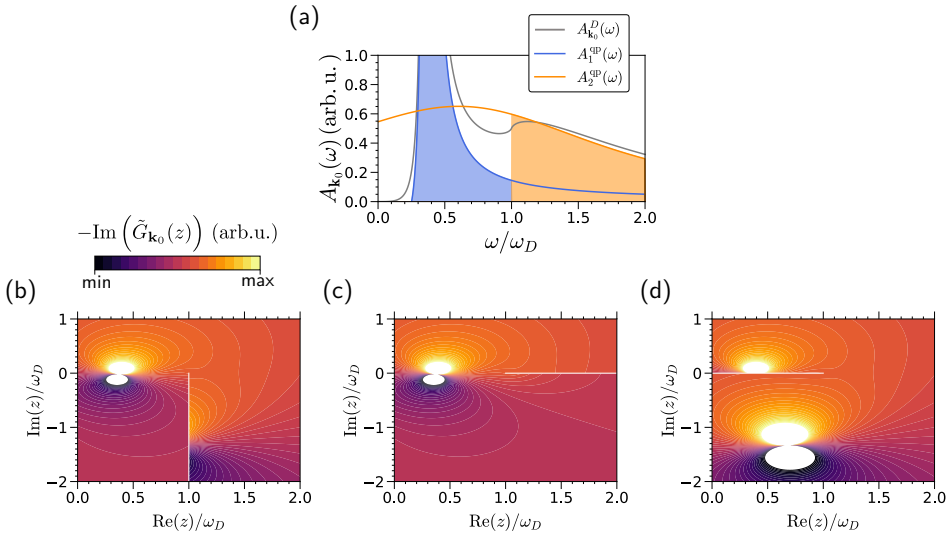

Figure 3.8. Contribution to the spectral function from the poles at the multiple sheets. (a) The full spectral function within the Debye model for $\varepsilon_{\mathbf{k}_0} = 0.8\,\omega_D$. The contributions from the two separate poles coming from the different Riemann sheets are represented by the blue and orange shaded areas, respectively. Each pole only contributes to the region on the real-z-axis on which its Riemann sheet is continuous. (b) Analytic continuation of the Green's function for the branch which is continuous across the real-axis, as given by Eq. (3.16). (c),(d) Analytic continuation of the Green's function for the two $\mathcal{S}_1$ and $\mathcal{S}_2$ Riemann sheets of Fig. 3.7, respectively. The pole of $\tilde{G}_{\mathbf{k}_0}(z)$ on $\mathcal{S}_2$ clearly recognized in (d) is hidden in the branch which is continuous across the real-axis, shown in (b).

which is continuous across the real-axis, as given by Eq. (3.16). Clearly, the origin of the main peak on the spectral function can be recognized to come from a pole very close to the real-axis. However, no pole can be found strictly in this branch which may account for the bump at $\omega > \omega_D$. Still, from the colormap one can deduce that it is hidden below the branch-cut.

The analytic continuation of the Green's function for the two sheets $\mathcal{S}_1$ and $\mathcal{S}_2$ are shown in Figs. 3.8(c) and (d), respectively. As expected, another pole can be found in the lower $\mathcal{S}_2$ sheet, clearly recognized in Fig. 3.8(d). We represent the separate contributions of each pole to the spectral function through each sheet [see Eq. (3.9)] by the blue and orange shaded areas in Fig. 3.8(a), respectively. Each pole only contributes to the region on the real-ω-axis on which its Riemann sheet is continuous. As compared to the single-pole contribution that one could find only in the continuous branch across the real-axis, represented by the solid blue line, a much better approximation to the full spectral function can be obtained in this way. Still, the simple summation of both contributions does not account for the full

spectral function, meaning that the self-energy introduces fine details on the Green's function beyond the standard quasiparticle approximation.

3.2.4 Extension to general self-energies

The procedure reviewed in Sec. 3.2.2 is valid for the analytical continuation of the electron-phonon self-energy in most of the cases in which this interaction is relevant, namely for electrons close to the Fermi surface in conventional metals. However, for some interesting cases, like the one we will present in Sec. 3.3, the approximation of constant density of states and particle-hole symmetry needed to get to Eq. (3.13) does not hold, and the more general self-energy of Eq. (1.36) has to be used in order to obtain correct spectral functions.

Following the essence of Eq. (3.13), we will try to look for an expression of the self-energy which is composed by a function whose analytical continuation is known — such as the logarithm —, and a more complicated function which can be computed numerically on the real-axis.

The starting point for our derivation is the Kramers-Kronig relation for the retarded self-energy on the real axis [27],

$$\mathrm{Re}\left(\Sigma_{n\mathbf{k}}(\omega)\right) = \frac{1}{\pi}\,\mathcal{P}\int_{-\infty}^{\infty} d\omega'\,\frac{\mathrm{Im}\left(\Sigma_{n\mathbf{k}}(\omega')\right)}{\omega'-\omega}\ . \tag{3.17}$$

Recalling that $(\omega' \pm i\eta)^{-1} = \mathcal{P}(1/\omega') \pm i\pi\delta(\omega')$, the full self-energy can be retrieved from the knowledge of its imaginary part on the real axis only,

$$\Sigma_{n\mathbf{k}}(\omega) = \frac{1}{\pi}\int_{-\infty}^{\infty} d\omega'\,\frac{\mathrm{Im}\left(\Sigma_{n\mathbf{k}}(\omega')\right)}{\omega'-\omega+i\eta}\ . \tag{3.18}$$

We can now integrate by parts, getting

$$\Sigma_{n\mathbf{k}}(\omega) = -\frac{1}{\pi}\int_{-\infty}^{\infty} d\omega'\,\frac{d\,\mathrm{Im}\left(\Sigma_{n\mathbf{k}}(\omega'')\right)}{d\,\omega''}\bigg|_{\omega''=\omega'}\mathrm{Log}(\omega'-\omega+i\eta)+\mathcal{C}\ , \tag{3.19}$$

where,

$$\mathcal{C} = i\,\mathrm{Im}\left(\Sigma_{n\mathbf{k}}(\omega\to\infty)\right) = i\int_{0}^{\infty} d\omega'\,\frac{d\,\mathrm{Im}\left(\Sigma_{n\mathbf{k}}(\omega'')\right)}{d\,\omega''}\bigg|_{\omega''=\omega'}\ . \tag{3.20}$$

The analytic continuation of the self-energy similar to Eq. (3.13) can now be obtained by substituting $\omega \to z$, and choosing the proper sheet of the logarithm term by summing $-\frac{i\pi}{2} + \mathrm{Log}(i) = 0$ in the integrand,

$$\widetilde{\Sigma}_{n\mathbf{k}}(z) = -\frac{1}{\pi}\int_{-\infty}^{\infty} d\omega'\,\frac{d\ \mathrm{Im}\left(\Sigma_{n\mathbf{k}}(\omega'')\right)}{d\,\omega''}\bigg|_{\omega''=\omega'}\left(-\frac{i\pi}{2}+\mathrm{Log}(i\omega'-iz)\right)+\mathcal{C}\ , \tag{3.21}$$

where the infinitesimal $\eta \to 0^+$ has been absorbed into z in the logarithm term.

If particle-hole symmetry is present, and under the same approximations leading to Eq. (3.13), we have that [22],

$$\frac{1}{\pi}\frac{d\ \mathrm{Im}\left(\Sigma_{n\mathbf{k}}(\omega'')\right)}{d\,\omega''}\bigg|_{\omega''=-\omega'} = -\frac{1}{\pi}\frac{d\ \mathrm{Im}\left(\Sigma_{n\mathbf{k}}(\omega'')\right)}{d\,\omega''}\bigg|_{\omega''=\omega'} = \alpha^2 F_{n\mathbf{k}}(\omega')\ , \tag{3.22}$$

and Eq. (3.13) can be retrieved from Eq. (3.21).

Nonetheless, Eq. (3.21) is much more general and goes beyond these approximations. Indeed, as this expression originates from the general Kramers-Kronig relation of Eq. (3.17), it is in principle applicable to any self-energy, including, for example, the electron-electron self-energy. In Sec. 3.3 we will use this expression together with the piecewise-polynomial method to identify the complex quasiparticle poles in the intricate spectra of doped monolayer MoS_2. In this system, the electron-phonon self-energy lies outside the range of validity of the approximated Eq. (3.13), and the full self-energy of Eq. (1.36) has to be used.

3.3 Complex quasiparticle band structure in the doped monolayer MoS_2

In the previous section, we have discussed different methods to obtain the analytical continuation of the electron-phonon self-energy to the unphysical Riemann sheet in a general way. In this section, we put the procedures discussed above into practice, and determine the complex quasiparticle band structure of a realistic system starting from first principles calculations.

The system we will study is the doped monolayer MoS_2 [14], where the possibility of systematic doping together with high resolution photoemission experiments has allowed to uncover a genuine many-body electron spectrum [87]. Being a doped semiconductor, its density of states close to the Fermi energy is far from being constant. Moreover, its complicated band structure composed of spin-split valleys at high-symmetry points of the Brillouin zone, makes the electron-phonon interaction particularly unconventional in this system [18, 94–96]. Thus, the full self-energy of Eq. (1.36) has to be evaluated explicitly for a proper description of the measured spectral function. This makes the use of Eq. (3.21) derived in Sec. 3.2.4 mandatory for the analytic continuation of the self-energy. In this thesis, we will focus in the determination of the quasiparticle properties of the system. All the details about the first principles calculations can be found in [14].

In Fig. 3.9 we show the spectral function $A_{\mathbf{k}}(\omega)$ of MoS_2 considering a doping carrier density of $n = 9 \times 10^{13}\mathrm{cm}^{-1}$, for which the conduction-band minima at $\overline{\mathrm{K}}$ are filled with a binding energy of $E_{\overline{\mathrm{K}}} = 118$ meV, while only

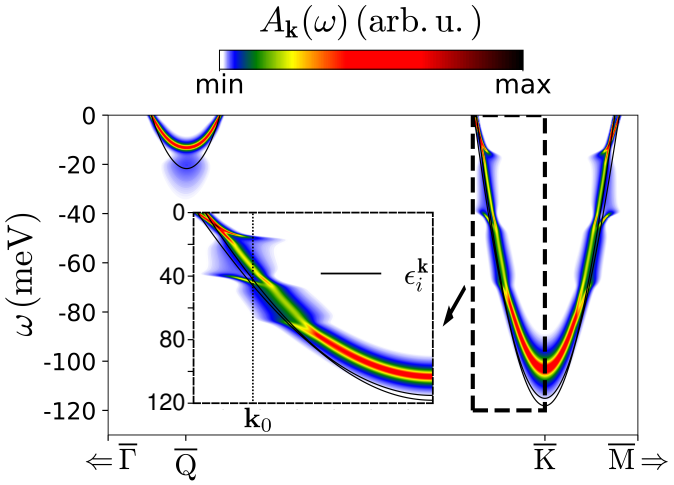

Figure 3.9. Electron spectral function for doped MoS_2 along the high-symmetry points of the Brillouin zone, calculated from first-principles including electron–phonon interaction effects [14]. The solid black lines represent the non-interacting electron bands. The dashed rectangle highlights the area of the Brillouin zone where the strongest renormalization of the electronic bands occur. The dotted line on the inset shows the momentum $\mathbf{k} = \mathbf{k}_0$ in which the self-energy is evaluated in Figs. 3.10–3.12.

the lower spin-split states are populated at $\overline{\mathrm{Q}}$ with a binding energy of $E_{\bar{\mathrm{Q}}} = 22$ meV. The spectral function has been calculated directly on the real axis in a similar way as in Eq. (3.12), but using the full self-energy of Eq. (1.36), in which all the components have been computed from first principles DFT and DFPT calculations (see Sec. 1.4 for a brief description of the adopted approximations).

The agreement with the experimentally measured ARPES spectra is remarkably good [87]. This indicates that carefully considering the details of the electron-phonon interaction within the Migdal approximation already accounts for the observed strong renormalization of the electronic bands. We show a zoom on the region of the Brillouin zone in which this renormalization is strongest in the inset of Fig. 3.9. Notably, the electron-phonon interaction is stronger in the outer spin-split band, owing to the interplay of the electron-phonon matrix-elements with the out-of-plane spin-polarization of the electronic bands at different valleys [14]. For completeness, we represent the non-interacting DFT bands by black solid lines in Fig. 3.9.

In order to illustrate the practical numerical workflow for the analytic continuation of the self-energy, we first focus on the outer spin-split band, and on a single $\mathbf{k}$-point close to the Fermi-momentum at the $\overline{\mathrm{K}}$ valley, represented by $\mathbf{k}_0$ and a dotted line in the inset of Fig. 3.9. We will use the piecewise-polynomial method described in Sec. 3.2.2, together with the

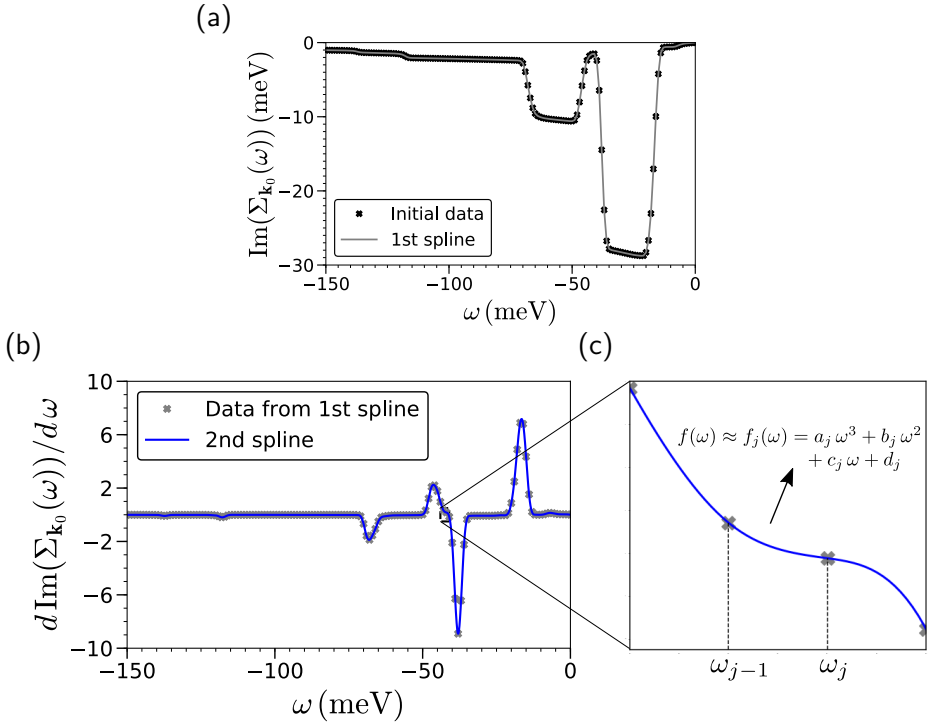

Figure 3.10. Spline interpolation of the electron-phonon self-energy. (a) The imaginary part of the self-energy at $\mathbf{k} = \mathbf{k}_0$ is evaluated on a regular grid of $\{\omega_i\}$ points in the real-axis through Eq. (1.36), as represented by the black crosses. A spline interpolation, represented by the gray line, is performed over this set of data. (b) The first spline interpolation is used to generate an accurate derivative in a denser grid $\{\omega_j\}$, shown by the gray crosses. A second spline interpolation is performed over the dense data set, as represented by the blue line, in order to define a piecewise-polynomial function approximating the continuous derivative of the self-energy on the real-axis. (c) Zoom over a particular region of the ω-axis.

formula Eq. (3.25) derived in Sec. 3.2.4 valid for the analytical continuation of a general self-energy.

Our first goal will be to interpolate the derivative of the imaginary part of the self-energy, $\frac{d\,\mathrm{Im}(\Sigma_{n\mathbf{k}}(\omega))}{d\,\omega}$, as a piecewise-polynomial function. With the aim of obtaining an accurate and smooth derivative, we will follow a two-step cubic spline interpolation process, as shown in Fig. 3.10. Usually, what is computed from first principles is the imaginary part of the self-energy on a regular grid of real frequencies $\{\omega_i\}$, as represented by the black crosses in Fig. 3.10(a). We compute the derivative of the self-energy by interpolating $\{\mathrm{Im}\,(\Sigma_{n\mathbf{k}}(\omega_i))\}$ through a cubic spline, and evaluating its first derivative on another grid of real frequencies $\{\omega_j\}$, which can be finer than the initial grid if needed. Then, the coefficients of the piecewise-polynomial function approximating the derivative of the self-energy, which will be used to integrate

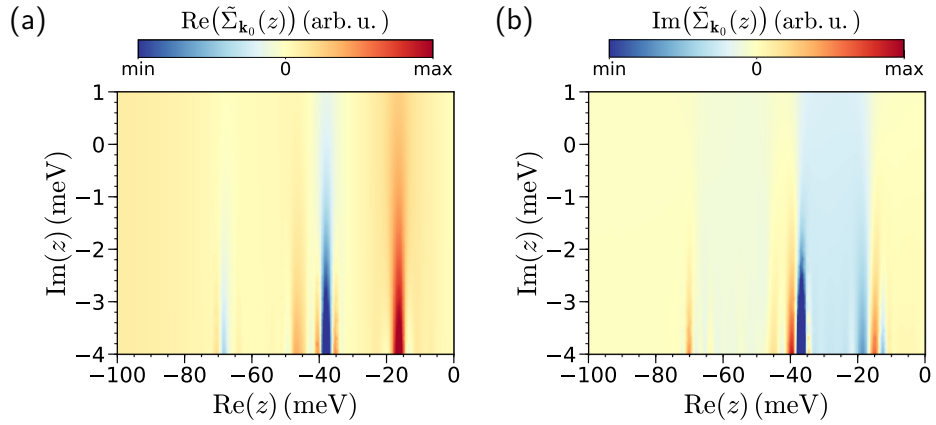

Figure 3.11. Analytic continuation of the electron-phonon self-energy in MoS_2. (a),(b) Real and imaginary parts of $\widetilde{\Sigma}_{\mathbf{k}_0}(z)$, respectively, evaluated through Eq. (3.25) on a region of the complex z-plane. The function is continuous across the real-axis from the upper to the lower half of the complex plane.

Eq. (3.21), are obtained by interpolating this finer data points by a second cubic spline. Explicitly, we have that [97, 98]

$$\frac{d\ \mathrm{Im}\left(\Sigma_{n\mathbf{k}}(\omega)\right)}{d\,\omega} = f(\omega) \approx \begin{cases} f_1(\omega-\omega_0) & , \quad \omega_0 \leq \omega < \omega_1 \\ \vdots & \vdots \\ f_j(\omega-\omega_{j-1}) & , \quad \omega_{j-1} \leq \omega < \omega_j \\ \vdots & \vdots \\ f_N(\omega-\omega_{N-1}) & , \quad \omega_{N-1} \leq \omega \leq \omega_N \end{cases} , \tag{3.23}$$

where

$$f_j(\omega) = d_j\,\omega^3 + c_j\,\omega^2 + b_j\,\omega + a_j\ , \tag{3.24}$$

and the coefficients a_j, b_j, c_j and d_j are determined by forcing the continuity of the function and its first and second derivatives over the intervals, together with the boundary conditions $f''(\omega_0) = f''(\omega_N) = 0$.

In this way, we can apply the method reviewed in Sec. (3.2.2), and perform the integral of Eq. (3.21) analytically on each interval. For completeness, we

give the general result, which reads

$$\begin{aligned}
\widetilde{\Sigma}_{n\mathbf{k}}(z) &\approx -\frac{1}{\pi}\sum_{j}^{N}\int_{\omega_{j-1}}^{\omega_j} d\omega'\, f_j(\omega'-\omega_{j-1})\left(-\frac{i\pi}{2}+\mathrm{Log}(i\omega'-iz)\right)+\mathcal{C}\\
&= -\frac{1}{\pi}\sum_{j}^{N}\Big[\frac{1}{144}(\omega'-z)\left(12\,\mathrm{Log}\left(i(\omega'-z)\right)\right)\left(12a_j+6b_j(\omega'-2\omega_{j-1}+z)\right.\\
&\quad+4c_j\left((\omega')^2+\omega'(z-3\omega_{j-1})+3\omega_{j-1}^2-3\omega_{j-1}z+z^2\right)\\
&\quad\left.+3d_j(\omega'-2\omega_{j-1}+z)\left((\omega')^2-2\omega'\omega_{j-1}+2\omega_{j-1}^2-2\omega_{j-1}z+z^2\right)\right)\\
&\quad-72i(\pi-2i)(a_j-(\omega_{j-1}-z)(b_j-(\omega_{j-1}-z)(c_j-d_j\omega_{j-1}+d_jz)))\\
&\quad-36i(\pi-i)(\omega'-z)(b_j+(\omega_{j-1}-z)(3d_j(\omega_{j-1}-z)-2c_j))\\
&\quad-8(2+3i\pi)(\omega'-z)^2(c_j+3d_j(z-\omega_{j-1}))\\
&\quad-9i(2\pi-i)d_j(\omega'-z)^3\Big)\Big]_{\omega_{j-1}}^{\omega_j}\quad+\quad\mathcal{C}\ .
\end{aligned}\tag{3.25}$$

This expression, although rather lengthy, allows to approximate the numerical evaluation of the analytic continuation of a general self-energy as a simple summation. We illustrate this in Fig. 3.11, where we show the analytic continuation of the numerically evaluated electron-phonon self-energy for MoS_2 at $\mathbf{k}=\mathbf{k}_0$. Clearly, the self-energy for this realistic case is much more complicated than the self-energy of the Einstein model shown in Fig. 3.2. However, the important aspect is that this function is continuous across the real-axis, demonstrating that Eq. (3.25) actually gives the proper analytic continuation of the self-energy needed to solve Eq. (3.8) on the complex plane. Solutions of this equation on the multiple Riemann sheets as discussed in Sec. 3.2.3 will not be sought, as the poles found on the branch which is continuous across the real-axis will already give a proper account for the spectral function, as we will see below.

We illustrate this point more explicitly in Fig. 3.12. For completeness, we show in Fig. 3.12(a) the spectral function for $\mathbf{k}=\mathbf{k}_0$ on the real-energy axis, where two clear peaks and a small bump can be observed for energies around $-15\,\mathrm{meV}$, $-45\,\mathrm{meV}$ and $-65\,\mathrm{meV}$, respectively. By plotting the imaginary part of the analytical continuation of the Green's function on the complex plane (see Fig. 3.12(b)), obtained by substituting $\omega\to z$ and $\Sigma(\omega)\to\widetilde{\Sigma}(z)$ in Eq. (1.37), we recognize the origin of the two strongest peaks in two clear poles close to the real-axis. Similarly, the origin of the bump can be traced back to a pole with a smaller residue deeper in the imaginary axis at $\mathrm{Re}(z)\sim-70\,\mathrm{meV}$.

Finally, we represent graphically the real and the imaginary components of the quasiparticle equation Eq. (3.8) by the blue and orange contours in Fig. 3.12(c), respectively. This figure demonstrates that the poles of $\tilde{G}_{\mathbf{k}_0}(z)$ can be determined by the self-consistent solutions of Eq. (3.8), that is, by

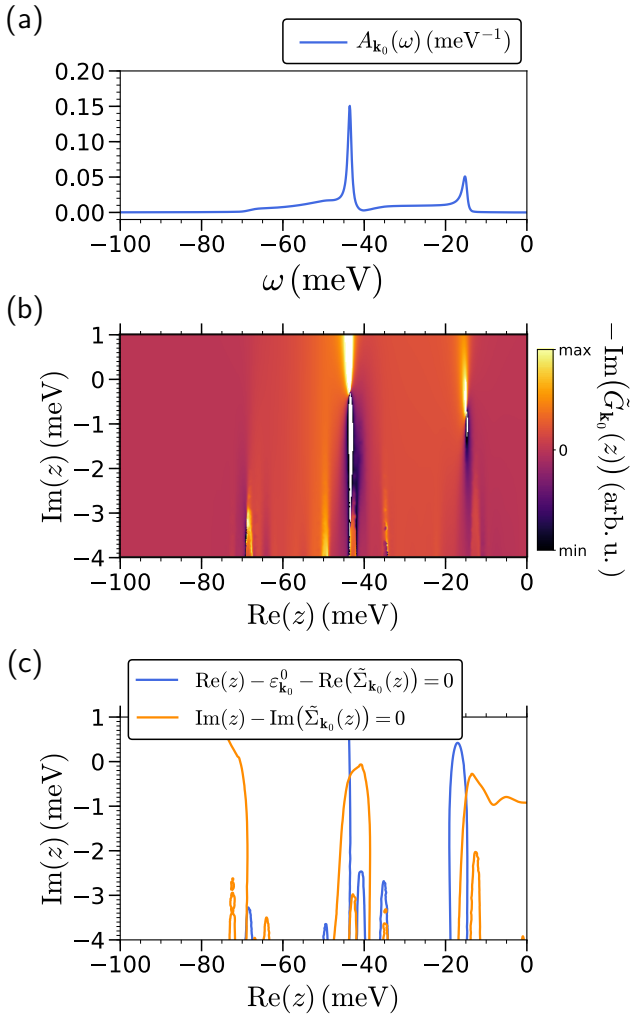

Figure 3.12. Spectral function and complex quasiparticle poles in MoS_2. (a) Spectral function at $\mathbf{k} = \mathbf{k}_0$ evaluated on the real-energy axis. (b) Imaginary part of the analytic continuation of the Green's function on the complex z-plane, $-\mathrm{Im}\left(\tilde{G}_{\mathbf{k}_0}(z)\right)$, obtained by substituting $\omega \to z$ and $\Sigma(\omega) \to \widetilde{\Sigma}(z)$ in Eq. (1.37). Three poles can be identified as the origin of the peaks on the real-axis. (c) Graphical solution of the quasiparticle equation Eq. (3.8). The real and imaginary components of the equation are shown in blue and orange, respectively. The crossing points correspond to self-consistent solutions, that is, quasiparticle energies.

the crossing points of the two contours in Fig. 3.12(c). In practice, these solutions have been found by a complex version of the Newton root-finding method [93].

Following the same procedure for all the $\mathbf{k}$-points on the Brillouin zone, we can obtain the full quasiparticle band structure of the system. We show in Fig. 3.13(a),(b) the results for the outer spin-split band of doped

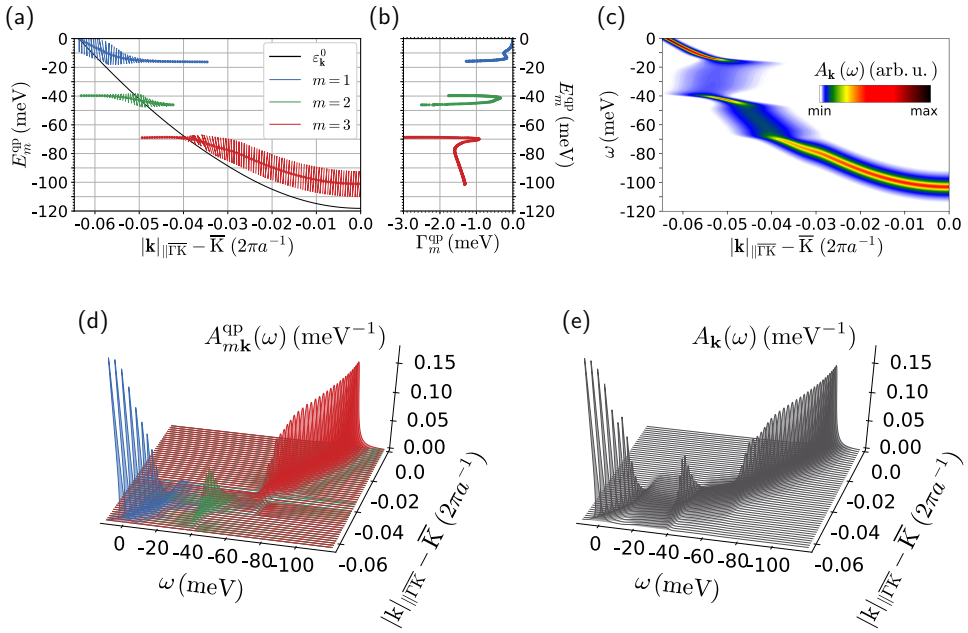

Figure 3.13. Complex quasiparticle band structure of doped monolayer MoS_2. (a) Dispersion of the three quasi-particle poles found for the outer spin-split band. The real part of the poles, that is the quasiparticle energies E_m^{qp}, for different values of the modulus of the momentum $\mathbf{k}$ are shown by the blue ($m = 1$), green ($m = 2$), and red ($m = 3$) dots, respectively. The bare electron energy $\varepsilon^0_{\mathbf{k}}$ is represented by the dashed black line. The length of the bars represent the spectral weight of each pole, given by the real part of their residues, $\mathrm{Re}\,(\mathbb{Z}_m^{\mathrm{qp}})$, while the imaginary part of the residues are represented by the rotation of the bars, $\mathrm{Im}\,(\mathbb{Z}_m^{\mathrm{qp}}) = 1$ giving a rotation of $\theta = \pi$ radians. (b) Negative of the imaginary part of the quasiparticle poles, that is, the inverse quasiparticle lifetime Γ_m^{qp}, with respect to the quasiparticle energies. The color code is the same as in (a). (c) Spectral function of the outer spin-split band on the area highlighted in Fig. 3.9. (d) Contribution to the spectral function coming from each complex quasiparticle pole (see Eq. (3.26)), shown by different colors following the same convention as in (a). (e) Three dimensional representation of (c).

MoS_2, in the region of the Brillouin zone highlighted in Fig. (3.9), where the same notation as in Fig. 3.4 has been used. For ease of comparison, the separated contribution to the spectral function for this band is shown in Fig. 3.13(c). By comparing Figs. 3.13(a) and (c), it is clearly appreciated that the most important spectral features can be indeed identified as elementary quasiparticle excitations. Qualitatively, the behavior of these quasiparticles is similar to the one described in the simple Einstein model of Sec. 3.2.1. However, the peculiar structure of the self-energy in this system results in up to three different solutions for some regions of the Brillouin zone.

Close to the Fermi momentum k_F, an Engelsberg–Schrieffer-like [5] state appears with a strongly renormalized dispersion and a very long lifetime,

which we denote as the $m = 1$ solution and we represent in blue color. Far enough from k_F, we find a dispersive and damped state, denoted as the $m = 3$ solution and represented in red color. Remarkably, for some intermediate values of the momentum we find an additional solution with an important spectral weight whose dispersion is practically flat, which we denote as the $m = 2$ solution and represent in green color. Its renormalized flat dispersion indicates that it is a strongly interacting state which tends to localization. Moreover, this state appears long lived as it lies just in the energy window where the imaginary part of the self-energy has almost a gap (see Fig. 3.10(a)). More specifically, the electron–phonon limited lifetime broadening at this energy range is almost negligible, $\Gamma^{\rm qp}_{m=2} \sim 0.35\,\text{meV}$, as shown in Fig. 3.13(b).

An assessment on the validity of the quasiparticle picture can be obtained by comparing the full spectral function with the so-called quasiparticle spectral function, which directly follows from Eq. (3.9),

$$A^{\rm qp}_{\mathbf{k}}(\omega) = -\frac{1}{\pi}\sum_m \text{Im}\frac{\mathbb{Z}^{\rm qp}_m}{z - \widetilde{E}^{\rm qp}_m}\ . \tag{3.26}$$

We represent the separate contributions from each quasiparticle pole in Fig. 3.13(d), following the same color convention as in Figs. 3.13(a),(b). This figure shows how the spectral weight is transferred from one quasi-particle into others as a function of momentum $\mathbf{k}$. For ease of comparison, the full spectral function, as directly obtained from Eq. (1.36), is represented again in Fig. 3.13(e), from the same perspective and in the same frequency range as in Fig. 3.13(d).

The comparison between the quasiparticle and the full spectral function is strikingly good, indicating that the the threefold band structure observed in experiment certainly corresponds to quasiparticle excitations and not to incoherent multi-phonon contributions.

3.4 Outlook: Connection with the polaron problem

In the previous sections we have analyzed in detail the renormalization of the electron energy-momentum dispersion as a consequence of the electron-phonon interaction. From these results it is appreciated that the electron-phonon interaction tends to flatten the electron bands in some regions of the Brillouin zone, which corresponds to a reduction of the electron velocity and an increase of the effective mass. The most clear manifestation of this effect has emerged in the strongly renormalized intermediate quasiparticle state of doped MoS_2 (see $m = 2$ in Fig. 3.13).

Physically, this increase of the effective mass can be understood to originate from an effective dressing of the electron states by a virtual phonon

cloud, which results from the atoms moving from their equilibrium positions to screen the charge of the propagating electron. The most drastically simplified version of this phenomenon can be realized in the case of a single electron added to the conduction band of an ionic insulator. When the excess electron deforms the crystal lattice so as to create a potential well from which it cannot escape, it is said to become self-trapped, and the composite quasiparticle formed by the electron and the polarization cloud is referred to as a *polaron*[2] [99–101].

The advent of first principles DFT methods has opened new possibilities to obtain accurate microscopic insight into material-specific polaron properties [102–105]. In this approach to the problem, the regular practice is to perform a supercell calculation with an extra electron added to the system, and relax the structure adiabatically to see whether a localized and distorted configuration is energetically more favorable than the conventional periodic state. Very recently, this procedure has been formalized in Refs. [106, 107], tracing back the localization condition within DFT to the solution of a set of two coupled equations, one for the electronic wave function and one for the atomic displacements (see Eqs.(24)–(25) of Ref. [107]). In any case, this type of calculations gives the localized structure of the polaron state directly in real space.

In the opposite side, the most recent claims on the experimental detection of polaron states have come through their signatures in the ARPES spectra, that is, in momentum space [87, 108–111]. As we have seen in the previous sections for the case of MoS_2 [87], in order to describe this signatures from first principles calculations, one needs to go beyond DFT and apply more advanced many-body Green's function methods [14]. Similar techniques give satisfactory results in the case of the replica bands seen on slightly doped semiconductors [13, 112].

In this context, one question that naturally comes up is whether one could obtain the real space structure of localized polarons from the general Green's function formalism reviewed in Chapter 1. In principle, this approach could provide a non-adiabatic description of the polaron formation, from where the expressions derived in Ref. [107] should be retrieved after applying the pertinent approximations. Most importantly, it would clarify the hitherto ambiguous connections between the polaron localization in real space and its ARPES signatures in momentum space, since this technique is sensible to extended states. In this section, we briefly outline the preliminar steps we have made towards the development of such approach, which is still a work in progress.

[2]Sometimes in the literature the word polaron is used to name interacting electron-phonon quasiparticles in general. In this thesis, we limit the use of this term to describe self-trapped quasiparticles.

3.4.1 Quasiparticle equation in real space

The formal definition of quasiparticles within the Green's function formalism, as described in Sec. 3.1, allows for the determination of their real space structure through the solution of Eq. (3.7) directly in real space [93],

$$H^0(\mathbf{r})\,\psi^{\mathrm{qp}}(\mathbf{r}) + \int d\mathbf{r}'\,\tilde{\Sigma}(\mathbf{r},\mathbf{r}',\widetilde{E}^{\mathrm{qp}})\,\psi^{\mathrm{qp}}(\mathbf{r}') = \widetilde{E}^{\mathrm{qp}}\,\psi^{\mathrm{qp}}(\mathbf{r})\ . \tag{3.27}$$

Moreover, the Hedin-Baym equations reviewed in Chapter 1, and in particular the contributions to the self-energy discussed in Sec. 1.3, incorporate the electron-phonon interactions that may happen in any metal or semiconductor in a general way. Thus, provided that H^0 describes the effects of electron-electron interactions — even approximately, for example through DFT —, inserting Eqs. (1.26)–(1.28) in Eq. (3.27) should allow for the description of the localization of polaron quasiparticles in real space.

However, a crucial assumption adopted in Sec. 1.4.4, namely the assumption of crystal periodicity of the electron self-energy, excludes this possibility. This assumption permits to label the quasiparticles with a momentum index $\mathbf{k}$, and thus to obtain a well-defined quasiparticle band structure, as amply discussed in the first part of this chapter. By extension, a crystal periodic self-energy in Eq. (3.27) can describe the renormalization of a $\mathbf{k}$-dependent periodic quasiparticle wave function within the unit cell, but can never give rise to a localized polaronic state which, by definition, breaks the original periodicity of the lattice.

In order to generalize our formalism, we have to go back to the full Hedin-Baym equations of Chapter 1, and see what is the minimal extra term we should consider in order to obtain non-periodic contributions to the self-energy.

3.4.2 Finite atomic displacement term on the electron self-energy

All the electron-phonon physics described within the Hedin-Baym formalism have their origin in the harmonic expansion of the nuclear density operator given by Eq. (1.9). As discussed in Sec. 1.3, if one only keeps the zero-order term in the expansion, so that $\langle \hat{n}_{\mathrm{n}}(\mathbf{r})\rangle \approx n^0_{\mathrm{n}}(\mathbf{r})$, one would be describing a solid with classical nuclei fixed at their equilibrium positions. However, the quantum nature of the vibrating nuclei allows for a finite value of the mean square of the displacement operator, which gives a contribution to the expectation value of the nuclear density through the second-order term in Eq. (1.9). This translates to a finite displacement-displacement correlation function $D_{\kappa p\alpha,\kappa' p'\alpha'}$, which in turn gives rise to a finite Fan-Migdal self-energy Σ^{FM} through the phonon contribution to the screened Coulomb interaction W_{ph} [see Eqs. (1.15), (1.20) and (1.27)].

Curiously, the average of the displacement operator $\langle \Delta\hat{\tau}_{\kappa\alpha p}\rangle$, coming from the first-order term in the expansion of Eq. (1.9), has always been taken to be zero in the literature to the best of our knowledge. This term has been neglected based on the fact that in a periodic crystal, the atoms are allowed to vibrate around their equilibrium positions, but, on average, they have to remain at their initial periodic positions. Interestingly enough, this reasoning breaks down in a polaronic ground state, where the equilibrium atomic positions are indeed displaced, translating into a finite contribution of this term which should be included in the self-energy.

The most evident contribution of a finite atomic displacement term arises in the Debye-Waller self-energy of Eq. (1.28). This can be seen by expanding the total-density operator to second order in the atomic displacements, assuming that the electronic field operators and the nuclear-displacement operators are uncorrelated, that is $\langle \hat{n}^{\mathrm{rn}}\Delta\hat{\tau}_{\kappa\alpha p}\rangle \approx \langle \hat{n}^{\mathrm{rn}}\rangle\langle\Delta\hat{\tau}_{\kappa\alpha p}\rangle$ [113], where $\hat{n}^{\mathrm{rn}} = \hat{n}_{\mathrm{e}} + n^0_{\mathrm{n}}$, and using the definition $V_{\mathrm{tot}}(1) = \int d2\, v(12)\,\langle \hat{n}(2)\rangle$. In this way, one can write the Debye-Waller self-energy as

$$\Sigma^{\mathrm{DW}}(12) = \delta(12)\sum_{\kappa\alpha p}\frac{\partial V^{\mathrm{rn}}_{\mathrm{tot}}(1)}{\partial \tau^0_{\kappa\alpha p}}\langle\Delta\hat{\tau}_{\kappa\alpha p}\rangle \tag{3.28a}$$

$$+\, i\delta(12)\sum_{\substack{\kappa\alpha p\\ \kappa'\alpha' p'}}\frac{1}{2}\frac{\partial^2 V^{\mathrm{rn}}_{\mathrm{tot}}(1)}{\partial\tau^0_{\kappa\alpha p}\partial\tau^0_{\kappa'\alpha' p'}} D_{\kappa\alpha p,\kappa'\alpha' p'}(t_1^+, t_1)\ . \tag{3.28b}$$

The second term, Eq. (3.28b), is the usual Debye-Waller term discussed in the literature (see, for example Eq. (159) of Ref. [7] and discussion/references therein).

Most importantly, the first term Eq. (3.28a), which to the best of our knowledge has not been discussed so far, will give a contribution to the renormalization of the electron quasiparticles — via Eq. (3.27) — whenever there are finite displacements of the equilibrium atomic positions in the ground state, as it happens in a polaronic state. Moreover, assuming that the total potential at rigid nuclei $V^{\mathrm{rn}}_{\mathrm{tot}}$ can be approximated as the KS potential of DFT, one recovers Eq. (24) of Ref. [107] by only considering this contribution in the self-energy of Eq. (3.27).

It is noteworthy that this term is static, and that therefore it cannot give rise to spectral features such as kinks or satellites. This leads to the important conclusion that although both have their origin in the electron-phonon interaction, the polaron localization in real space is not directly related to the momentum-space features observed in ARPES experiments.

3.4.3 Determination of the atomic displacements

The new term arising in the Debye-Waller self-energy, as discussed in the previous section, accounts for the renormalization of the polaron wave function due to the possible finite displacements of the atomic positions from

their equilibrium periodic positions. However, we have not specified what the magnitude of these displacements would be — if any —, and how we can determine them.

In order to do so, we move from Green's functions and work directly with the displacement operator. We consider a somewhat simplified picture with respect to Eq. (1.1), and start from a Hamiltonian which describes well-defined electrons and phonons, and the coupling between them to linear order in the displacement [2, 7, 27]

$$\begin{aligned}\hat{H} &= \hat{H}_{\mathrm{e}} + \hat{H}_{\mathrm{p}} + \hat{H}_{\mathrm{ep}} \\ &= \sum_{n\mathbf{k}} \varepsilon_{n\mathbf{k}} \hat{c}^{\dagger}_{n\mathbf{k}} \hat{c}_{n\mathbf{k}} + \sum_{\mathbf{q}\nu} \omega_{\mathbf{q}\nu} (\hat{a}^{\dagger}_{\mathbf{q}\nu} \hat{a}_{\mathbf{q}\nu} + 1/2) \\ &\quad + N_p^{-\frac{1}{2}} \sum_{\substack{\mathbf{k},\mathbf{q} \\ mn\nu}} g_{mn\nu}(\mathbf{k},\mathbf{q})\, \hat{c}^{\dagger}_{m\mathbf{k}+\mathbf{q}} \hat{c}_{n\mathbf{k}} (\hat{a}_{\mathbf{q}\nu} + \hat{a}^{\dagger}_{-\mathbf{q}\nu}) \ . \end{aligned} \tag{3.29}$$

The phonon part of the Hamiltonian can be rewritten in terms of the displacement operator and its momentum conjugate operator [7, 27],

$$\hat{H}_{\mathrm{p}} = -\sum_{\kappa\alpha p} \frac{\hat{p}^2_{\kappa\alpha p}}{2M_\kappa} + \frac{1}{2} \sum_{\substack{\kappa\alpha p \\ \kappa'\alpha' p'}} C_{\kappa\alpha p,\kappa'\alpha' p'} \Delta\hat{\tau}_{\kappa\alpha p} \Delta\hat{\tau}_{\kappa'\alpha' p'} \ , \tag{3.30}$$

where $C_{\kappa\alpha p,\kappa'\alpha' p'}$ are the interatomic force constans. Besides, the electron-phonon Hamiltonian can be rewritten in terms of the displacement operator [7],

$$\hat{H}_{\mathrm{ep}} = \sum_{n\mathbf{k},m\mathbf{k}'} \langle \varphi_{m\mathbf{k}'} | \sum_{\kappa\alpha p} \frac{\partial V^{\mathrm{rn}}_{\mathrm{tot}}}{\partial \tau_{\kappa\alpha p}} \Delta\hat{\tau}_{\kappa\alpha p} \, | \varphi_{n\mathbf{k}} \rangle \, \hat{c}^{\dagger}_{m\mathbf{k}'} \hat{c}_{n\mathbf{k}}, \tag{3.31}$$

where $|\varphi_{n\mathbf{k}}\rangle$ are electronic single-particle basis wave functions. We can rewrite Eq. (3.31) by means of the field-operators in real-space,

$$\hat{\Psi}(\mathbf{r}) = \sum_{n\mathbf{k}} \langle \mathbf{r} | \varphi_{n\mathbf{k}} \rangle \, \hat{c}_{n\mathbf{k}}, \tag{3.32}$$

$$\hat{\Psi}^{\dagger}(\mathbf{r}) = \sum_{n\mathbf{k}} \langle \varphi_{n\mathbf{k}} | \mathbf{r} \rangle \, \hat{c}^{\dagger}_{n\mathbf{k}}, \tag{3.33}$$

and insert $\int d\mathbf{r} |\mathbf{r}\rangle\langle\mathbf{r}| = 1$, so that Eq. (3.31) becomes

$$\hat{H}_{\mathrm{ep}} = \int\int d\mathbf{r} d\mathbf{r}' \hat{\Psi}^{\dagger}(\mathbf{r}) \sum_{\kappa\alpha p} \langle \mathbf{r} | \frac{\partial V^{\mathrm{cn}}_{\mathrm{tot}}}{\partial \tau_{\kappa\alpha p}} | \mathbf{r}' \rangle \hat{\Psi}(\mathbf{r}') \Delta\hat{\tau}_{\kappa\alpha p} \ . \tag{3.34}$$

Finally, since the total potential is local $\left(\langle \mathbf{r} | \frac{\partial V^{\mathrm{cn}}}{\partial \tau_{\kappa\alpha p}} | \mathbf{r}' \rangle = \frac{\partial V^{\mathrm{cn}}(\mathbf{r})}{\partial \tau_{\kappa\alpha p}} \delta(\mathbf{r} - \mathbf{r}') \right)$, and using the definition of the electron density operator of Eq. (1.7), we find

$$\hat{H}_{\mathrm{ep}} = \int d\mathbf{r} \sum_{\kappa\alpha p} \frac{\partial V^{\mathrm{cn}}_{\mathrm{tot}}(\mathbf{r})}{\partial \tau_{\kappa\alpha p}} \, \hat{n}_{\mathrm{e}}(\mathbf{r}) \, \Delta\hat{\tau}_{\kappa\alpha p} \ . \tag{3.35}$$

Now, using the canonical commutation relations,

$$[\hat{\tau}_{\kappa\alpha p}, \hat{\tau}_{\kappa'\alpha'p'}] = [\hat{p}_{\kappa\alpha p}, \hat{p}_{\kappa'\alpha'p'}] = 0 \ , \tag{3.36}$$

$$[\hat{\tau}_{\kappa\alpha p}, \hat{p}_{\kappa'\alpha'p'}] = i\,\delta_{\kappa\kappa'}\delta_{\alpha\alpha'}\delta_{pp'} \ , \tag{3.37}$$

we can derive the equation of motion for the displacement operator, which reads

$$\begin{aligned}\frac{d^2}{dt^2}\Delta\hat{\tau}_{\kappa\alpha p}(t) &= -[[\Delta\hat{\tau}_{\kappa\alpha p}, \hat{H}], \hat{H}] = -[\frac{i}{M_\kappa}\hat{p}_{\kappa p}, \hat{H}] \\ &= -\sum_{\kappa'\alpha'p'} \frac{C_{\kappa\alpha p,\kappa'\alpha'p'}}{M_\kappa}\Delta\hat{\tau}_{\kappa'\alpha'p'}(t) + \frac{1}{M_\kappa}\int d\mathbf{r}\frac{\partial V^{\rm cn}_{\rm tot}(\mathbf{r})}{\partial\tau_{\kappa\alpha p}}\,\hat{n}_{\rm e}(\mathbf{r}) \ .\end{aligned} \tag{3.38}$$

This equation is a nonhomogeneous differential equation for the time-dependence of the displacement operator. The general solution of the complementary homogeneous equation — i.e. second term on the right hand side equals zero — is simply given by a linear combination of the time-dependence of the phonon eigenmodes [27]. However, the additional second term coming from $\hat{H}_{\rm ep}$ introduces a particular time-independent solution, so that finally we find

$$\begin{aligned}\Delta\tau_{\kappa\alpha p}(t) = &\sum\nolimits_{\mathbf{q}\nu}\sqrt{\frac{1}{2N_pM_\kappa\omega_{\mathbf{q}\nu}}}\,e^{i\mathbf{q}\cdot\mathbf{R}_p}e_{\kappa\alpha,\nu}(\mathbf{q})\,(\hat{a}_{\mathbf{q}\nu} + \hat{a}^\dagger_{-\mathbf{q}\nu})\,e^{i\omega_{\mathbf{q}\nu}t} \\ &+ \sum_{\kappa'\alpha'p'} C^{-1}_{\kappa\alpha p,\kappa'\alpha'p'}\int d\mathbf{r}\frac{\partial V^{\rm cn}_{\rm tot}(\mathbf{r})}{\partial\tau_{\kappa'\alpha'p'}}\,\hat{n}_{\rm e}(\mathbf{r}) \ .\end{aligned} \tag{3.39}$$

In order to determine the value of the atomic displacements, we have to take the average of the displacement operator over the many-body ground state, $\langle\Delta\hat{\tau}_{\kappa\alpha p}\rangle$. The phonon creation and annihilation operators in the first term make the average over this term to vanish. This means that in the absence of the electron-phonon coupling part of the Hamiltonian, the atoms vibrate without displacing on average from their equilibrium periodic positions, as expected. However, the average over the second term gives a finite constant contribution which depends on the average of the electron density:

$$\langle\Delta\hat{\tau}_{\kappa\alpha p}\rangle = \sum_{\kappa'\alpha'p'} C^{-1}_{\kappa\alpha p,\kappa'\alpha'p'}\int d\mathbf{r}\frac{\partial V^{\rm cn}_{\rm tot}(\mathbf{r})}{\partial\tau_{\kappa'\alpha'p'}}\,\langle\hat{n}_{\rm e}(\mathbf{r})\rangle \ . \tag{3.40}$$

This expression implies that finite atomic displacements with respect to the equilibrium positions are possible as a result of the electron-phonon interaction and a non-periodic electronic density. In this scenario, where the initial periodic symmetry has been broken, the displacements and the density have to be determined self-consistently.

In order to link this expression to the polaron problem, the difference between a ground state of N electrons — in which the displacement vanishes —

and a ground state of $N+1$ electrons has to be taken. Then one can assume that the total potential and the force constants do not change due to the presence of the extra electron, and one obtains an equivalent expression to Eq.(25) of Ref. [107], where the electron density entering the integral is the one of the extra localized polaron.

3.4.4 Self-consistent polaron equations

All in all, Eqs. (3.27)–(3.28a), the density obtained from the polaron quasiparticle wave functions, and Eq. (3.40), form a set of self-consistent equations equivalent to the ones derived within DFT in Ref. [107]. However, in our case they have been derived within a more general many-body formalism. This makes the upgrading of the theory to incorporate non-adiabatic effects in the polaron formation readily available through the addition of the dynamical Fan-Migdal term in the self-energy of Eq. (3.27), which has not been considered in the literature so far.

Although more work is needed to formalize this procedure and make it amenable for practical calculations, the preliminary results presented in this section open the path towards a complete first principles many-body description of polaron quasiparticles.

3.5 Conclusion

In this chapter, we have analyzed in deep detail the renormalization of electron quasiparticles driven by the electron-phonon interaction.

In the first part of the chapter, we have shown that a proper definition of quasiparticles within a Green's function formalism requires the analytic continuation of the electron self-energy to the lower-half of the complex energy plane. Based on previous work, we have extended the available numerical methods to obtain the analytic continuation of general self-energies beyond the constant density of states approximation. Then, we have described the application of the implemented procedure to unambigously identify, from first principles, an intricate strongly interacting electron-phonon quasiparticle band structure underlying the recently reported ARPES measurements on the doped monolayer MoS_2.

Finally, in the last part of the chapter, we have outlined a procedure which lays the ground for a full many-body description of polaron quasiparticles in real space from first principles.

Chapter 4

Symmetric Helmholtz Fermi Surface Harmonics for electron-phonon problems

The Fermi surface (FS) is an abstract surface in reciprocal space that separates the occupied from the unoccupied electronic states of a metal. As dictated by the Pauli exclusion principle, the low-energy electronic excitations driven by, say, small external electromagnetic fields or finite temperatures, are thus restricted to a very narrow window around the FS. This implies that a detailed knowledge of the specific shape and topology of the FS, as well as of the matrix elements defining the scattering processes on it, appears crucial for a proper understanding of most transport properties of metals [114].

In this respect, one of the most important scattering source for electrons close to the Fermi surface is their interaction with phonons [2]. As we have analyzed in detail in Chapter 3, the electron-phonon interaction yields a strong renormalization of the electronic quasiparticles, modifying their effective mass and their lifetime. This, in turn, underpins observable macroscopic phenomena such as the temperature dependent resistivity [1], or even conventional superconductivity [21, 22], which we will adress in this chapter.

The delimitation of the relevant many-body processes to the Fermi surface, although implying a simplification *a priori*, results in a complication from the numerical point of view. In a typical electronic structure calculation, the Brillouin zone in reciprocal space is sampled by a discrete number of **k**-points, for which the single-particle electronic energies are computed through Density Functional Theory methods (see Sec. 1.4.3). The most common procedure to determine a FS is then to select the **k**-points for which the electronic energies lie within a given threshold around the Fermi energy (E_F), generally approximated by a smearing function such as a Gaussian. The smearing

function should be as narrow as possible, ideally becoming a delta function, and the finer the details needed on the description of the Fermi surface, the more the **k**-points required in the sampling.

Several works have shown that a huge amount of **k**-points points are actually needed for accurate calculations of the diverse problems involving electron-phonon interactions [9–11, 115]. As a rough estimate, typically one needs around $n_{\mathbf{k}} \sim 10^4$ points for a faithful description of the Fermi surface anisotropy, resulting in $n_{\mathbf{k},\mathbf{k}'} \sim 10^8$ pairs of points in which the electron-phonon matrix elements $g^{\nu}_{m\mathbf{k},m'\mathbf{k}'}$ have to be computed for all the different FS sheets ($n_m \sim 1$–10) and phonon branches ($n_\nu \sim 1$–10). In total, the required amount of data is of the order of $N \sim 10^9$ elements. For electron-phonon problems in which self-consistent integral equations have to be solved on the FS, such as the problem of superconductivity that we will discuss in this chapter, the computational workload gets exceedingly high.

With the aim of alleviating this issue, a promising scheme was proposed by Allen in Ref. [116]. His approach was based on a transformation of the scalar quantities defined on the FS into a new basis set composed of polynomials of electron velocities orthogonalized on the FS, which were called Fermi Surface Harmonics (FSH). However, the technical difficulties encountered in the construction of the basis set, which involves several semi-analytic steps and requires a different procedure for each crystal structure, has turned the practical application of the method unattainable so far, except for some recent scarce instances [117, 118].

An alternative definition of the FSH basis set was introduced in Ref. [119], which overcome the limitations of Allen's proposal. In this novel approach, the orthonormal basis functions, called Helmholtz Fermi Surface Harmonics (HFSH), are obtained by a purely numerical procedure as the solutions of the Helmholtz equation defined on a triangularly tessellated Fermi surface.

In this chapter, we will introduce some crucial improvements on the procedure presented in Ref. [119], which will allow to incorporate the crystal symmetries in the HFSH basis set. This will permit an optimal representation of physical quantities defined on the Fermi surface in terms of few symmetric elements of the set.

In the second part of the chapter, the full potential of the method will be demonstrated in practice for the first time: we will show that the anisotropic gaps and transition temperatures of phonon-mediated superconductors can be determined to high accuracy and a much reduced computational cost from first principles through the solution of the Eliashberg equations of superconductivity in the HFSH representation.

4.1 General properties of the HFSH basis set

For completeness, we first review the main properties of the HFSH basis set introduced in Ref. [119].

The HFSHs are defined as the eigenmodes of a velocity-weighted Laplace-Beltrami operator on the curved Fermi surface,

$$v(\mathbf{k})\,\nabla^2_{\mathbf{k}}\Phi_L(\mathbf{k}) \,+\, \omega_L\,\Phi_L(\mathbf{k}) = 0, \tag{4.1}$$

where ω_L are the eigenvalues associated with the eigenfunctions $\Phi_L(\mathbf{k})$. Eq. (4.1) represents a generalized Helmholtz equation, from which, for example, the ordinary spherical harmonics are recovered in a spherical Fermi surface with a constant $v(\mathbf{k})$.

The HFSH functions obtained through Eq. (4.1) obey the orthogonality condition

$$\int \frac{d^2 s_{\mathbf{k}}}{v(\mathbf{k})}\,\Phi_{L'}(\mathbf{k})\,\Phi_L(\mathbf{k}) = \delta_{L',L}\int \frac{d^2 s_{\mathbf{k}}}{v(\mathbf{k})}\ , \tag{4.2}$$

and form a complete basis. Thus, we can represent any anisotropic function $F(\mathbf{k})$ defined on the Fermi surface by an expansion in the HFSH basis set,

$$F(\mathbf{k}) = \sum_L F_L\,\Phi_L(\mathbf{k})\ , \tag{4.3}$$

where the expansion coefficients are given by the following FS integrals:

$$F_L \equiv \frac{\int_{S_F}\frac{d^2 s_{\mathbf{k}}}{v(\mathbf{k})}\,\Phi_L(\mathbf{k})\,F(\mathbf{k})}{\int_{S_F}\frac{d^2 s_{\mathbf{k}}}{v(\mathbf{k})}}\ . \tag{4.4}$$

Besides, the product of two functions $F_1(\mathbf{k})$ and $F_2(\mathbf{k})$ may be conveniently represented in terms of the separated HFSH coefficients for each function F_{L_i} by

$$F_1(\mathbf{k})F_2(\mathbf{k}) = \sum_{L_1 L_2 L}\Xi_{L,L_1L_2}\,F_{L_1}\,F_{L_2}\,\Phi_L(\mathbf{k})\ , \tag{4.5}$$

where Ξ_{L,L_1L_2} are the generalization of the Clebsch-Gordan coefficients for the HFSH basis set:

$$\Xi_{L,L_1L_2} = \frac{\int_{S_F}\frac{d^2 s_{\mathbf{k}}}{v(\mathbf{k})}\,\Phi_L(\mathbf{k})\,\Phi_{L_1}(\mathbf{k})\,\Phi_{L_2}(\mathbf{k})}{\int_{S_F}\frac{d^2 s_{\mathbf{k}}}{v(\mathbf{k})}}\ . \tag{4.6}$$

An effective numerical procedure to obtain the HFSH basis set involves the construction of a triangular mesh defining the Fermi surface as a prior step. This allows for the numerical solution of a discretized version of Eq. 4.1, which is transformed into a generalized sparse eigenvalue problem,

$$\frac{v(\mathbf{k}_i)}{S_i}\sum_j \Omega_{i,j}\,\Phi_L(\mathbf{k}_j) = \omega_L\,\Phi_L(\mathbf{k}_i)\ . \tag{4.7}$$

In this expression, i and j are indices for vertices on the triangulated mesh, $\mathbf{k}_i$ represents the coordinates of a vertex i in the reciprocal space, and S_i its control area, defined as the sum of $\frac{1}{3}$ of its neighboring triangle areas. The discretized Laplace-Beltrami operator $\Omega_{i,j}$ takes the form

$$\Omega_{i,j} = \begin{cases} -\frac{1}{2}\left[\cot(\alpha_{i,j}) + \cot(\beta_{i,j})\right] & i \neq j \\ \sum_{i \neq j} \Omega_{i,j} & i = j \end{cases} , \tag{4.8}$$

where $\alpha_{i,j}$ and $\beta_{i,j}$ are the two opposite angles of the triangles sharing the edge joining the vertices i and j.

The relations given by Eqs. (4.3)–(4.6) remain equally valid in the discretized mesh, given that the FS integrals can be approximated by

$$\int_{S_F} \frac{d^2 s_{\mathbf{k}}}{v(\mathbf{k})} \approx \sum_i \frac{S_i}{v(\mathbf{k}_i)} . \tag{4.9}$$

This expression shows that, in addition to providing a numerical scheme in which the HFSH basis functions can be obtained in practice, a high-quality triangulated FS — as obtained for example through the procedure described in the next section — allows for more efficient and accurate Fermi surface integrals in comparison with the conventional smearing techniques.

4.2 Fully symmetric triangulated Fermi surface

In this section, we describe the numerical procedure we have implemented to obtain a triangular tessellation of the Fermi surface of any metal which fulfills all the point group and translational symmetries of its crystal structure.

In principle, a robust method for accomplishing such a task is the linear tetrahedron method [120]. In its original formulation, a tetrahedral tessellation of the BZ is performed in the crystal coordinates, where a $\mathbf{k}$-point grid translates into cubes which can be trivially decomposed in six tetrahedra. A triangulated Fermi surface can be then obtained from the linear interpolation of the electronic energies at the corners of each tetrahedra (see Sec. 4.2.3 below). This approach was used in the original procedure to obtain the HFSH functions presented in Ref. [119]. However, when analyzing in detail the resulting triangulated isosurface, one finds that the symmetries of the crystal are not incorporated in the FS. In other words, the triangulated FS obtained is not invariant under all the symmetry operations of the crystal — as it should —, due to the broken symmetries introduced by the initial tetrahedral tessellation of the BZ.

In this thesis, we have developed an alternative approach, which allows us to find an irreducible isosurface in a previously detected irreducible BZ in cartesian coordinates. As we will see in the next sections, this variation provides an effective way of obtaining a fully symmetric triangulated Fermi

surface, but also poses some technical difficulties, which are nevertheless overcome by our procedure.

We describe our approach following several steps. First, the irreducible volume of the BZ (IBZ) is identified. Then a tetrahedral tessellation of the IBZ is generated, from which a triangulated irreducible Fermi surface (IFS) is obtained using the linear tetrahedron method. As an optional intermediate step, different mesh improvement techniques are proposed and implemented in order to increase the quality of the triangular mesh. Finally, the IFS is rotated using all the symmetries of the crystal, resulting in a high-quality and fully symmetric triangulated Fermi surface.

4.2.1 Detection of the irreducible wedge of the Brillouin zone

In any crystal system, an irreducible wedge of the Brillouin zone exists from which the full BZ can be recovered by applying all the symmetry operations that the crystal possesses. The first task in our procedure will be to identify such an irreducible volume of the Brillouin zone, for any system crystallizing in a given space group.

Geometrically speaking, the BZ is a polyhedron composed of polygonal faces joined by edges. We first make the observation that, apart from the Γ point that lies in the center of the BZ, the high symmetry points of the 14 types of Bravais lattices always lie either in the center of a face, or in the corner or the middle-point of an edge [121]. As an illustrative example, we show in Fig. 4.1(a) the BZ of the FCC lattice (space group $Fm\bar{3}m$), in which all the corners, the centers of the faces and the middle-points of the edges have been highlighted with blue dots.

Joining each of the points in the edges with the points at their nearest corners, and these two in turn with the points at the center of their corresponding face, we can create a triangular tessellation of the polygonal faces of the BZ. Moreover, joining all of these points with the Γ point in the center of the BZ, we can obtain a coarse tetrahedral tessellation of the whole BZ volume. Given that, by definition, all the non-equivalent high symmetry points have to be included in the irreducible wedge of the BZ, we can represent the IBZ as the sum of several of these tetrahedra. We show in Fig. 4.1(a) the coarse tetrahedral tessellation of the FCC BZ volume obtained in this way, in which some tetrahedra have been removed for ease of visualization.

In order to determine which are the irreducible tetrahedra that we have to include in order to form the IBZ of a given system, we need to know the particular symmetry operations belonging to its space group. The procedure is similar to the one used to detect the irreducible number of $\mathbf{k}$-points within a regular grid that can form a full mesh in the BZ by applying all the symmetry operations of a particular system. In a first step, one selects an arbitrary tetrahedron and applies all the symmetry operations allowed by

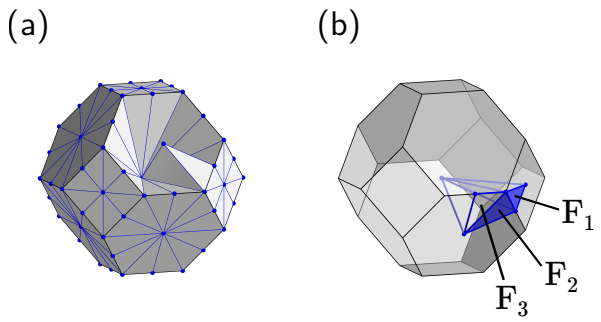

Figure 4.1. Detection of the irreducible wedge of the Brillouin zone. (a) Initial tetrahedral tessellation of the full BZ, from wich the irreducible BZ volume can be detected, shown in (b). Irreducible faces at the IBZ boundary are highlighted in blue.

the point group. In this way, we detect the volume of the BZ connected by symmetry to the initially selected tetrahedron. We repeat this operation for all the tetrahedra in the initial tessellation of the BZ volume, constructing in this way the irreducible volume of the BZ. As an example, the resulting IBZ volume for the FCC lattice, which is composed by three tetrahedra, is shown in Fig. 4.1(b).

In addition, we have that as a consequence of the translational invariance of crystals, at the BZ boundary the Fermi surface possesses extra symmetries beyond the point group. In this respect, we have to check for further reduction of the irreducible wedge at the BZ boundary. For this purpose, we repeat a similar procedure as the one described above, but only for the triangular facets on the boundary of the IBZ volume. We now apply $\mathcal{S} + \mathbf{G}$ operations, where $\mathcal{S}$ is a symmetry rotation and $\mathbf{G}$ is a reciprocal lattice vector, and check if any of the facets can be recovered from an irreducible subgroup. Following with the FCC example, we find that one of the three triangular facets (F_3) can be recovered in this way from its neighbor facet (F_2). The irreducible facets of the IBZ (F_1 and F_2) are highlighted in blue in Fig. 4.1(b).

4.2.2 Tetrahedral tessellation of the irreducible wedge of the Brillouin zone

The next step in our procedure will be to obtain a fine tetrahedral tessellation of the irreducible wedge of the Brillouin zone identified in Sec. 4.2.1. Obtaining a tetrahedral tessellation of a general polyhedron defining the IBZ in Cartesian coordinates is a nontrivial problem, and the additional $\mathcal{S} + \mathbf{G}$ symmetries at the BZ boundaries force us to proceed with care. We describe the scheme we have implemented for this purpose in the following.

The first task will be to triangulate the faces of the IBZ volume in such a way that all the $\mathcal{S} + \mathbf{G}$ symmetries are fulfilled. To this end, in a first step we triangulate the irreducible facets that are related to the non-irreducible

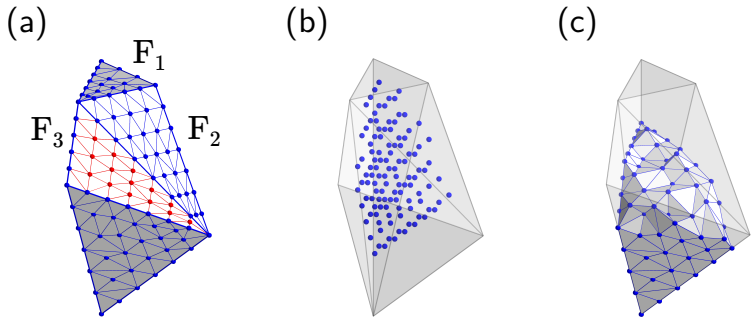

Figure 4.2. Tetrahedral tessellation of the irreducible wedge of the Brillouin zone. (a) The IBZ boundary faces are first triangulated, (b) extra Steiner points are added within the IBZ volume, and (c) a Delaunay tetrahedralization is performed constrained by the triangular facets at the boundary.

ones by symmetry (F_2 in Fig. 4.2(a)). In a second step, we obtain the triangulation of the non-irreducible facets by applying the corresponding symmetry operations (F_3 in Fig. 4.2(a)). In a third step, we triangulate all the rest of the irreducible facets, considering the constraints imposed by the nodes already present in the facet-joining edges.

For the triangulation of each facet, we first distribute nodes throughout the facet-plane. This distribution is done in such a way that the projection of a given mesh of points in the reciprocal-lattice vectors $\{n_{k_1}, n_{k_2}, n_{k_3}\}$ onto the facet-plane is approximately matched, setting the condition that the nodes on each edge are regularly spaced. Then a constrained Delaunay triangulation is constructed from this nodes using the TRIANGLE code [122], in which the edges of the facet are maintained. As an example, the triangulation obtained in such a way for the boundary of the FCC IBZ volume is shown in Fig.4.2(a), where the facet obtained by symmetry is highlighted in red.

Next, as shown in Fig. 4.2(b), we populate the IBZ volume with a set of regularly spaced points, selected from the points of the $\{n_{k_1}, n_{k_2}, n_{k_3}\}$ mesh that fall within this volume.

Finally, a constrained Delaunay tetrahedralization is constructed using the TETGEN code [123], in which the boundary triangulation is maintained and the volume-nodes are added as Steiner points. The resulting tetrahedral tessellation of the FCC IBZ example is shown in Fig. 4.2(c), in which some of the tetrahedra on the upper part have been removed for ease of visualization.

4.2.3 Linear tetrahedron method and triangle mesh refinement

Filling the IBZ volume with tetrahedra, as described in Sec. 4.2.1, allows us to apply the linear tetrahedron method [120] in order to obtain a numerical representation of the irreducible Fermi surface in terms of a triangle mesh.

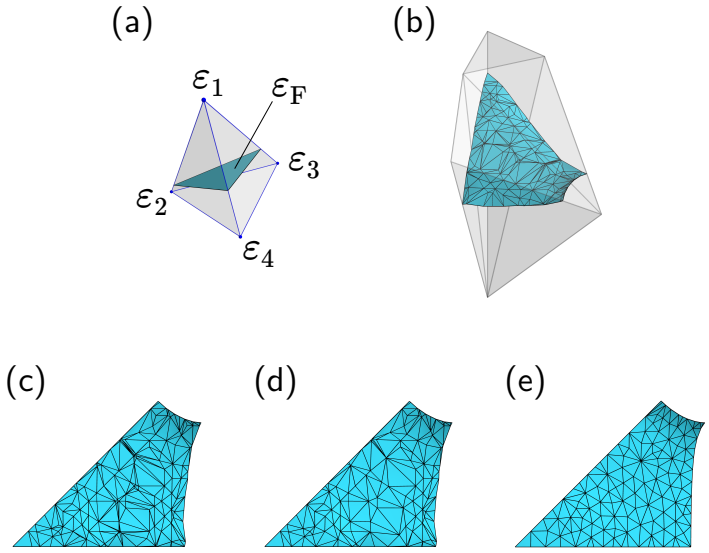

Figure 4.3. High-quality triangulated Fermi surface mesh within the irreducible wedge of the BZ. (a) The linear tetrahedron method is applied in each of the fine tetrahedra shown in Fig. 4.2(c). The electronic energies are computed at the four vertices of each tetrahedra, represented by $\varepsilon_{1,\dots,4}$. A linear interpolation among the values at the corners gives an approximation to the points in which the isosurface crosses the tetrahedral edges. (b) In this way, a triangulated Fermi surface mesh is obtained in the irreducible wedge. (h),(i),(j) Several mesh-refinement techniques are applied to the irreducible Fermi surface, resulting in a high-quality triangulated mesh.

Following this method, each tetrahedron marks four points in the reciprocal space in which the energies have to be computed, as represented schematically in Fig. 4.3(a) by $(\varepsilon_1, \varepsilon_2, \varepsilon_3, \varepsilon_4)$. Then we check if the energy corresponding to the isosurface lies within the values at the corners of the tetrahedron. In the affirmative case, a linear interpolation among the values at the corners gives an approximation to the points in which the isosurface crosses the tetrahedral edges. Depending on the number of edges that the isosurface crosses, one or two triangles can be formed inside the tetrahedron, as discussed in detail, for example, in Ref.[119] Appendix A. The simplest case is shown in Fig. 4.3(a), in which the isosurface (denoted as ε_F) crosses three of the tetrahedral edges, directly forming a triangle inside. All the triangles constructed in this way form a two-dimensional triangle mesh, representing numerically the Fermi surface within the IBZ.

As an example, we show in Fig. 4.3(b) the isosurface obtained for FCC-Cu from the tetrahedral tessellation of the IBZ shown in Fig. 4.2(c). A clearer view of the triangle mesh formed in this example is shown in Fig. 4.3(c).

As it can be noted from this figure, even if a good initial tetrahedral tessellation is provided, the resulting triangular mesh may be of a low quality, meaning that the isosurface may present an inhomogeneous density of vertices which will most likely form a set of triangles with a poor aspect ratio. Although not strictly necessary, it is highly desirable to incorporate procedures to improve the quality of the mesh, possibly eliminating redundant and poor-quality triangles. We have implemented two different mesh refinement techniques, namely the mesh-simplification and the vertex-relaxation procedures [124]. Special care has been taken with the vertices at the BZ boundary, so that the borders of the irreducible Fermi surface are preserved and the $\mathcal{S} + \mathbf{G}$ symmetries are maintained after the refinement process.

In the mesh-simplification procedure, triangles with a poor shape-quality are detected first, following the criteria that one of their edges is much shorter than the perimeter of the triangle, up to a given threshold value. This short edge is collapsed, so that one vertex and one triangle are removed from the mesh, though maintaining the original topology. This procedure is repeated iteratively until all poor shape-quality triangles are eliminated. The simplified mesh obtained after this procedure in the FCC-Cu example is shown in Fig. 4.3(d).

The so-called vertex-relaxation procedure consists of two steps. First, a tangential relaxation of the vertices is performed. Each vertex is moved from its position seeking a homogeneous distance with respect to all of its neighbor vertices. However, this movement is constrained to the tangential plane of the vertex, defined by its velocity vector, $\mathbf{v}_{n\mathbf{k}} = \nabla\varepsilon_{n\mathbf{k}}/\hbar$. Note that this vector for a $\mathbf{k}$-point at the Fermi surface is, by definition, the normal vector of the Fermi surface at this point. The Fermi velocities $\mathbf{v}_{n\mathbf{k}}$ at the triangular vertices are computed efficiently by means of the Wannier interpolation method [56, 57, 125] (see Sec. 2.2). This procedure is repeated iteratively for all the vertices in the mesh, resulting in a homogeneous distribution of triangles with similar areas. Finally, the vertices are relaxed along the direction of their normal vector. This additional step compensates the error introduced by the linear interpolation in the regular linear tetrahedron method, so that the final relaxed vertices are located at ε_F to a great accuracy [119].

The final refined mesh for the FCC-Cu example is shown in Fig. 4.3(e), where the improvement in the quality of the mesh is clearly appreciated. These mesh refinement techniques translate into a considerable accuracy and efficiency gain in the computation of Fermi surface integrals.

4.2.4 Rotation to a fully symmetric Fermi surface

The very last step in our scheme consists in applying all the symmetry operations to the irreducible Fermi surface obtained by the procedures described in the previous sections, in order to get a fully symmetric Fermi

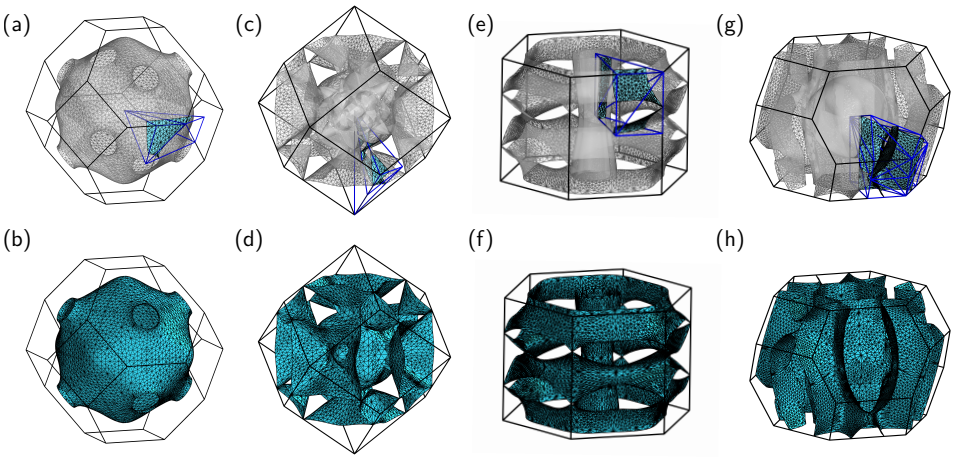

Figure 4.4. Fully symmetric triangulated Fermi surfaces. (a) The refined irreducible Fermi surface mesh for FCC-Cu is rotated by applying all the point group symmetry operations of the crystal, so that the complete fully symmetric Fermi surface mesh is obtained (b). (c)–(d), (e)–(f) and (g)–(h) Show the irreducible and fully symmetric Fermi surface meshes obtained using the same procedure for BCC-YH_6, HEX-MgB_2 and RHL-CaC_6, respectively.

surface mesh which is invariant under all the symmetry operations of the crystal up to numerical precision.

The irreducible part of the Fermi surface of the FCC-Cu example is shown within the full BZ in Fig. 4.4(a). The complete Fermi surface mesh obtained by rotation of the irreducible part is shown in Fig. 4.4(b). As it can be appreciated in the figure, our procedure provides a high-quality triangulated Fermi surface, which fulfills all the symmetries of the crystal.

We note that our procedure is completely general and valid for systems with different symmetries. As illustrative examples, we show in Fig. 4.4(c)–(d), (e)–(f) and (g)–(h) the irreducible and fully symmetric Fermi surface meshes obtained using the same procedure for BCC-YH_6, HEX-MgB_2 and RHL-CaC_6, respectively.

4.3 Symmetries on the HFSH basis set

Clearly, the symmetries of the surface on which Eq. 4.1 is defined translate into symmetric properties of the HFSH basis set. Provided that the symmetries of the surface are exactly maintained in the triangulated mesh, these properties will be preserved in the discretized form of Eq. 4.7. The fulfillment of this requirement is guaranteed if the mesh is constructed following the procedure described in Sec. 4.2.

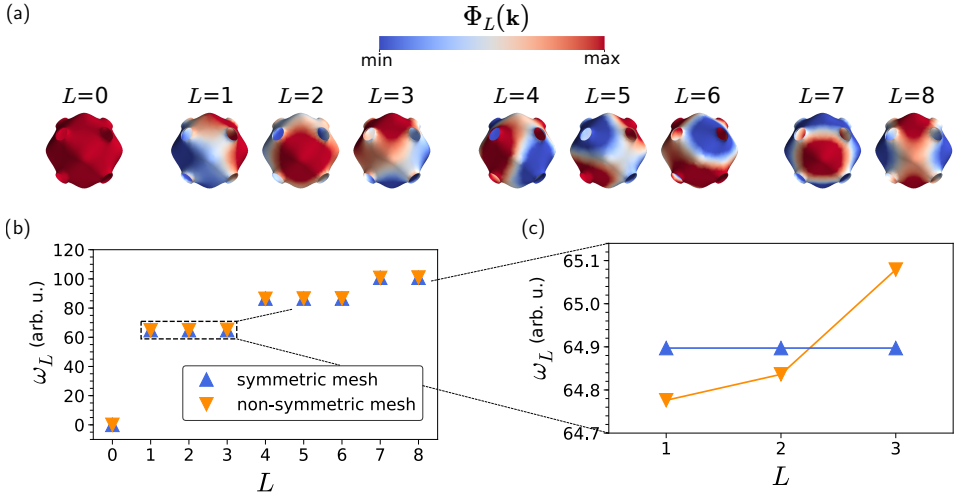

Figure 4.5. Degeneracies in the HFSH eigenmodes. (a) First nine HFSH basis functions for FCC-Cu, and (b) their corresponding eigenvalues. The eigenvalues obtained using the fully symmetric mesh are shown in blue, and the eigenvalues obtained in Ref. [119] are shown in orange for comparison. (c) Zoom on the first non-zero eigenvalues, highlighting the numerical accuracy of the degeneracy in the symmetric mesh.

In this section, we illustrate two of the most important consequences of incorporating the symmetries of the crystal in the HFSH basis set.

4.3.1 Degenerate subspaces

A straight consequence of retaining the symmetries on the surface appears in the degeneracies of the energy levels ω_L. For instance, in a perfect sphere, the full rotational symmetry enforces the 3-fold and 5-fold degeneracies in the p and d spherical harmonics, respectively. Even though the full rotational symmetry of the sphere is broken in a realistic Fermi surface due to the crystal field, the possible discrete rotational symmetries of the crystal may enforce subspaces within the HFSH basis set which are exactly degenerate.

Continuing with the FCC-Cu example, we show in Fig. 4.5(a) the first nine HFSH basis functions $\Phi_L(\mathbf{k})$, obtained as solutions of Eq. 4.7 on the symmetric mesh produced in Sec. 4.2. The corresponding eigenvalues ω_L are shown in Fig. 4.5(b), compared with the eigenvalues obtained on a mesh in which the crystal symmetries are not explicitly enforced, as in Ref [119]. As discussed in Ref. [119], the 3-fold degeneracy in the p-like harmonics is maintained, but the energies of the d-like states are split into two subspaces of 3-fold and 2-fold degeneracies.

However, a closer look reveals that these degeneracies are fulfilled only approximately on the non-symmetric mesh, as shown in Fig. 4.5(c) for the

energies of the p-like harmonics. As we can see in this figure, not incorporating the symmetries exactly on the mesh can introduce errors of $\sim 0.15\%$ in the energies. In contrast, when using the symmetric mesh we obtain equal energies up to numerical accuracy, with relative differences of the order of $\sim 10^{-10}$ in this particular example. Similar results are obtained for all the degenerate subspaces of the full HFSH basis set.

4.3.2 Fully symmetric HFSHs

As the triangular mesh in which Eq. 4.7 is solved and in which the $\Phi_L(\mathbf{k}_i)$ functions are defined is exactly symmetric, we can identify numerically those functions within the HFSH basis set that are invariant under all the symmetry operations of the crystal. We will name this subset as the *fully symmetric* HFSHs, and label them with the symbol $\tilde{L}$. Formally, they are identified as the functions within the HFSH basis set that satisfy the following condition,

$$\Phi_{\tilde{L}}(\mathcal{S}_n \mathbf{k}_i) = \Phi_{\tilde{L}}(\mathbf{k}_i) \ , \tag{4.10}$$

for all n, where $\mathcal{S}_n$ is a symmetry operation of the crystal. As an example, in the FCC-Cu case, out of the first 400 HFSH functions only 12 satisfy Eq. 4.10, and are shown in Fig. 4.6(a).

The fact that most of the physical properties defined on the Fermi surface are invariant under all the symmetry operations of the crystal imposes severe restrictions on their expansion in the HFSH basis set. As it can be directly deduced from Eq. 4.3, if a given function $F(\mathbf{k}_i)$ is fully symmetric on the FS, only those coefficients corresponding to the fully symmetric HFSHs can give a finite contribution in the expansion.

We now demonstrate that this restriction is satisfied in our implementation up to numerical precision. As an illustrative example, we consider the squared of the Fermi velocity, $F(\mathbf{k}) = v^2(\mathbf{k})$, clearly a fully symmetric function [see inset of Fig. 4.6(b)]. We show in Fig. 4.6(b) the first 400 coefficients of the expansion of this function in the HFSH basis set (see Eq. 4.4), relative to the value of the first coefficient, i.e. the FS average $v_0^2 \equiv \langle v^2(\mathbf{k}) \rangle_{\mathrm{FS}}$.

As appreciated from this figure, the values of the expansion coefficients decrease rapidly for larger HFSH indices. This trend goes in line with the fact that HFSHs with higher energies oscillate more intensely, and therefore only add finer details to the anisotropy of the expanded function. The more isotropic is the quantity to be transformed, the less are the coefficients needed for a faithful representation of its anisotropy. In the extreme case of a constant function, only the first coefficient will be finite.

Most importantly, we see that only those coefficients corresponding to the fully symmetric HFSHs shown in Fig. 4.6(a) have a finite value, being all the rest strictly zero up to numerical precision. We show this more clearly in Fig. 4.6(c), which zooms into the last two finite coefficients of Fig. 4.6(b). The magnitude of this coefficients is only $\sim 0.5\%$ of the average

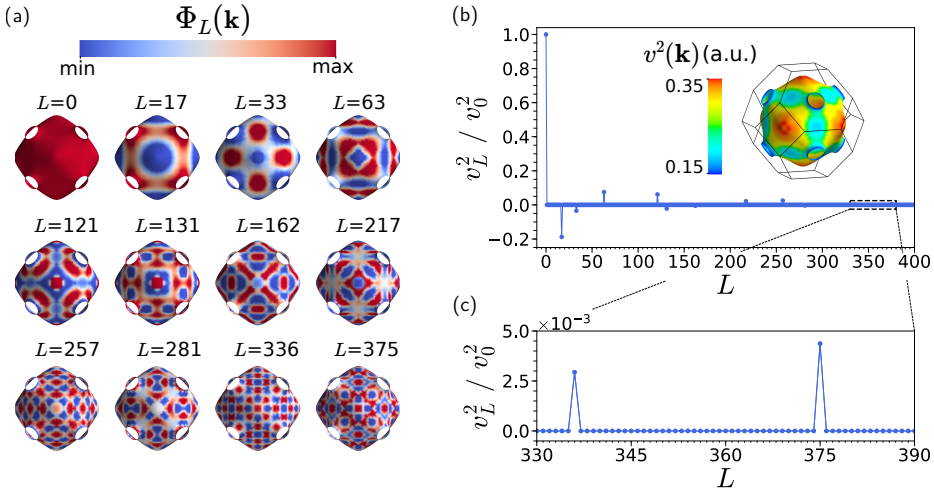

Figure 4.6. Fully symmetric HFSHs. (a) First 12 fully symmetric HFSH basis functions for FCC-Cu, together with their index in the full HFSH basis set. (b) First 400 expansion coefficients in the HFSH basis set for the squared modulus of the electron velocity, relative to the $L = 0$ coefficient. The magnitude and anisotropy of $v^2(\mathbf{k})$ over the FS is shown in the inset in atomic units. Only the fully symmetric HFSH functions shown in (a) give finite contributions, as highlighted in (c), where a zoom on the last two finite coefficients is shown.

value, showing that we can achieve this accuracy in the representation of the anisotropic function $v^2(\mathbf{k})$ of this example by using only 12 coefficients.

All in all, the use of a fully symmetric Fermi surface for the construction of the HFSH basis set, and the identification of the fully symmetric HFSH subset, allows us to obtain an extra reduction of at least one order of magnitude in the computational workload to describe anisotropic quantitites on the FS with respect to Ref. [119]. Note that this method already introduced a saving factor of approximately two orders of magnitude with respect to the conventional **k**-space representation.

4.4 Application to phonon-mediated superconductivity

One of the most exciting phenomenon driven by the electron-phonon interaction is the conventional superconductivity [21]. Ever since the first microscopic theory developed by Bardeen, Cooper and Schrieffer [126], it was noted that the superconducting pairing must take place in the vicinity of the Fermi surface when mediated by phonon excitations, due to their low energy scale.

This fact allows for an effective separation of the energy and angular parts in the interaction, and makes the use of the (Helmholtz) Fermi Surface Harmonics particularly appealing in the theory of phonon-mediated superconductivity [116]. Indeed, the seminal work by Allen and Mitrovic [22], which is considered an unmissable reference in the field, is written entirely in the language of the FSHs. However, due to the technical difficulties involved in the definition of the original basis functions, the equations derived in this reference have only been implemented in practice for isolated cases and invoking further approximations in the anisotropy of the electron-phonon interaction [127]. In this section, we present the first practical implementation of the full Eliashberg equations of superconductivity in the HFSH representation, showing that their numerical solution yields an efficiency gain of several orders of magnitude with respect to the conventional representation in momentum space.

4.4.1 Eliashberg equations of superconductivity

By virtue of the difference between electron and phonon energy-scales, the many-body description of the phonon-mediated superconductivity can be reduced to a set of two coupled nonlinear integral equations defined on the Fermi surface, which are the so-called Eliashberg equations [20, 22, 128],

$$Z_{\mathbf{k}}(i\omega_j) = 1 + \frac{\pi k_B T}{\omega_j N_F \Omega_{\mathrm{BZ}}} \sum_{j'} \int_{S_F} \frac{ds_{\mathbf{k}'}}{v_{\mathbf{k}'}} \, R^Z_{\mathbf{k}'}(i\omega_{j'}) \, \lambda_{\mathbf{k},\mathbf{k}'}(i\omega_j - i\omega_{j'}) \, , \quad (4.11)$$

$$\phi_{\mathbf{k}}(i\omega_j) = \frac{\pi k_B T}{N_F \Omega_{\mathrm{BZ}}} \sum_{j'} \int_{S_F} \frac{ds_{\mathbf{k}'}}{v_{\mathbf{k}'}} \, R^\phi_{\mathbf{k}'}(i\omega_{j'}) \, [\lambda_{\mathbf{k},\mathbf{k}'}(i\omega_j - i\omega_{j'}) - \mu^*(\omega_c)] \, , \quad (4.12)$$

where the following auxiliary definitions have been used:

$$R^Z_{\mathbf{k}}(i\omega_j) = \frac{\omega_j Z_{\mathbf{k}}(i\omega_j)}{\sqrt{(\omega_j Z_{\mathbf{k}}(i\omega_j))^2 + \phi_{\mathbf{k}}(i\omega_j)^2}} \, , \quad (4.13)$$

and,

$$R^\phi_{\mathbf{k}}(i\omega_j) = \frac{\phi_{\mathbf{k}}(i\omega_j)}{\sqrt{(\omega_j Z_{\mathbf{k}}(i\omega_j))^2 + \phi_{\mathbf{k}}(i\omega_j)^2}} \, . \quad (4.14)$$

The self-consistent solution of Eqs. (4.11)–(4.14) determine completely the so-called renormalization factor $Z_{\mathbf{k}}$ and the pair-field $\phi_{\mathbf{k}}$ at a given temperature T. The resulting pair-field ϕ will be finite only for temperatures below the superconducting transition temperature ($T \leq T_c$). All the thermodynamic properties of superconductors, such as the specific heat, can be fully determined from the knowledge of these two functions [129]. In order to

deduce the spectral properties of superconductors, such as their ARPES spectra or the tunneling density of states, an analytic continuation $i\omega_j \to \omega + i\eta$ to the real-axis has to be performed [40]. For completeness, the main points of the derivation of Eqs. (4.11)–(4.14) are reviewed in Appendix A.

The nonlinear character of the equations introduces numerical difficulties to achieve self-consistency for $T \approx T_c$, where the magnitude of the pair-field becomes vanishingly small ($\phi << Z$). In this regime, one can linearize the equations by dropping the ϕ^2 terms in the denominators of Eqs. (4.13)–(4.14). After this simplification, Eq. (4.11) can be inserted in Eq. (4.12). In this way, we are left with a single linear equation for $\Delta_{\mathbf{k}} \equiv \frac{\phi_{\mathbf{k}}}{Z_{\mathbf{k}}}$, identified as the superconducting gap [130], which reads [22]

$$\Delta_{\mathbf{k}}(i\omega_j) = \sum_{j'} \int_{S_F} \frac{ds_{\mathbf{k}'}}{v_{\mathbf{k}'}} \frac{\pi k_B T}{N_F\, \omega_{j'}} K_{\mathbf{k},\mathbf{k}'}(j-j')\, \Delta_{\mathbf{k}'}(i\omega'_j) \ . \tag{4.15}$$

In Eq. (4.15), we have defined

$$\begin{aligned} K_{\mathbf{k},\mathbf{k}'}(j-j') = {} & \lambda_{\mathbf{k},\mathbf{k}'}(i\omega_j - i\omega_{j'}) \ - \ \mu^*(\omega_c) \\ & - \delta^{(2)}_{\mathbf{k}\mathbf{k}'} \delta_{jj'} \sum_{j''} \frac{1}{N_F} \int_{S_F} \frac{ds_{\mathbf{k}''}}{v_{\mathbf{k}''}} \lambda_{\mathbf{k},\mathbf{k}''}(i\omega_j - i\omega_{j''}) \ , \end{aligned} \tag{4.16}$$

and $\delta^{(2)}_{\mathbf{k}\mathbf{k}'}$ is defined as

$$\frac{1}{N_F} \int_{S_F} \frac{ds_{\mathbf{k}'}}{v_{\mathbf{k}'}} \delta^{(2)}_{\mathbf{k}\mathbf{k}'} f_{\mathbf{k}'} = f_{\mathbf{k}} \ . \tag{4.17}$$

Note that Eq. (4.15) can be identified as a linear eigenvalue problem. However, in cases where a dense sampling of the FS is needed for a faithful description of the electron-phonon anisotropy, the matrix $K_{\mathbf{k},\mathbf{k}'}$ takes a prohibitively large size to be diagonalized.

Alternatively, one could solve Eqs. (4.11)–(4.14) self-consistently in a range of temperatures, and identify the highest T resulting in a non-vanishing pair amplitude as T_c. However, the dense $\mathbf{k}$-point sampling needed to converge the integrals, together with the numerical difficulties to achieve self-consistency for $T \approx T_c$ where $\phi << Z$, turn the determination of T_c by these means extremely involved computationally.

Transformation to the HFSH representation

An alternative representation of the Eliashberg equations of superconductivity can be obtained by rewriting all the scalar $\mathbf{k}$-dependent quantities as expansions in the HFSH basis set [see Eq. (4.3)]. In this way, Eqs. (4.11)–(4.12)

take the form

$$Z_L(i\omega_j) = \delta_{L0} + \frac{\pi k_B \mathrm{T}}{\omega_j} \sum_{j'L'} R^Z_{L'}(i\omega_{j'})\, \lambda_{L,L'}(i\omega_j - i\omega_{j'}) \ , \quad (4.18)$$

$$\phi_L(i\omega_j) = \pi k_B \mathrm{T} \sum_{j'L'} R^\phi_{L'}(i\omega_{j'}) \left[\lambda_{L,L'}(i\omega_j - i\omega_{j'}) - \mu^*(\omega_c)\, \delta_{L0,L'0}\right] \ , \quad (4.19)$$

where all the anisotropy of the electron-phonon interaction is encoded in the coefficients

$$\lambda_{L,L'}(i\omega) = \frac{\int_{S_F} \frac{ds_{\mathbf{k}}}{v_{\mathbf{k}}} \int_{S_F} \frac{ds_{\mathbf{k}'}}{v_{\mathbf{k}'}}\, \lambda_{\mathbf{k},\mathbf{k}'}(i\omega)\, \Phi_L(\mathbf{k})\, \Phi_{L'}(\mathbf{k}')}{\int_{S_F} \frac{ds_{\mathbf{k}}}{v_{\mathbf{k}}} \int_{S_F} \frac{ds_{\mathbf{k}'}}{v_{\mathbf{k}'}}} \ , \quad (4.20)$$

and R^Z_L and R^ϕ_L are transformed from Eqs. (4.13)–(4.14) through Eq. (4.4).

Similarly, the linearized Eq. (4.15) can be rewritten in the HFSH basis as [22],

$$\varepsilon\, \Delta_L(i\omega_j) = \sum_{j'L'} \frac{1}{|2j'+1|} \mathrm{K}_{L,L'}(j,j')\, \Delta_{L'}(i\omega_{j'}) \ , \quad (4.21)$$

where,

$$\begin{aligned} \mathrm{K}_{L,L'}(j,j') &= \lambda_{L,L'}(i\omega_j - i\omega_{j'}) - \mu^*_{L,L'}(\omega_c) \\ &- \delta_{jj'} \sum_{j''L''} \Xi_{L,L'L''}\, \lambda_{L'',0}(i\omega_j - i\omega_{j'})\, \mathrm{sgn}(j)\, \mathrm{sgn}(j'') \ , \end{aligned} \quad (4.22)$$

and $\Xi_{L,L'L''}$ are the Clebsch-Gordan coefficients of Eq. (4.6). The temperature at which the maximum eigenvalue ε equals unity gives T_c, since in that case the linearized Eliashberg equation Eq. (4.15) is fulfilled.

In the case of conventional s-wave superconductors, both $Z_{\mathbf{k}}$ and $\phi_{\mathbf{k}}$ must be invariant under all the symmetry operations of the crystal. As a result, only the fully symmetric HFSH functions $\{\Phi_{\tilde{L}}\}$ fulfilling Eq. (4.10) will contribute to their expansions. In this way, Eqs. (4.18)–(4.19) can be effectively reduced to this fully symmetric subset. Moreover, if the coefficients $\lambda_{L,L'}$ are shown to decay rapidly for increasing indices, a cutoff can be applied in the sums of Eqs. (4.18)–(4.19) and Eq. (4.21) without any loss accuracy.

Due to the complications introduced by the $\mathbf{k}$-dependence in Eqs. (4.11)–(4.15), the most popular practice is to neglect the anisotropy of the problem altogether and approximate the electron-phonon interaction by the double FS average of Eq. (A.9). This approximation is retrieved from the HFSH representation by simply considering the $L = 0$ components in the expansions. Nevertheless, the modern computational capabilities have allowed to explore the role of the anisotropy in the superconducting properties through the direct solution of Eqs. (4.11)–(4.15) in momentum space, demonstrating its crucial role in several cases [19, 20, 131, 132].

The HFSH representation is the ideal approach to bridge the two approaches, since it has the ability to incorporate all the anisotropy of the problem in a few coefficients. This allows for the numerical solution of Eqs. (4.18)–(4.19) and Eq. (4.21) in notably reduced subspaces, which translates into a computational cost comparable to that of the isotropic approximation, but with full anisotropic accuracy. In the next section, we provide benchmark calculations which verify this assertion in practical calculations.

4.4.2 Benchmark calculations in MgB_2

As a first example we consider the prototypical anisotropic phonon-mediated superconductor MgB_2. Its Fermi surface is composed of four different sheets, two inner cylindrical sections formed by σ bands and two outer three-dimensional sections formed by π bands [133]. The distinct orbital character of the different bands crossing the Fermi level implies that the electron-phonon coupling varies strongly among the different FS sheets [134], and considerably within each FS sheet [10, 20, 135]. As a matter of fact, MgB_2 represents the first instance in which a full anisotropic account of the electron-phonon interaction has been necessary to properly reproduce the experimentaly measured critical temperature and superconducting gap [19].

The calculation parameters have been chosen with the aim of making the comparison with previous works as direct as possible. The ground state calculations have been performed with the QUANTUM ESPRESSO package [136] within the local density approximation of density functional theory [137] in a 24^3 **k**-point grid, using norm-conserving pseudopotentials and a kinetic energy cutoff of 60Ry in the plane-wave expansion of valence electronic wave functions. The lattice parameters have been set to the experimental values of $a = 5.832$ Bohr and $c/a = 1.142$ [138]. Phonon properties have been computed within density functional perturbation theory [8] on a 8^3 **q**-point grid. Electron-phonon matrix elements have been computed on a coarse $(8^3, 8^3)$ **k** and **q**-point grid, and the Wannier interpolation method [9, 10, 14, 18, 78] has been used to interpolate the matrix elements to the triangular vertices (see Sec. 2.2).

Anisotropic mass-enhancement parameter

As a first representative anisotropic quantity related to the electron-phonon problem, we consider the momentum-dependent mass enhancement parameter for electron states at the FS,

$$\lambda_{n\mathbf{k}} = \frac{2}{\Omega_{\mathrm{BZ}}} \sum_{m\nu} \int_{S_F} \frac{d^2 s_{\mathbf{k}'}}{v(\mathbf{k}')} \frac{|g^{\nu}_{mn}(\mathbf{k}, \mathbf{k}')|^2}{\omega^{\nu}_{\mathbf{k}'-\mathbf{k}}} \,. \tag{4.23}$$

The $\lambda_{n\mathbf{k}}$ parameter is the most meaningful measure of the quasiparticle renormalization driven by electron-phonon interactions. Its average over the

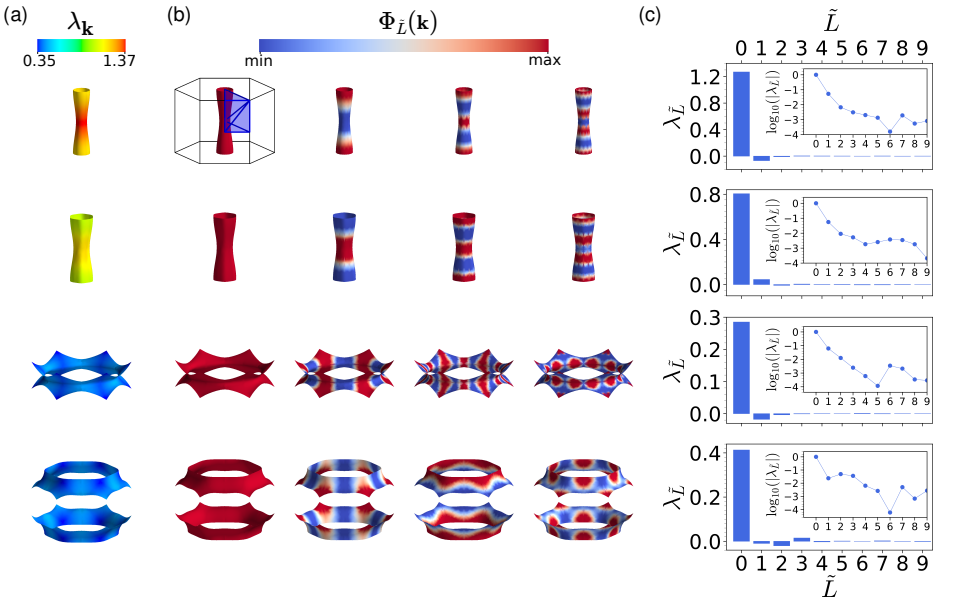

Figure 4.7. HFSH representation of the anisotropic mass enhancement parameter $\lambda_{\mathbf{k}}$ in MgB_2. (a) $\lambda_{\mathbf{k}}$ on the Fermi surface of MgB_2, separated in the four different FS sheets. (b) First four fully symmetric HFSH basis functions for each FS sheet. The hexagonal BZ and the corresponding IBZ is shown in the top left corner. (c) First ten expansion coefficients of $\lambda_{\mathbf{k}}$ for each FS sheet in the fully symmetric HFSH subset. The inset shows the same result with a logarithmic scale on the y-axis.

FS is a central parameter in simplified expressions for the critical temperature of superconductors [139, 140], and its two-index and frequency-dependent generalization of Eq. (A.11) is crucial in the full Eliashberg theory of superconductivity, as it can be appreciated from Eqs.(4.11) and (4.12).

We show in Fig. 4.7(a) our results for the anisotropic mass-enhancement parameter of MgB_2, in which the four different FS sheets have been separated for clarity. In agreement with previous works [10, 20, 135], we find that $\lambda_{n\mathbf{k}}$ takes considerably large values in the range of 1.00–1.37 on the cylinder-like FS sheets corresponding to the σ bands. In contrast, the FS sheets formed by the π bands couple much less efficiently to phonons, resulting in smaller $\lambda_{n\mathbf{k}}$ values in the range of 0.35–0.47. Apart from the arrangement of the absolute values of the $\lambda_{n\mathbf{k}}$ parameter in two main groups, this figure also shows that its anisotropy within each FS sheet is sizable.

For the Fermi surface averaged mass-enhancement parameter we obtain $\lambda = 0.73$, also in very good agreement with previous calculations [10, 20, 135]. In particular, we find that our results agree very well with the values presented in Ref. [20], where a systematic convergence test of λ with respect to the $\mathbf{k}$-point sampling was performed. Remarkably, while they showed that $\sim 10^5$

k-points are needed in the three-dimensional BZ to obtain converged results when approximating the FS with a smearing function, we already obtain convergence in the average value and the distribution of $\lambda_{\mathbf{k}}$ with $\sim 8 \times 10^3$ points in the triangulated Fermi surface.

Now we move on to the HFSH representation. Being a scalar quantity, the $\lambda_{n\mathbf{k}}$ parameter is invariant under all the symmetry operations of the crystal, as it can be appreciated in Fig. 4.7(a). Therefore, as discussed in Sec. 4.3.2, its expansion will only have finite coefficients in the fully symmetric HFSH subset,

$$\lambda_{n,\tilde{L}} = \frac{\int_{S_{F_n}} \frac{d^2 s_{\mathbf{k}}}{v(\mathbf{k})} \; \Phi_{n,\tilde{L}}(\mathbf{k}) \; \lambda_{n\mathbf{k}}}{\int_{S_{F_n}} \frac{d^2 s_{\mathbf{k}}}{v(\mathbf{k})}} \; . \tag{4.24}$$

Note that the HFSH functions for each FS sheet are independent by construction [119] , and that the integrals are performed over the corresponding sheet S_{F_n}.

We show in Fig. 4.7(b) the first four fully symmetric HFSH functions for the different FS sheets of MgB_2. The first HFSH function is always the trivial constant solution with eigenvalue $\omega_{\tilde{L}} = 0$, and the following ones oscillate more and more rapidly in direct analogy with the normal modes of a vibrating membrane. The first ten $\lambda_{n,\tilde{L}}$ coefficients given by Eq. 4.24 are shown in Fig. 4.7(c). As it can be anticipated from Eq. (4.3) and by looking at the HFSH functions of Fig. 4.7(b), the $\tilde{L} = 0$ coefficient gives the average value of $\lambda_{n\mathbf{k}}$ in each FS sheet, and the subsequent coefficients add finer and finer anisotropic details. It is therefore reassuring to see that the magnitude of the $\lambda_{n,\tilde{L}}$-s decay very quickly for bigger $\tilde{L}$-s. What is more remarkable is the rate at which the coefficients decay. In order to analyze this point further we plot in the insets of Fig. 4.7(c) the same result but using a logarithmic scale in the y-axis, revealing that the value of the coefficients decay very rapidly.

Indeed, this result demonstrates that the transformation from **k**-space to the HFSH representation turns out strikingly beneficial, as all the details of the $\lambda_{n\mathbf{k}}$ parameter can be compressed with a relative accuracy of at least 10^{-3} in as few coefficients as 10 $\lambda_{\tilde{L}}$-s per FS sheet. In comparison with the ~ 8000 triangular vertices needed in **k**-space, this simplification implies a saving factor of $\sim 2 \times 10^2$ with no loss of accuracy.

We now extend the same procedure to the two-index mass-enhancement parameter of Eq. (A.11). For simplicity, we focus on the most anisotropic outer σ sheet. In Fig. 4.8(a), we represent the anisotropic $\lambda_{\mathbf{k},\mathbf{k}'}$ parameter in a matrix form, computed from first principles on the discrete mesh of $\mathbf{k}, \mathbf{k}'$ points forming the triangularly tessellated Fermi surface. This example represents a typical scenario where a dense sampling of $n_k \times n_{k'} \sim 10^4 \times 10^4$ points is needed to obtain a converged solution of Eqs. (4.11)–(4.14), as $\lambda_{\mathbf{k},\mathbf{k}'}$ varies considerably from point to point on the Fermi surface. In contrast, by transforming this quantity to the HFSH representation, all of its anisotropic

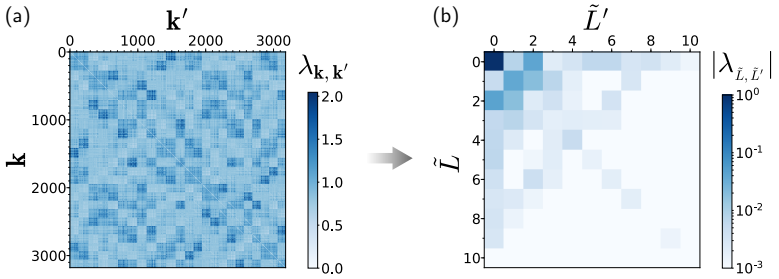

Figure 4.8. HFSH representation of the two-index anisotropic mass enhancement parameter $\lambda_{\mathbf{k},\mathbf{k}'}$ in MgB_2. (a) $\lambda_{\mathbf{k},\mathbf{k}'}$ computed from first principles on a discretized mesh of triangular vertices on the outer σ Fermi surface sheet of MgB_2, unfolded into a matrix representation. In this example, the isosurface is formed by $\sim 3 \times 10^3$ vertices. (b) Magnitude, in logarithmic scale, of the first 10×10 fully symmetric HFSH coefficients of the two-index mass enhancement parameter $\lambda_{\tilde{L},\tilde{L}'}$ on this Fermi surface sheet. Coefficients for larger $\tilde{L}$-s are smaller than 10^{-3} in magnitude.

details can be described by a handful of coefficients. We show the magnitude of the first $\lambda_{\tilde{L},\tilde{L}'}$ coefficients, as obtained by Eq. 4.20, are given in Fig. 4.8(b) in logarithmic scale. All the elements beyond this 10×10 matrix are lower than 10^{-3} in magnitude, and therefore give a negligible contribution to the sums in Eqs. (4.18)–(4.19). This implies that these equations can be solved in such a drastically reduced subspace, with virtually no loss of accuracy. In comparison, when solving Eqs. (4.11)–(4.14) directly on $\mathbf{k}$-space, the full $\lambda_{\mathbf{k},\mathbf{k}'}$ matrix has to be used as no cutoff can be applied in this case.

Anisotropic superconducting gap

In the following, we check the effect of the simplification introduced by the HFSH representation in the full solution of the Eliashberg equations of superconductivity. For that purpose, we solve Eqs. (4.18)–(4.19) for MgB_2 at $T = 10$ K, using different cutoff values in the sums, which we denote by $n_{\tilde{L}}$. We show in Fig. 4.9 our results for the calculated superconducting gap on the Fermi surface,

$$\Delta_{\mathbf{k}}^{n_{\tilde{L}}} = \frac{\phi_{\mathbf{k}}^{n_{\tilde{L}}}}{Z_{\mathbf{k}}^{n_{\tilde{L}}}} = \frac{\sum_{\tilde{L}}^{n_{\tilde{L}}} \phi_{\tilde{L}}\, \Phi_{\tilde{L}}(\mathbf{k})}{\sum_{\tilde{L}}^{n_{\tilde{L}}} Z_{\tilde{L}}\, \Phi_{\tilde{L}}(\mathbf{k})} \,, \tag{4.25}$$

using $n_{\tilde{L}} = 16$, four per Fermi surface sheet. The Matsubara frequency cutoff has been set to ten times the maximum phonon energy, and $\mu^* = 0.16$ has been used. The value of the gap at the FS has been approximated by its value at the lowest Matsubara frequency ($j \equiv 0$).

In very good agreement with previous reported calculations [20], we see that $\Delta_{\mathbf{k}}$ clusters into two ranges of values of $(1.4, 2.2)$ meV and $(8.0, 9.3)$ meV

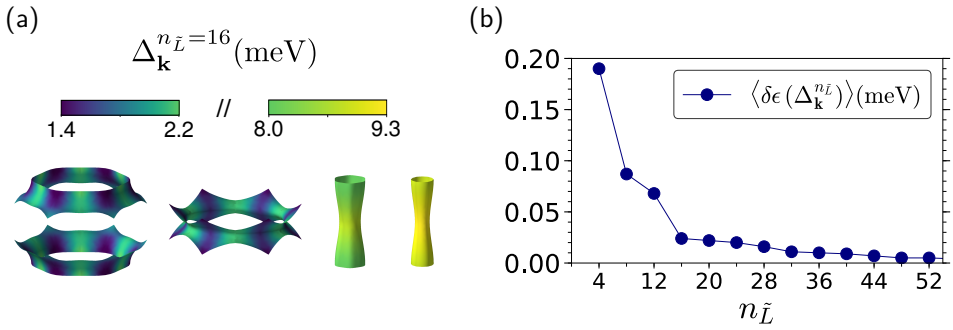

Figure 4.9. Anisotropic superconducting gap in MgB_2 through the solution of the Eliashberg equations in the HFSH representation. (a) Magnitude of the superconducting gap $\Delta_{\mathbf{k}}^{n_{\tilde{L}}}$ on the Fermi surface of MgB_2 at 10 K, obtained after solving the anisotropic Eliashberg equations in the HFSH representation, with a cutoff of $n_{\tilde{L}} = 16$. (b) Average of the absolute error of $\Delta_{\mathbf{k}}^{n_{\tilde{L}}}$ for different values $n_{\tilde{L}}$, with respect to the result obtained by considering all the symmetric HFSHs in the sums.

for the σ and π Fermi surface sheets, respectively, varying considerably within each sheet. The comparison with the experimentally measured two-gap structure is also very good [141–144].

Fig. 4.9(b) shows the average of the absolute error of $\Delta_{\mathbf{k}}^{n_{\tilde{L}}}$ for different values of $n_{\tilde{L}}$, with respect to the fully converged calulation in which all the symmetric HFSHs are considered in the sums,

$$\langle\, \delta\epsilon\,(\Delta_{\mathbf{k}}^{n_{\tilde{L}}})\,\rangle = \frac{\int_{S_F} ds_{\mathbf{k}}\, |\Delta_{\mathbf{k}}^{n_{\tilde{L}}} - \Delta_{\mathbf{k}}^{n_{\tilde{L}_{\max}}}|}{\int_{S_F} ds_{\mathbf{k}}} \,. \tag{4.26}$$

We see that the error drops rapidly with the size of the subspace. For a basis size as small as $n_{\tilde{L}} = 16$, the error as defined above is ~ 0.025 meV, well below the current experimental resolution [144]. Besides the negligible loss of accuracy, the efficiency gain with respect to state of the art approaches is immense. Taking Ref. [20] as an example, in order to obtain fully converged calculations of the superconducting gap for the very same system, a Brillouin zone sampling of $n_{\mathbf{k}} = 50^3 = 1.25 \times 10^5$ $\mathbf{k}$-points was needed in momentum space. Our method, in comparison, brings an efficiency gain factor of $n_{\mathbf{k}}/n_{\tilde{L}} \sim 10^4$.

Another important advantage of the HFSH representation is that all the information about the superconducting state is encoded effectively in the few resulting $Z_{\tilde{L}}$ and $\Phi_{\tilde{L}}$ coefficients. This facilitates the comparison between calculations using different meshes and the interpretation of experimental measurements, in a similar spirit as it is done when comparing Fermi surface averaged values — simply given by the $\tilde{L} = 0$ coefficients in the HFSH representation —, but generalized to full anisotropic detail.

4.4.3 Superconducting transition temperature in YH_6

Compressed hydrides have been attracting an enormous interest during the last years, specially since the prediction and discovery of conventional high-temperature superconductivity in hydrogen sulfide under high pressures [145–147]. Developing methods to alleviate the computational cost of calculating superconducting properties appears particularly interesting in this research field, in which theoretical predictions of new candidates guide the experimental efforts to find materials with increasingly favorable properties [148, 149]. YH_6 represents an interesting case within this class of materials, as the very recent experimental confirmation of superconductivity in this system [150, 151] has revealed a sizable deviation in the measured critical temperature with respect to the theoretical predictions [152–154].

We have considered YH_6 at 300GPa in the BCC structure, with the lattice parameter $a = 3.369\,\text{Å}$ as in [154]. Ground state calculations have been performed in a 12^3 **k**-point grid within the generalized gradient approximation of density functional theory [155], using norm-conserving pseudopotentials of the Goedecker-Hartwigsen-Hutter-Teter table [156, 157]. Phonon properties and electron-phonon matrix elements have been computed on a coarse 4^3 **q**-point grid, and later interpolated to the triangular vertices forming the FS by the Wannier interpolation method (see Sec. 2.2). A tessellation consisting of $\sim 7.5 \times 10^3$ vertices has been needed in this case to obtain converged results. In good agreement with previous calculations [154], we obtain a Fermi surface composed of three small electron pockets around the Γ point, two bigger and strongy anisotropic sheets, and a hole pocket around the P point at the BZ boundary.

We show our results for the superconducting gap on the six Fermi surface sheets at 40 K in Fig. 4.10(a), where a converged cutoff of $n_{\tilde{L}} = 48$ has been used in the HFSH expansions to solve Eqs. (4.18)–(4.19). The Coulomb pseudopotential parameter has ben set to $\mu^* = 0.11$ as in Ref. [154].

We obtain a continuous range of values of $(25, 47)$ meV for $\Delta_{\mathbf{k}}$, being its anisotropy particularly large on the biggest sheets. Our results are in qualitative agreement with the ones reported Ref. [154], while quantitatively we obtain smaller gap values. We trace back this discrepancy to the finer Fermi surface integrations provided by our triangulated mesh, which also reflects in a smaller magnitude of the electron-phonon mass-enhancement parameter: we obtain a FS averaged value of $\lambda = 1.5$, where a value of $\lambda = 1.9$ is reported in Ref. [154].

The distribution of the gap, $\rho(\Delta)$, obtained for different temperatures is represented by the light blue shaded areas in Fig. 4.10(b). The magnitude of the gap decreases with temperature, and we do not find superconductivity ($\phi \neq 0$) beyond ~ 230 K.

In order to determine the superconducting transition temperature more accurately, we diagonalize the linearized Eliashberg equation Eq. (4.21) for

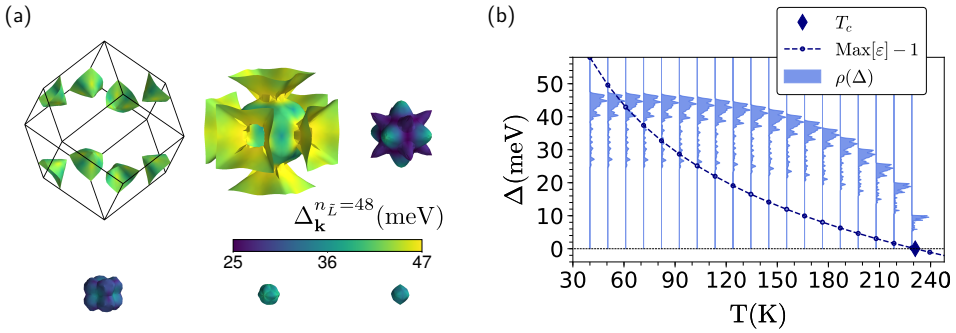

Figure 4.10. Solution of the Eliashberg equations in the HFSH representation for YH_6. (a) Magnitude of the superconducting gap on the six Fermi surface sheets of YH_6 at 300 GPa and 40 K. (b) Energy-distribution of the superconducting gap at different temperatures (light blue shaded areas). The dark blue dots represent the maximum eigenvalue of Eq. (4.21) in the same range of temperatures, displaced by -1, and the dashed line is a guide to the eye. The temperature at which $\mathrm{Max}[\varepsilon] - 1 = 0$ is fulfilled corresponds to T_c, and is represented by the blue diamond.

the same range of temperatures, and represent the maximum eigenvalue (displaced by -1 for ease of visualization) by the dark blue dots in Fig. 4.10(b). The dashed blue line is a guide to the eye. As it can be appreciated in this figure, the temperature-dependence is very smooth, allowing for an efficient use of root finding algorithms to detect the exact T for which $\mathrm{Max}[\varepsilon(T)] - 1 = 0$ is fulfilled. In particular, the secant method has been implemented in this thesis for this purpose, typically obtaining converged solutions in less than ten iterations. For $n_{\tilde{L}} = 48$, we obtain $T_c = 230.98\,\mathrm{K}$, as represented by the blue diamond in Fig. 4.10(b). This result is in good agreement with two very recent experimental measurements, which have independently reported a superconducting transition temperature of $T_c = 227\,\mathrm{K}$ at 237 GPa [151], and $T_c = 224\,\mathrm{K}$ at 166 GPa [151].

With the aim of reducing the size of the problem as much as possible, we analyze in Fig. 4.11 the sensitivity of the predicted T_c with respect to the HFSH expansion cutoff $n_{\tilde{L}}$. Interestingly, we verify that convergence is reached very rapidly, obtaining results within 1% of accuracy with as few as 30 HFSHs.

This result demonstrates that the HFSH basis set appears extremely beneficial for a precise determination of T_c with a full inclusion of the anisotropy, as the problem is reduced to a small matrix diagonalization for the small number of temperatures involved in the root finding procedure. We note, in comparison, that the state-of-the-art approach to determine the transition temperature considering anisotropy is to self-consistently solve

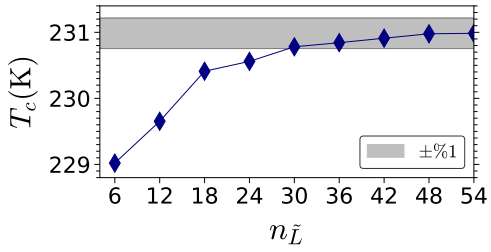

Figure 4.11. Convergence of T_c with respect to the cutoff $n_{\tilde{L}}$ applied on the HFSH expansion for solving Eq. (4.21). The grey shaded area represents the values within a 1% of accuracy with respect to the converged value, taken to be the T_c obtained with $n_{\tilde{L}} = 54$.

the non-linear Eqs. (4.11)–(4.14) in a set of $\sim 10^5$ **k**-points for a range of temperatures until no solution with $\Phi \neq 0$ is found.

4.5 Conclusion

In conclusion, we have implemented a computational procedure to obtain a high-quality triangulated Fermi surface mesh, which fulfills all the symmetries of the crystal up to numerical accuracy. This allows us to identify the fully symmetric components of the Helmholtz Fermi Surface Harmonics basis set, which give the only finite contributions in the expansions of physical symmetric quantities defined on the Fermi surface.

We have applied the procedure in the electron-phonon problem, showing that the anisotropic mass-enhancement parameter can be described to high accuracy by a handful of coefficients in the symmetric HFSH representation. This acts as an extremely effective filter, and allows for the solution of integral Fermi surface equations in remarkably reduced subspaces.

As the first application of the methodology, we have solved of the Eliashberg equations of superconductivity in the HFSH representation, allowing for an extremely efficient determination of anisotropic superconducting properties from first principles. We have illustrated the potential of the method with benchmark calculations in the prototypical anisotropic superconductor MgB_2 and the recently discovered compressed YH_6, demonstrating that our procedure introduces an efficiency gain of several orders of magnitude with respect to state-of-the-art approaches.

Chapter 5

Overview and conclusions

The main goal of this thesis was to develop new numerical techniques to expand the limits of what can be computed from first principles in the context of electron-phonon interactions. Throughout this dissertation, we have presented several methods that go beyond state-of-the-art approaches, which we summarize in the following:

- We have implemented a Wannier interpolation method for a fine frequency and momentum resolution of the low-energy electronic response function of surfaces and two-dimensional materials, including the spin-charge correlations introduced by the spin-orbit coupling.

- We have developed a procedure to analyze the real-space structure of the coupled spin-charge collective modes through the diagonalization of the generalized $(4 \times \mathbf{G}) \times (4 \times \mathbf{G}')$ dielectric response matrix.

- We have extended the piecewise polynomial method to obtain the analytic continuation of general self-energies beyond the constant-density-of-states approximation. This allows for a proper determination of quasiparticle properties on the complex-energy plane for systems with complicated electron-phonon interactions.

- We have developed a deformed contour integral procedure to access the different Riemann sheets of multivalued self-energies.

- We have taken some preliminary but important steps towards a many-body Green's function formalism to describe the localization of polaron quasiparticles in real-space.

- We have implemented a numerical scheme to incorporate the crystal symmetries in the Helmholtz Fermi Surface Harmonics basis set, through the construction of fully symmetric triangulated Fermi surface meshes of high-quality. This allows for the accurate description of

anisotropic Fermi surface quantities in terms of few symmetric elements of the set.

- We have implemented a code to solve the Eliashberg equations of superconductivity in the HFSH representation, which efficiently determines the anisotropic superconducting gaps and transition temperatures of phonon-mediated superconductors.

From the application of the developed methodologies in practical first principles calculations we can draw the following general conclusions:

- Relativistic effects introduce a sizable coupling between the charge and spin components of the electronic response in systems with inversion asymmetry and significant spin-orbit interaction. If partially populated spin-polarized bands are present, this coupling leads to a novel plasmon excitation whose spin and charge oscillations are of a similar order of magnitude.

- The electron-phonon interaction may drive qualitative changes in the band structure of doped two-dimensional semiconductors, giving rise to strongly renormalized quasiparticles with a long lifetime but a greatly enhanced effective mass.

- The Helmholtz Fermi Surface Harmonics basis set provides a remarkably simplified description of the electron-phonon interactions on the Fermi surface, in which even the symmetries and the selection rules can be incorporated by construction.

The apparently separated problems tackled in the different chapters of this thesis actually lead to interesting connections among the obtained results, and open exciting future lines of research. We name a few of them in the following:

- The nature of the coupled spin-charge response analyzed in Chapter 2 has direct physical implications in the electron-phonon problem. From the off-diagonal components of the dielectric response matrix, it appears clear that the self-consistently screened variation of the potential induced by phonons will also have finite magnetic components in systems with significant spin-orbit coupling. Indeed, explicit predictions of this effect have been very recently reported in Ref. [158], from the direct evaluation of the full phonon induced spin-charge potential within non-collinear spin Density Functional Perturbation Theory in monolayer WSe_2. The hitherto unexplored magnetic components of the phonon induced potential may lead to interesting new effects, specially in the context of spin and charge transport. Besides, our results also show that the frequency-dependence of the dielectric function at

doped semiconductor surfaces might show structures in the meV range. This can lead to interesting new physics beyond the approximation discussed in Sec. 1.4.2, such as frequency-dependent electron-phonon matrix elements, or the appearance of hybrid plasmon-phonon modes [18, 27].

- One specially interesting aspect of the expression Eq. (3.21) derived in Chapter 3, is that it is completely general and allows for the analytic continuation of any physical function fulfilling the Kramers-Kronig relations. Thus, it is readily applicable to analyze the quasiparticle renormalization induced by other many-body interactions, such as, for example, the electron-plasmon coupling [159]. Indeed, the analytic continuation for the dielectric function itself (see Chapter 2) could be obtained following a similar procedure. This would permit to determine the plasmon frequencies through a complex version of Eq. (2.8), when their decay to electron-hole excitations is not negligible. Along the same lines, the complex non-adiabatic renormalization of phonon dispersions has been analyzed recently in Ref. [18] through an approximate analytic continuation procedure. Another interesting prospect, in connection with Chapter 4, is the determination of complex Bogoljubov excitation despersions in the superconducting state [160]. Finally, the preliminary results for the many-body description of the polaron quasiparticles outlined in Sec. 3.4 are particularly promising, and a systematic effort along this line of research is certainly warranted.

- The results presented in Chapter 4 open several exciting possibilities. In the context of phonon-mediated superconductivity, for example, the unprecedented simplification introduced by the HFSH representation should allow for the hitherto unattainable exploration of vertex corrections beyond the Migdal approximation. Furthermore, the incorporation of the crystal symmetries in the set permits the unambiguous determination of unconventional superconducting gap symmetries beyond the conventional s-wave case. Most importantly, the minimal description of the Fermi surface complexity provided by this basis set opens the way towards new simplified model-theoretical treatments of diverse electron-phonon, impurity or transport problems in general.

To conclude, we believe that the methods developed throughout this thesis will help to advance in the understanding of complex many-body interactions in solids, and hopefully will make our small contribution towards uncovering exciting new physics in this thrilling field.

Appendix A

Derivation of the Eliashberg equations of superconductivity

For a quantitative description of the superconducting state amenable to practical calculations, we will follow the same lines of reasoning of Sec. 1.4, which lead to a set of equations first derived by Eliashberg in Ref. [128]. A comprehensible and detailed derivation of these equations can be consulted, for example, in Ref. [22]. A more recent review of the equations in the context of *ab initio* calculations can be found, for example, in Ref. [20]. For completeness, in this section we outline the main points.

Our starting point will be the non-interacting electron energies $\varepsilon_{n\mathbf{k}}$ obtained by DFT, the adiabatically screened phonon energies $\omega_{\mathbf{q}\nu}$ obtained by DFPT, and the electron-phonon matrix elements $g^{\nu}_{mn}(\mathbf{k},\mathbf{q})$ given by Eq. (1.35). The major deviation from the equations presented in Sec. 1.4 comes from introducing the Nambu two-component field operator [161],

$$\hat{\Psi}_{\mathbf{k}} = \begin{pmatrix} \hat{c}_{\mathbf{k}\uparrow} \\ \\ \hat{c}^{\dagger}_{-\mathbf{k}\downarrow} \end{pmatrix} , \tag{A.1}$$

where the band index n has been absorbed into the momentum index $\mathbf{k}$ for simplicity, and $\hat{c}_{\mathbf{k}\uparrow}$ ($\hat{c}^{\dagger}_{-\mathbf{k}\downarrow}$) is the destruction (creation) operator of a spin up (down) Bloch state with index $\mathbf{k}$ ($-\mathbf{k}$). From Eq. (A.1) a generalized Green's function in the form of a 2×2 matrix follows,

$$\begin{aligned} \mathbf{G}_{\mathbf{k}}(\tau) &= -\langle \hat{T}_{\tau} \hat{\Psi}_{\mathbf{k}}(\tau) \hat{\Psi}^{\dagger}_{\mathbf{k}}(0) \rangle \\ &= \begin{pmatrix} \langle \hat{T}_{\tau} \hat{c}_{\mathbf{k}\uparrow}(\tau) \hat{c}^{\dagger}_{\mathbf{k}\uparrow}(0) \rangle & \langle \hat{T}_{\tau} \hat{c}_{\mathbf{k}\uparrow}(\tau) \hat{c}_{-\mathbf{k}\downarrow}(0) \rangle \\ \langle \hat{T}_{\tau} \hat{c}^{\dagger}_{-\mathbf{k}\downarrow}(\tau) \hat{c}^{\dagger}_{\mathbf{k}\uparrow}(0) \rangle & \langle \hat{T}_{\tau} \hat{c}^{\dagger}_{-\mathbf{k}\downarrow}(\tau) \hat{c}_{-\mathbf{k}\downarrow}(0) \rangle \end{pmatrix} , \end{aligned} \tag{A.2}$$

where the braces indicate a grand-canonical thermodynamic average, and $\tau \equiv it$ is an imaginary time variable [23]. The diagonal elements correspond to the *normal* Green's function of Eq. (1.10) in the basis of KS states, and contains information about the propagation of single-electron quasiparticles. The off-diagonal components are the *anomalous* Green's functions introduced by Gor'kov [162], which account for the propagation of Cooper pairs.

Similar to Eq. (1.37) for the normal state Green's function, the 2×2 Green's function fulfills the following Dyson equation,

$$\mathbf{G}_{\mathbf{k}}(i\omega_j)^{-1} = \mathbf{G}^0_{\mathbf{k}}(i\omega_j)^{-1} - \mathbf{\Sigma}_{\mathbf{k}}(i\omega_j) \ , \tag{A.3}$$

where, the generalization of Eq. (1.33) for $\mathbf{G}^0$ is [22],

$$\mathbf{G}^0_{\mathbf{k}}(i\omega_j) = \begin{pmatrix} (i\omega_j - \varepsilon_{\mathbf{k}})^{-1} & 0 \\ 0 & (i\omega_j + \varepsilon_{\mathbf{k}})^{-1} \end{pmatrix} \ , \tag{A.4}$$

and ω_j are the so-called Matsubara frequencies [27],

$$\omega_j = (2j+1)\pi k_B T \ , \tag{A.5}$$

where T is the temperature, k_B is the Boltzmann constant, and j are integer numbers.

It is convenient to write the 2×2 self-energy in terms of the Pauli matrices $\boldsymbol{\sigma}$,

$$\mathbf{\Sigma}_{\mathbf{k}}(i\omega_j) = i\omega_j \left[1 - Z_{\mathbf{k}}(i\omega_j)\right] \boldsymbol{\sigma}_0 + \chi_{\mathbf{k}}(i\omega_j)\boldsymbol{\sigma}_3 + \phi_{\mathbf{k}}(i\omega_j)\boldsymbol{\sigma}_1 + \bar{\phi}_{\mathbf{k}}(i\omega_j)\boldsymbol{\sigma}_2 \ , \tag{A.6}$$

where the four independent functions Z, χ, ϕ and $\bar{\phi}$ are yet to be determined. Inverting the Dyson Eq. (A.3), the Green's function takes the general form,

$$\mathbf{G}_{\mathbf{k}}(i\omega_j) = \frac{i\omega_j Z_{\mathbf{k}}(i\omega_j)\boldsymbol{\sigma}_0 + \left[\varepsilon_{\mathbf{k}} + \chi_{\mathbf{k}}(i\omega_j)\right]\boldsymbol{\sigma}_3 + \phi_{\mathbf{k}}(i\omega_j)\boldsymbol{\sigma}_1 + \bar{\phi}_{\mathbf{k}}(i\omega_j)\boldsymbol{\sigma}_2}{\left[i\omega_j Z_{\mathbf{k}}(i\omega_j)\right]^2 - \left[\varepsilon_{\mathbf{k}} - \chi_{\mathbf{k}}(i\omega_j)\right]^2 - \phi_{\mathbf{k}}(i\omega_j)^2 - \bar{\phi}_{\mathbf{k}}(i\omega_j)^2} \ . \tag{A.7}$$

The Eliashberg theory of superconductivity consists on extending the Migdal approximation discussed in Sec. 1.4.1 to the superconducting state, so that the electron-phonon self-energy takes the form [22],

$$\mathbf{\Sigma}^{\mathrm{ep}}_{\mathbf{k}}(i\omega_j) = k_B T \sum_{j'\nu} \int \frac{d\mathbf{k}'}{\Omega_{\mathrm{BZ}}} \boldsymbol{\sigma}_3 \, \mathbf{G}_{\mathbf{k}'}(i\omega_{j'}) \, \boldsymbol{\sigma}_3 \, |g^{\nu}_{\mathbf{k}\mathbf{k}'}|^2 \, \frac{2\,\omega^{\nu}_{\mathbf{k}'-\mathbf{k}}}{(\omega_j - \omega_{j'})^2 + (\omega^{\nu}_{\mathbf{k}'-\mathbf{k}})^2} \ . \tag{A.8}$$

At this point we introduce the two-index generalization of the Eliashberg function of Eq. (3.14),

$$\alpha^2 F_{\mathbf{k}\mathbf{k}'}(\omega) = N_F \sum_{\nu} |g^{\nu}_{\mathbf{k}\mathbf{k}'}|^2 \delta(\omega - \omega^{\nu}_{\mathbf{k}'-\mathbf{k}}) \ , \tag{A.9}$$

where N_F is the density of states at the Fermi level. In this way, Eq. (A.8) can be rewritten as,

$$\boldsymbol{\Sigma}^{\mathrm{ep}}_{\mathbf{k}}(i\omega_j) = \frac{k_B T}{N_F} \sum_{j'\nu} \int \frac{d\mathbf{k}'}{\Omega_{\mathrm{BZ}}} \, \boldsymbol{\sigma}_3 \, \mathbf{G}_{\mathbf{k}'}(i\omega_{j'}) \, \boldsymbol{\sigma}_3 \, \lambda_{\mathbf{k}\mathbf{k}'}(j - j') \ , \tag{A.10}$$

where we have defined,

$$\lambda_{\mathbf{k}\mathbf{k}'}(j - j') = \int_0^\infty d\omega \, \frac{2\,\omega}{(\omega_j - \omega_{j'})^2 + \omega^2} \, \alpha^2 F_{\mathbf{k}\mathbf{k}'}(\omega) \ , \tag{A.11}$$

which effectively describes all the anisotropy and the frequency-dependence of the electron-phonon coupling.

In order to proceed further, it is useful to separate the three-dimensional Brillouin zone integral into a one-dimensional integral in the energy variable ε and a two-dimensional integral in a momentum variable restricted to each energy-isosurface S_ε, that is,

$$\int d\mathbf{k} = \int d\mathbf{k} \int_{-\infty}^{\infty} d\varepsilon \ \delta(\varepsilon - \varepsilon_{\mathbf{k}}) = \int_{-\infty}^{\infty} d\varepsilon \int_{S_\varepsilon} \frac{ds_{\mathbf{k}}}{v_{\mathbf{k}}} \ , \tag{A.12}$$

where $v_{\mathbf{k}} = |\nabla \varepsilon_{\mathbf{k}}|$ is usually referred to as the electron velocity.

The small energies of phonons compared to the electronic energy scales restrict the phonon-mediated superconductivity to a very narrow window around the Fermi surface. In this window, among the quantities on the right-hand side of Eq. (A.10), the dominant energy dependence comes from the explicit ε' appearing in the denominator of Eq. (A.7). Therefore, to a good approximation, we can neglect the implicit ε' dependence of Z, χ, ϕ and λ, and restrict $\mathbf{k}$ and $\mathbf{k}'$ to the Fermi surface, so that the energy integral can be performed analytically [22],

$$\int_{-\infty}^{\infty} d\varepsilon' \, \mathbf{G}_{\mathbf{k}'}(\varepsilon', i\omega_{j'}) = -\pi \, \frac{i\omega_{j'} Z_{\mathbf{k}}(i\omega_{j'})\boldsymbol{\sigma}_0 + \phi_{\mathbf{k}}(i\omega_{j'})\boldsymbol{\sigma}_1}{\sqrt{\left[\omega_{j'} Z_{\mathbf{k}}(i\omega_{j'})\right]^2 + \phi_{\mathbf{k}}(i\omega_{j'})^2}} \ . \tag{A.13}$$

The $\boldsymbol{\sigma}_3$ coefficient of the self-energy given by χ vanishes automatically under this approximation when performing the integral. Moreover, the choice of gauge where $\bar{\phi} = 0$ has been made explicit[1].

In order to account for the Coulomb repulsion between electrons counteracting the effective phonon-mediated attraction, we follow the most regular practice and include the so-called Morel-Anderson pseudopotential parameter $\mu^*(\omega_c)$ in the off-diagonal component of the self-energy, where ω_c is a cutoff frequency of the order of 10 times the maximum phonon energy [163].

Finally, equating the $\boldsymbol{\sigma}$ coefficients in Eq. (A.6) with the ones obtained from Eqs. (A.10)–(A.13), we arrive at Eqs. (4.11)–(4.14) of the main text.

[1] See, for example, Ref. [22] p.37

Laburpena

Materia atomoz osaturik dago. Egoera solidoan, atomoen nukleoak posizio kristalografikoetan antolatzen dira, hauen arteko lotura elektroien bitartez gauzatzen delarik. Eskala mikroskopiko horretan gertatzen diren fenomeno fisikoak ulertzeko mekanika kuantikora jo behar dugu, eta, beraz, material jakin baten propietateak lehen printzipioetako kalkuluetatik (ingelesez *from first principles*) aurresatea, bere konfigurazio atomikotik abiatuz mekanika kuantikoak emandako ekuazioak ebaztean datza, beste parametro enpiriko gehigarririk erabili gabe.

Mekanika kuantikoaren baitan, elkarrekintzan dauden partikula askoz osatutako sistemak ulertzeko ebatzi behar diren problema fisikoak gorputz anitzeko problema (ingelesez *many-body problem*) bezala ezagutzen dira. Material lagin makroskopiko bat osatzen duen atomo kopurua izugarri handia — 10^{23} ingurukoa — izanik, lehen printzipioetako kalkuluak gorputz anitzeko problemen adibiderik garbienetakoak dira.

Mota honetako problemak ebaztearen interes nagusia fenomeno emergenteak ulertzean dago, sistema osatzen duten elementu isolatuen ezagutzatik soilik ondorioztatu ezin daitezkeenak. Adibidez, atomo isolatu baten erabateko ezagutzatik abiatuta ere, ezin izango genituzke materialetan gertatzen diren nukleoen bibrazio kolektiboak (fonoiak, ingelesez *phonons*) ondorioztatu, haien arteko elkarrekintzak kontuan hartuko ez bagenitu.

Era berean, elektroien propietateak nabarmen eraldatzen dira materialen baitan, nukleoen eta beste elektroien bitartez jasandako elkarrekintzen ondorioz. Izan ere, elektroien eta nukleoen bibrazioen arteko elkarrekintzak, hau da, elektroi-fonoi elkarrekintzak (ingelesez *electron-phonon interaction*), materialen propietate elektroniko ugari baldintzatzen ditu, hala nola metalen konduktibitatea, erdieroaleen xurgatze optikoa, edota supereroaleen trantsizio tenperatura.

Elektroi-fonoi elkarrekintzarekin lotutako lehen ikerketak metalen erresistibitate elektrikoarentzat teoria kuantiko bat garatzeko motibazioarekin landu ziren 30eko hamarkadan. Supereroankortasunaren jatorria topatzeko esfortzuek, halaber, eremuen teoria kuantikoan jorratutako kontzeptu eta teknikak egoera solidoaren fisikara egokitzea ekarri zuten 50eko hamarkadan. Hauen bitartez, elektroi-fonoi elkarrekintza barneratzen zuen formalismo matematikoa guztiz garatua zegoen 60eko hamarkadaren amaierarako. Hala

ere, garai hartako baldintza teknikoek eredu sinpleetara mugatzen zuten formalismo honen aplikazioa, eta era honetara hainbat fenomeno fisiko kualitatiboki ulertzea lortu zen arren — ohiko supereroankortasuna azaltzen duen BCS teoria kasu —, material espezifikoen propietateak kuantitatiboki aurresatea ezinezkoa zen.

60eko hamarkadan garatutako dentsitate funtzionalaren teoria (ingelesez *Density Functional Theory, DFT*) aurrerapauso handia izan zen eredu sinpleetatik haratago joan eta kalkulu errealistagoetara hurbiltze aldera, materialen gorputz anitzeko problema ordenagailuan ebatzi daitezkeen algoritmo numeriko moduan berridaztea erraztu baitzuen. Azken urteotan jasan ditugun aurrerapen teknologiko itzelei esker, DFT-ren aplikazio praktikoan laguntzen duten hainbat eta hainbat garapen metodologikoekin batera, gaur egun posible dugu material konplexuen propietate asko zehaztasun atomistikoarekin aurresatea. Izan ere, helburu honekin sortutako software desberdin asko garatu dira dagoeneko, eta errendimendu handiko konputazio zentroetan egin daitezkeen software hauen erabilera masiboak izugarrizko datu base digitalak sortzea ahalbidetzen ari da. Praktika honen anbiziorik handiena oraindik ezagutzen ez ditugun material berri interesgarriak diseinatzeko gaitasuna izatea da, ordenagailuan bere propietateak aztertu eta gero laborategian sintetizatu zitezkeenak.

Badira, hala ere, DFT-ren aplikazio mugetatik kanpo geratzen diren hainbat fenomeno fisiko. Funtsean, DFT oinarrizko egoerako teoria bat da, eta, beraz, elektroien egoera kitzikatuekin lotutako propietateak aurresateko — hala nola garraio elektrikoa edo xurgatze optikoa — oinarrizko zailtasunak ditu. Hauetarako, lehen aipatutako eremu kuantikoen teoriatik ekarritako ideiak dira erabili beharrekoak, zeintzuk, bestalde, konplexutasun tekniko eta konputazional izugarria dakartzaten kalkulu atomistikoetara aplikatzerakoan. Teoria hauen inplementazio numerikoa erraztuko luketen metodo konputazionalak garatzeak, beraz, aurresan ditzakegun propietate-sorta izugarri zabalduko zuen. Gainera, orain arte eredu sinpleetatik ondorioztatutako fenomeno fisiko interesgarriak errealitatera ekartzea ahalbidetuko lukete, material konkretuetan aurreikuspen kuantitatiboak eginez.

Tesi honetan, elektroi-fonoi elkarrekintzarekin lotutako hainbat propietate aurresateko metodo konputazionalak garatu ditugu, gorputz anitzeko teoria kuantikoak lehen printzipioetan oinarritutako kalkuluetan aplikatzea ahalbidetzen dituztenak. Kasu batzuetan, lehendik proposatutako metodo-ak orokortu ditugu haien jatorrizko aplikagarritasun eremua zabalduz. Beste batzuetan, aldiz, egungo metodoekin konparatuz efizientzia konputazionalean hobekuntza handiak ekartzen dituzten prozedura alternatiboak garatu ditugu. Gainera, garatutako metodo orokorrak material konkretuetan kalkuluak egiteko erabili ditugu, propietate ezberdinen azalpen teorikoa lortuz, eta kasuren batean propietate fisiko berriak iragarriz.

Erantzun elektronikoa eta plasmoiak spin-orbitadun gainazaletan

Material jakin bat kanpo-eremu batekin perturbatzean, materialeko elektroiek era kolektiboan erantzuten dute. Adibidez, kanpo-potentzial elektrostatiko bati erantzuteko, elektroien dentsitatea berrantolatuko da. Kanpo potentziala txikia bada, elektroi dentsitatearen aldaketaren eta kanpo potentzialaren artean erlazio lineal bat ezarri daiteke, eta bi kantitate hauek erlazionatzen dituen funtzioari erantzun funtzioa deitzen zaio. Erantzun funtzioen kalkuluak esperimentu askoren interpretazio teorikoa lortzen lagundu dezake, teorikoki egindako aurreikuspenak neurketetatik lortutako emaitzekin zuzenean konparatzea ahalbidetzen baitu. Materialen propietateak aztertzeko erabili daitezkeen kanpo perturbazioen artean, X izpiak edo neutroi sortak dira adibide ezagun batzuk. Kanpo-perturbazioaren maiztasunaren arabera sistema elektronikoaren erantzuna aldatuko da, eta, beraz, erantzun funtzioa orokorrean maiztasunaren funtzioa izango da. Neurketa esperimentaletan aztarna garbienak erresonantzia maiztasunetan topatzen dira. Maiztasun hauetan, elektroi gasak plasmoi (ingelesez *plasmon*) izeneko kitzikapen kolektibo bat jasaten du, elektroien karga-dentsitatean uhin bat dakarrena.

Bada, bestalde, elektroientzat kanpo-perturbaziotzat ulertu daitekeen baina materialetan intrintsekoki gertatzen den efektu bat ere: nukleoen bibrazioek eragindako potentzial elektrostatikoaren aldaketa. Nukleoak haien oreka posiziotik mugitzean, jatorrizko potentzial kristalinoa apur bat aldatuko da, eta elektroiek erantzun egingo dute aldaketa hau pantailatzeko. Elektroi-fonoi elkarrekintza aztertzean, beraz, erantzun funtzioak emandako pantailatze hau modu egokian barneratzeak berebiziko garrantzia izango du kalkulu teorikoen zehaztasunean.

Erantzun funtzioaren kalkulu konputazionala, tamalez, oso astuna da. Maiztasunean bereizmen handia lortzeko, erantzun kolektiboa emango duten elektroi trantsizioen mapa dentso bat behar da momentuen espazioan. Praktikan, honek trantsizio elektronikoekin lotutako matrize-elementu kopuru oso altu bat kalkulatzera behartzen gaitu, konputazio denbora izugarri handituz. Arazo hau nabarmenagoa egiten da bi dimentsioko sistemetan edota gainazaletan, non plasmoi kitzikapenaren frekuentzia oso baxua izan ohi den.

Zailtasun honi aurre egiteko helburuarekin, tesi honetako bigarren kapituluan, Wannier interpolazio teknikan oinarritutako prozedura konputazional bat garatu eta inplementatu dugu, erantzun funtzioen kalkuluan efizientzia-irabazi garrantzitsua dakarrena. Teknika honek Wannier funtzioen espazio-errealeko lokalizazioa eta Fourier-en transformatuaren propietateak erabiltzen ditu matrize-elementuen interpolaketa efizientea eta fidagarria lortzeko momentuen espazioan. Modu honetara, plasmoi kitzikapenen momentu eta maiztasunaren arteko dispertsio erlazioa zehaztasun handiarekin aurresan dezakegu kostu konputazional mugatuan.

Bada, gainera, gainazalen erantzun elektronikoa aztertzera bultzatzen gaituen motibazio berezi bat. Izan ere, solidoaren mugalde honetan hiru dimentsioko sistema arrunt gehienetan betetzen den simetria garrantzitsu bat apurtzen da, inbertsio-simetria hain zuzen ere. Honen ondorioz, solidoaren barnealdean endekatuta egon ohi diren aurkako spin-polarizazioa duten egoera elektronikoak banandu daitezke. Banantze honen magnitudea spin-orbita elkarrekintza (ingelesez *spin-orbit interaction*) izeneko efektu erlatibistak zehazten du. Gainazalaren egitura atomiko konkretuaren eraginez, gainera, gainazal-elektroien spin-polarizazio egitura konplexuak sortu daitezke momentuen espazioan, eredu sinpleekin ezin daitezkeenak deskribatu. Zentzu honetan, oso interesgarria suertatzen da elektroien spin-egitura konplexu honek erantzun elektronikoan duen eragina aztertzea. Orain arte ezinezkoa izan da efektu hau lehen printzipioetan oinarritutako erantzun funtzioaren kalkuluan barneratzea, lehen aipatutako zailtasun teknikoen ondorioz.

Tesi honen bigarren kapituluan, erantzun funtzioa kalkulatzeko garatu dugun metodo konputazional efizientea erabili dugu elektroien spin-polarizazio egitura konplexuak erantzun elektronikoan duen eragina aztertzeko. Bereziki, efektu erlatibista garrantzitsuak erakusten dituzten gainazalen plasmoi kitzikapenen azterketan zentratu gara, eta Tl/Si(111) sistema erabili dugu kalkulu konkretuak burutzeko adibide bezala. Lortutako emaitzetatik ondorio garrantzitsuak atera ditugu. Izan ere, gure kalkuluek erakusten dutenez, spin-orbita elkarrekintza handidun gainazaletan, plasmoi kitzikapenak kargadentsitate oszilazioez gain, spin-dentsitate oszilazioak ere dakartzate. Kitzikapen berri honi akoplatutako spin-karga plasmoia deitu diogu (ingelesez *coupled spin-charge plasmon*), eta bere momentu-energia dispertsioaren eta karga eta spin dentsitate oszilazioen balio konkretuak Tl/Si(111) gainazalean aurresan ditugun arren, gure lehen printzipioetako prozedurak fenomeno orokorra dela erakusten du. Aurkikuntza honek ondorio garrantzitsuak dakartza elektroi-fonoi elkarrekintzarentzat ere: fonoiek eragindako karga potentzial aldaketak, akoplatutako spin-karga erantzunaren ondorioz, eremu magnetiko bat sortuko du spin-orbitadun gainazaletan. Eremu magnetiko honek elektroi-fonoi elkarrekintza gauzatzeko kanal berriak zabaltzen ditu, elektroien spin-polarizazio egoeraren menpekoak izango direnak. Efektu hau tesi honetan aztertu ez den arren, etorkizunerako lerro oso interesgarri bat zabaltzen du.

Kuasipartikulen birnormalizazioa elektroi-fonoi elkarrekintzaren bitartez

Elektroien propietateak, hala nola abiadura edo masa, aldatu egiten dira hau solidoan zehar hedatzean, ingurunearekin duen elkarrekintzen eraginez. Gorputz-anitzeko teoria kuantikoaren baitan, eraldaketa honi birnormalizazio (ingelesez *renormalization*) deritzo. Birnormalizatutako elektroi honekin lotutako propietate fisikoak eta esperimentuetan uzten dituen aztarnak ik-

ertzerako orduan, hala ere, nolabaiteko partikula izaera antzeman daiteke, eta beraz kuasipartikula (ingelesez *quasiparticle*) bezala sailkatzen da.

Kuasipartikulen propietate bereizgarri nagusienetako bat haien bizidenbora da. Material batean elektroi bat kitzikatzerakoan, adibidez, denbora bat igaro ostean probabilitate jakin bat izango du bere energia ingurunearekin trukatu eta oinarrizko egoerara itzultzeko. Energia-trukatze prozesu hori gertatzeko igaro beharreko batazbesteko denbora elektroi kuasipartikula horren bizidenbora bezala ezagutzen da.

Elektroiek ingurunearekin izan ditzakeen elkarrekintzen artean, elektroi-fonoi elkarrekintza da nagusienetakoa. Kitzikatutako elektroiaren energia fonoiaren energia baino altuagoa bada, elektroi-fonoi matrize-elementuek zehaztutako probabilitate jakin bat izango du sisteman fonoi bat kitzikatu eta bere energia galtzeko. Elektroiaren energia fonoiarena baino baxuagoa bada ere, mekanika kuantikoak, beste mota bateko elkarrekintza bat ahalbidetzen du, zeinetan elektroiak birtualki fonoiak kitzikatu eta xurgatu ditzakeen, bere inguruan elkarrekintza-hodi bat sortuz. Elkarrekintza honen eraginez, elektroiaren abiadura jaisten da, eta bere masa efektiboa igo. Honek elektroiaren energia-momentu dispertsio erlazioan, hau da, banda egituran, aztarna garbiak uzten ditu, esperimentalki neurtu daitezkeenak.

Kuasipartikulak definitu eta aztertzeko esparru teoriko egokia eremuen teoria kuantikoaren testuinguruan garatutako Green-en funtzioen formalismoa da. Matematikoki, kuasipartikula baten energia eta bizidenbora, kuasipartikula horri dagokion Green-en funtzioaren polo konplexu batek plano konplexuan duen kokapenak zehazten du: ardatz errealeko posizioak kuasipartikularen energia emango digu, eta ardatz irudikariko posizioak bere bizidenbora.

Elektroi-fonoi elkarrekintzapean dagoen elektroi kuasipartikula bati dagokion Green-en funtzioa lehen printzipioetatik kalkulatzeko prozedura ezberdinak garatu dira azken urteotan. Izan ere, arrakasta handia erakutsi dute material konplexuen espektro elektronikoa aurresaterakoan, neurketa esperimentalekin konparaketa oso onak lortuz. Hala ere, prozedura hauek energia errealetan bakarrik lan egiteko daude prestatuta, eta beraz kuasipartikulen energia konplexu eta bizidenbora era hurbilduan bakarrik eman dezakete. Limitazio honek, beraz, esperimentuen interpretazio fisiko egoki bat lortzea ekiditzen du.

Tesi honen hirugarren kapituluan, metodo numeriko bat garatu dugu Green-en funtzioaren kontinuazio analitikoaren bitartez kuasipartikula energiak plano konplexu osoan topatzeko. Hemen garatutako prozedurak aurretik proposatutako metodo bat orokortzen du, elektroi-fonoi elkarrekintza prozesu konplexuen bitartez bai eta beste gorputz anitzeko elkarrekintzen bitartez birnormalizatutako kuasipartikulak aztertzea ahalbidetzen duena.

Kapituluaren lehenengo atalean, metodoaren funtsa xehetasun handiz deskribatzen da, eredu sinpleetatik hasi eta amaierako adierazpen orokorretara iritsi arte. Bigarren atalean, garatutako prozedura praktikan jartzen

da material konkretu baten kuasipartikulen banda egitura konplexua kalkulatzeko, atomo geruza bakarreko MoS2 sistemarena hain zuzen ere. Material honetan orain dela gutxi egin den esperimentu batek, elektroi-fonoi elkarrekintzak eragindako aztarna oso bitxiak neurtu ditu elektroien banda egituran. Tesi honetan garatutako prozedura orokorra erabiliz, aztarna horiek sakonki birnormalizatutako baina bizidenbora luzedun elektroi kuasipartikula berezietatik datozela erakusten dugu.

Kapituluaren azken atalean, kuasipartikulen espazio-errealeko egitura aztertzeko prozedura bat garatze aldera emandako lehen pausuak deskribatzen dira. Bereziki, elektroi-fonoi elkarrekintzaren bitartez inguruko atomoak desplazatu eta espazioko zonalde batean lokalizatzen diren elektroiak aztertzen dira, polaroi (ingelesez *polaron*) deituriko kuasipartikulak hain zuzen ere. Lortutako aurretiazko emaitzak oso itxaropentsuak dira lehen printzipioteako kalkuluetan oinarritutako polaroien teoria kuantiko bat garatze aldera.

Fermiren gainazaleko harmonikoen oinarria elektroi-fonoi elkarrekintzarekin loturiko problemak ebazteko

Pauliren esklusio printzipioari jarraituz, solidoetako elektroiek energia eta momentu jakin batekin etiketatu daitezkeen egoera kuantikoak betetzen dituzte. Egitura atomikoaren arabera, onartutako energia mailek momentuarekiko duten menpekotasuna aldatuko da, material bakoitzari dagokion banda egitura sortuz. Erdieroaletan, elektroiek banda osoak betetzen dituzte, libre dagoen ondorengo bandarekin energia-tarte (ingelesez gap) finitu bat lagaz. Metaletan, aldiz, gutxienez banda bat guztiz bete gabe geratzen da. Betetako egoera elektroniko energetikoenek Fermiren energia markatzen dute, eta momentuen espazioan beteta eta libre dauden egoera elektronikoak banatzen dituen gainazalak Fermiren gainazala definitzen du.

Elektroi bat bere oinarrizko egoeratik kitzikatzerakoan, hala nola kanpoeremu bat aplikatuz edo tenperatura finituaren eraginez, hutsik dagoen egoera batera bakarrik joan daiteke, eta, beraz, energia baxuko kitzikapen elektronikoak Fermiren gainazalaren ingurura mugatuta daude. Arrazoi honegatik, metal bakoitzari dagokion Fermiren gainazalaren forma eta topologia, bai eta gainazal honen inguruan elektroiek jasaten dituzten sakabanaketa prozesuak ezagutzea berebizikoa da bere garraio propietateak ulertzeko.

Fonoien energia oso txikia da (meV eskalakoa) elektroien energiekin konparatuz (eV eskalakoa). Horregatik, elektroi-fonoi sakabanatze prozesuak, Fermiren gainazalaren ingurura mugatuta daude, eta, beraz, papera oso garrantzitsua jokatzen dute metalen garraio propietateetan. Honen adibide interesgarri bat da ohiko supereroankortasuna, zeinetan Fermiren gainazalaren inguruko elektroiak Cooper pareetan lotzen diren fonoien bitartez gauzatutako erakarpen-elkarrekintzaren ondorioz.

Elektroi-fonoi elkarrekintza Fermiren gainazalaren ingurura mugatze honek, arazo tekniko bat dakar kalkulu praktikoen ikuspuntutik. Izan ere, momentuen espazioa numerikoki adierazteko modurik ohikoena sare homogeneoetan diskretizatzea da. Beraz, Fermiren gainazalaren inguruan puntu asko izateko, sekulako sare dentsoak erabili behar dira. Sare dentso hau osatzen duten puntuetatik, Fermiren energiatik gertu dauden egoera elektronikoak dituzten puntuak bakarrik erabiliko dira elektroi-fonoi sakabanaketa prozesuak aztertzeko. Esperientziak erakutsi du elektroi-fonoi elkarrekintza ondo barneratzen duten garraio-propietateen kalkulu konbergituak lortzeko 105 puntu inguru behar direla Fermiren gainazalaren inguruan. Horregatik, mota honetako kalkuluak oso pisutsuak dira konputazionalki, gaur egun superordenagailu zentroetan bakarrik burutu ahal direnak.

Tesi honetako hirugarren kapituluan, arazo hau konpontzeko ahalmena duen prozedura numeriko bat garatzen dugu, Fermiren gainazaleko harmonikoen oinarrian zentratua dagoena. Fermiren gainazalean ortonormala den oinarri bat erabiltzeko ideia Allenek 70eko hamarkadan planteatu zuen, garraio eta supereroankortasuna deskribatzeko ekuazioak oinarri honetan berridazteak sinplifikazio itzela ekarriko zuela iragarriz. Hala ere, berak planteatutako oinarri konkretua ezin izan da inoiz praktikara eraman, hainbat zailtasun teknikoen ondorioz. Honi aurre egiteko, Eiguren eta Gurtubayk oinarri berri bat proposatu zuten, eta hau lortzeko prozedura numerikoa garatu zuten, zeinetan triangulatutako Fermiren gainazal bat eraiki behar den aurretiazko urrats gisa. Tesi honetan, hobekuntza garrantzitsuak inplementatu ditugu triangulatutako Fermiren gainazala lortzeko prozeduran, kristalaren simetriak guztiz barneratzeko ahalmena ematen duena. Honi esker, Fermiren gainazaleko harmoniko simetrikoak eraiki ditzakegu, zeintzuen menpe Fermiren gainazalean definituta dauden propietate fisiko gehienak berridatzi daitezkeen. Kapituluaren hasieran, garatutako prozedura xehetasun handiarekin deskribatzen dugu, edozein simetriadun kristaletara aplikatu daitekeela erakutsiz, eta Fermiren gainazaleko harmoniko simetrikoen propietate orokorrak azalduz.

Kapituluaren bigarren zatian, Fermiren gainazaleko harmonikoen lehenengo aplikazio praktikoa erakusten dugu elektroi-fonoi elkarrekintzarekin loturiko problemak ebazteko. Honetarako aukeratu dugun problema fonoien bitartez gauzatutako supereroankortasuna izan da. Fenomeno hau gorputz anitzeko teoria kuantikoaren baitan azaltzen duten Eliashbergen ekuazioak berridatzi ditugu Fermiren gainazaleko harmonikoen oinarrian, eta hauek ebazteko kode konputazional bat inplementatu dugu. Honela, ekuazio hauek harmoniko simetriko oso gutxirekin zehaztasun handiz ebatzi daitezkeela egiaztatzen dugu, metodo konbentzionalekiko efizientzia-irabazia magnitude ordenetakoa izanik. Kapitulu honetan deskribatutako emaitzek metodo honen potentzial itzela erakusten dute, Fermiren gainazalean definitutako beste hainbat problema ebazteko tresna oso baliogarria izan daitekeela baieztatuz.

List of publications

Part of the work presented in this thesis has been published in the following references:

1. *Relativistic response and novel spin-charge plasmon at the Tl/Si(111) surface*,
   Jon Lafuente-Bartolome, Idoia G. Gurtubay, and Asier Eiguren,
   Physical Review B 96, 035416 (2017)

2. *Long-living carriers in a strong electron-phonon interacting two-dimensional doped semiconductor*,
   Peio Garcia-Goiricelaya, Jon Lafuente-Bartolome, Idoia G. Gurtubay and Asier Eiguren,
   Communications Physics 2, 81 (2019)

3. *Symmetric Helmholtz Fermi surface harmonics for an optimal representation of anisotropic quantities on the Fermi surface: Application to the electron-phonon problem*,
   Jon Lafuente-Bartolome, Idoia G. Gurtubay and Asier Eiguren.
   Accepted for publication in **Physical Review B**

4. *Fully anisotropic superconductivity with few Helmholtz Fermi surface harmonics*,
   Jon Lafuente-Bartolome, Idoia G. Gurtubay and Asier Eiguren.
   Accepted for publication in **Physical Review B - Rapid Communications**

Acknowledgments

It is with joy that I look back to the memories I keep from the years spent in Leioa during the course of my PhD. This is a happy ending for a long journey, which would not have been possible without the support of the many extraordinary people I am so lucky to have around me, to whom I owe my most sincere thanks.

First of all, I would like to express my deep gratitude to my supervisors Asier and Idoia. I clearly remember the day when I knocked your doors asking for a bachelor thesis project. Then I realize that if I am something of a scientist today, I owe it to you. For the confidence you have always put on me, and for the generosity with which you have shared your broad knowledge with me, I truly thank you.

I was lucky enough to join the Computational Theory in Condensed Matter Physics group when it had just taken off. The thrilling atmosphere created by all the members, and the exciting projects that are on the make, makes me foresee a bright future ahead. I would like to thank all of you for the lively discussions and for the valuable contributions to my thinking. Special thanks are due to Peio and Haritz, for all the endless debates at the office.

Whenever these debates have departed from the realm of the electron-phonon interactions, they have been spiced by the contributions of the different members of the Condensed Matter Physics and Applied Physics II departments at UPV/EHU, specially by my fellow pre-docs over the years: Xabi, Jon, Oscar, Mikel, Iñigo, Santos, Paul, Patricia, Leire and Telmo; you all have made the office a most pleasant workplace. A particular mention is deserved for Gose Naiz Taldea (GNT): Joanes, Asier, Iraultza, Iagoba, Julen, Iñigo, Mattin and the aforementioned Peio, Haritz, Xabi, Telmo and Oscar; for giving the daily routines the importance they merit, and for making the lunch time an oasis in the hardest days.

Outside Leioa, I would like to thank Feliciano Giustino for kindly welcoming me into his newly formed group at the University of Texas at Austin where I felt at home, and for all the enlightening discussions.

Apart from UPV/EHU, I would like to acknowledge the Donostia International Physics Center (DIPC) for financial support at the initial and final stages of my PhD, and for the computational resources.

The last words of gratitude go to the closest and most important ones. Eskerrik asko kuadrila, momentu on eta txarretan beti alboan egoteagatik. Gracias a mis padres y a mi hermano, por todo el amor y consejo que me habéis dado. Y por último gracias a ti, Marta, por escucharme, y por mantenerme siempre con el ánimo alto y los pies en el suelo. Esta tesis te la dedico a ti.

Bibliography

[1] J. M. Ziman, *Electrons and Phonons: The Theory of Transport Phenomena in Solids*. Clarendon Press, Oxford, 1960.

[2] G. Grimvall, *The Electron-Phonon Interaction in Metals*. North-Holland, Amsterdam, 1981.

[3] A. B. Migdal, *"Interaction between electrons and lattice vibrations in a normal metal"*, Sov. Phys. JETP **7**, 996–1001 (1958).

[4] G. Baym, *"Field-theoretic approach to the properties of the solid state"*, Annals of Physics **14**, 1 - 42 (1961).

[5] S. Engelsberg and J. R. Schrieffer, *"Coupled Electron-Phonon System"*, Phys. Rev. **131**, 993–1008 (1963).

[6] L. Hedin and S. Lundqvist, *"Effects of Electron-Electron and Electron-Phonon Interactions on the One-Electron States of Solids"*, in *Solid State Physics*, F. Seitz, D. Turnbull, and H. Ehrenreich, eds., volume 23 of *Solid State Physics*, pp. 1 – 181. Academic Press, New York, 1970.

[7] F. Giustino, *"Electron-phonon interactions from first principles"*, Rev. Mod. Phys. **89**, 015003 (2017).

[8] S. Baroni, S. de Gironcoli, A. Dal Corso, and P. Giannozzi, *"Phonons and related crystal properties from density-functional perturbation theory"*, Rev. Mod. Phys. **73**, 515–562 (2001).

[9] F. Giustino, M. L. Cohen, and S. G. Louie, *"Electron-phonon interaction using Wannier functions"*, Phys. Rev. B **76**, 165108 (2007).

[10] A. Eiguren and C. Ambrosch-Draxl, *"Wannier interpolation scheme for phonon-induced potentials: Application to bulk MgB_2, W, and the (1×1) H-covered W(110) surface"*, Phys. Rev. B **78**, 045124 (2008).

[11] M. Calandra, G. Profeta, and F. Mauri, *"Adiabatic and nonadiabatic phonon dispersion in a Wannier function approach"*, Phys. Rev. B **82**, 165111 (2010).

[12] A. Eiguren, S. de Gironcoli, E. V. Chulkov, P. M. Echenique, and E. Tosatti, *"Electron-Phonon Interaction at the Be(0001) Surface"*, Phys. Rev. Lett. **91**, 166803 (2003).

[13] C. Verdi, F. Caruso, and F. Giustino, *"Origin of the crossover from polarons to Fermi liquids in transition metal oxides"*, Nature Communications **8**, 15769 (2017).

[14] P. Garcia-Goiricelaya, J. Lafuente-Bartolome, I. G. Gurtubay, and A. Eiguren, *"Long-living carriers in a strong electron-phonon interacting two-dimensional doped semiconductor"*, Communications Physics **2**, 81 (2019).

[15] A. M. Saitta, M. Lazzeri, M. Calandra, and F. Mauri, *"Giant Nonadiabatic Effects in Layer Metals: Raman Spectra of Intercalated Graphite Explained"*, Phys. Rev. Lett. **100**, 226401 (2008).

[16] F. Caruso, M. Hoesch, P. Achatz, J. Serrano, M. Krisch, E. Bustarret, and F. Giustino, *"Nonadiabatic Kohn Anomaly in Heavily Boron-Doped Diamond"*, Phys. Rev. Lett. **119**, 017001 (2017).

[17] D. Novko, *"Nonadiabatic coupling effects in MgB_2 reexamined"*, Phys. Rev. B **98**, 041112(R) (2018).

[18] P. Garcia-Goiricelaya, J. Lafuente-Bartolome, I. G. Gurtubay, and A. Eiguren, *"Emergence of large nonadiabatic effects induced by the electron-phonon interaction on the complex vibrational quasiparticle spectrum of doped monolayer MoS_2"*, Phys. Rev. B **101**, 054304 (2020).

[19] H. J. Choi, D. Roundy, H. Sun, M. L. Cohen, and S. G. Louie, *"The origin of the anomalous superconducting properties of MgB2"*, Nature **418**, 758-760 (2002).

[20] E. R. Margine and F. Giustino, *"Anisotropic Migdal-Eliashberg theory using Wannier functions"*, Phys. Rev. B **87**, 024505 (2013).

[21] J. R. Schrieffer, *Theory of superconductivity*. W.A. Benjamin, New York, 1964.

[22] P. B. Allen and B. Mitrovic, *"Theory of Superconducting T_c"*, in *Solid State Physics*, F. Seitz, D. Turnbull, and H. Ehrenreich, eds., volume 37, pp. 1–92. Academic Press, New York, 1983.

[23] A. Fetter and J. Walecka, *Quantum theory of many-particle systems*. Dover Publications, New York, 2003.

[24] J. Schwinger, *"On the Green's functions of quantized fields. I"*, Proceedings of the National Academy of Sciences **37**, 452–455 (1951).

[25] L. Hedin, *"New Method for Calculating the One-Particle Green's Function with Application to the Electron-Gas Problem"*, Phys. Rev. **139**, A796–A823 (1965).

[26] E. G. Maksimov, *"A self-consistent description of the electron-phonon system in metals and the problem of lattice stability"*, Sov. Phys. JETP **42**, 1138 (1976).

[27] G. Mahan, *Many-Particle Physics*. Physics of Solids and Liquids. Springer US, New York, 2000.

[28] M. S. Hybertsen and S. G. Louie, *"Electron correlation in semiconductors and insulators: Band gaps and quasiparticle energies"*, Phys. Rev. B **34**, 5390–5413 (1986).

[29] F. Aryasetiawan and O. Gunnarsson, *"The GW method"*, Reports on Progress in Physics **61**, 237–312 (1998).

[30] D. Golze, M. Dvorak, and P. Rinke, *"The GW Compendium: A Practical Guide to Theoretical Photoemission Spectroscopy"*, Frontiers in Chemistry **7**, 377 (2019).

[31] P. Hohenberg and W. Kohn, *"Inhomogeneous Electron Gas"*, Phys. Rev. **136**, B864–B871 (1964).

[32] W. Kohn and L. J. Sham, *"Self-Consistent Equations Including Exchange and Correlation Effects"*, Phys. Rev. **140**, A1133–A1138 (1965).

[33] J. Bardeen, *"Conductivity of Monovalent Metals"*, Phys. Rev. **52**, 688–697 (1937).

[34] H. Fröhlich, *"Electrons in lattice fields"*, Advances in Physics **3**, 325-361 (1954).

[35] T. Holstein, *"Studies of polaron motion: Part I. The molecular-crystal model"*, Annals of Physics **8**, 325 - 342 (1959).

[36] R. Parr and W. Yang, *Density-Functional Theory of Atoms and Molecules*. Oxford University Press, New York, 1989.

[37] R. M. Martin, *Electronic Structure: Basic Theory and Practical Methods*. Cambridge University Press, Cambridge, 2004.

[38] D. Singh and L. Nordstrom, *Planewaves, Pseudopotentials, and the LAPW Method*. Springer US, New York, 2006.

[39] N. Ashcroft and N. Mermin, *Solid State Physics*. Harcourt College Publishers, New York, 1976.

[40] F. Marsiglio, M. Schossmann, and J. P. Carbotte, *"Iterative analytic continuation of the electron self-energy to the real axis"*, Phys. Rev. B **37**, 4965–4969 (1988).

[41] I. Žutić, J. Fabian, and S. Das Sarma, *"Spintronics: Fundamentals and applications"*, Rev. Mod. Phys. **76**, 323–410 (2004).

[42] G. A. Prinz, *"Magnetoelectronics"*, Science **282**, 1660–1663 (1998).

[43] G. Bihlmayer, O. Rader, and R. Winkler, *"Focus on the Rashba effect"*, New Journal of Physics **17**, 050202 (2015).

[44] A. Manchon, H. C. Koo, J. Nitta, S. M. Frolov, and R. A. Duine, *"New perspectives for Rashba spin–orbit coupling"*, Nature Materials **14**, 871-882 (2015).

[45] E. Runge and E. K. U. Gross, *"Density-Functional Theory for Time-Dependent Systems"*, Phys. Rev. Lett. **52**, 997–1000 (1984).

[46] M. Petersilka, U. J. Gossmann, and E. K. U. Gross, *"Excitation Energies from Time-Dependent Density-Functional Theory"*, Phys. Rev. Lett. **76**, 1212–1215 (1996).

[47] M. Marques, A. Rubio, E. K. Gross, K. Burke, F. Nogueira, and C. A. Ullrich, *Time-dependent density functional theory*. Springer-Verlag Berlin Heidelberg, 2006.

[48] J. P. Perdew and Y. Wang, *"Accurate and simple analytic representation of the electron-gas correlation energy"*, Phys. Rev. B **45**, 13244–13249 (1992).

[49] S. L. Adler, *"Quantum Theory of the Dielectric Constant in Real Solids"*, Phys. Rev. **126**, 413–420 (1962).

[50] N. Wiser, *"Dielectric Constant with Local Field Effects Included"*, Phys. Rev. **129**, 62–69 (1963).

[51] I. G. Gurtubay, J. M. Pitarke, W. Ku, A. G. Eguiluz, B. C. Larson, J. Tischler, P. Zschack, and K. D. Finkelstein, *"Electron-hole and plasmon excitations in 3d transition metals: Ab initio calculations and inelastic x-ray scattering measurements"*, Phys. Rev. B **72**, 125117 (2005).

[52] U. von Barth and L. Hedin, *"A local exchange-correlation potential for the spin polarized case. I"*, Journal of Physics C: Solid State Physics **5**, 1629 (1972).

[53] K. Andersen, K. W. Jacobsen, and K. S. Thygesen, *"Spatially resolved quantum plasmon modes in metallic nano-films from first-principles"*, Phys. Rev. B **86**, 245129 (2012).

[54] J. M. Pitarke, V. M. Silkin, E. V. Chulkov, and P. M. Echenique, *"Theory of surface plasmons and surface-plasmon polaritons"*, Reports on Progress in Physics **70**, 1–87 (2006).

[55] G. H. Wannier, *"The Structure of Electronic Excitation Levels in Insulating Crystals"*, Phys. Rev. **52**, 191–197 (1937).

[56] N. Marzari and D. Vanderbilt, *"Maximally localized generalized Wannier functions for composite energy bands"*, Phys. Rev. B **56**, 12847–12865 (1997).

[57] I. Souza, N. Marzari, and D. Vanderbilt, *"Maximally localized Wannier functions for entangled energy bands"*, Phys. Rev. B **65**, 035109 (2001).

[58] N. Marzari, A. A. Mostofi, J. R. Yates, I. Souza, and D. Vanderbilt, *"Maximally localized Wannier functions: Theory and applications"*, Rev. Mod. Phys. **84**, 1419–1475 (2012).

[59] J. R. Yates, X. Wang, D. Vanderbilt, and I. Souza, *"Spectral and Fermi surface properties from Wannier interpolation"*, Phys. Rev. B **75**, 195121 (2007).

[60] S. LaShell, B. A. McDougall, and E. Jensen, *"Spin Splitting of an Au(111) Surface State Band Observed with Angle Resolved Photoelectron Spectroscopy"*, Phys. Rev. Lett. **77**, 3419–3422 (1996).

[61] Y. M. Koroteev, G. Bihlmayer, J. E. Gayone, E. V. Chulkov, S. Blügel, P. M. Echenique, and P. Hofmann, *"Strong Spin-Orbit Splitting on Bi Surfaces"*, Phys. Rev. Lett. **93**, 046403 (2004).

[62] P. Hofmann, J. E. Gayone, G. Bihlmayer, Y. M. Koroteev, and E. V. Chulkov, *"Electronic structure and Fermi surface of Bi(100)"*, Phys. Rev. B **71**, 195413 (2005).

[63] K. Sugawara, T. Sato, S. Souma, T. Takahashi, M. Arai, and T. Sasaki, *"Fermi Surface and Anisotropic Spin-Orbit Coupling of Sb(111) Studied by Angle-Resolved Photoemission Spectroscopy"*, Phys. Rev. Lett. **96**, 046411 (2006).

[64] I. Gierz, T. Suzuki, E. Frantzeskakis, S. Pons, S. Ostanin, A. Ernst, J. Henk, M. Grioni, K. Kern, and C. R. Ast, *"Silicon Surface with Giant Spin Splitting"*, Phys. Rev. Lett. **103**, 046803 (2009).

[65] S. Hatta, T. Aruga, Y. Ohtsubo, and H. Okuyama, *"Large Rashba spin splitting of surface resonance bands on semiconductor surface"*, Phys. Rev. B **80**, 113309 (2009).

[66] K. Yaji, Y. Ohtsubo, S. Hatta, H. Okuyama, K. Miyamoto, T. Okuda, A. Kimura, H. Namatame, M. Taniguchi, and T. Aruga, *"Large Rashba spin splitting of a metallic surface-state band on a semiconductor surface"*, Nature Communications **1**, 17 (2010).

[67] K. Sakamoto, T. Oda, A. Kimura, K. Miyamoto, M. Tsujikawa, A. Imai, N. Ueno, H. Namatame, M. Taniguchi, P. E. J. Eriksson, and R. I. G. Uhrberg, *"Abrupt Rotation of the Rashba Spin to the Direction Perpendicular to the Surface"*, Phys. Rev. Lett. **102**, 096805 (2009).

[68] A. Takayama, T. Sato, S. Souma, and T. Takahashi, *"Giant Out-of-Plane Spin Component and the Asymmetry of Spin Polarization in Surface Rashba States of Bismuth Thin Film"*, Phys. Rev. Lett. **106**, 166401 (2011).

[69] P. Höpfner, J. Schäfer, A. Fleszar, J. H. Dil, B. Slomski, F. Meier, C. Loho, C. Blumenstein, L. Patthey, W. Hanke, and R. Claessen, *"Three-Dimensional Spin Rotations at the Fermi Surface of a Strongly Spin-Orbit Coupled Surface System"*, Phys. Rev. Lett. **108**, 186801 (2012).

[70] A. Eiguren and C. Ambrosch-Draxl, *"Spin polarization and relativistic electronic structure of the* 1×1 *H/W(110) surface"*, New Journal of Physics **11**, 013056 (2009).

[71] A. Stróżecka, A. Eiguren, and J. I. Pascual, *"Quasiparticle Interference around a Magnetic Impurity on a Surface with Strong Spin-Orbit Coupling"*, Phys. Rev. Lett. **107**, 186805 (2011).

[72] J. Ibañez-Azpiroz, A. Eiguren, and A. Bergara, *"Relativistic effects and fully spin-polarized Fermi surface at the Tl/Si(111) surface"*, Phys. Rev. B **84**, 125435 (2011).

[73] D. V. Gruznev, L. V. Bondarenko, A. V. Matetskiy, A. A. Yakovlev, A. Y. Tupchaya, S. V. Eremeev, E. V. Chulkov, J.-P. Chou, C.-M. Wei, M.-Y. Lai, Y.-L. Wang, A. V. Zotov, and A. A. Saranin, *"A Strategy to Create Spin-Split Metallic Bands on Silicon Using a Dense Alloy Layer"*, Scientific Reports **4**, 4742 (2014).

[74] D. Y. Usachov, I. A. Nechaev, G. Poelchen, M. Güttler, E. E. Krasovskii, S. Schulz, A. Generalov, K. Kliemt, A. Kraiker, C. Krellner, K. Kummer, S. Danzenbächer, C. Laubschat, A. P. Weber, J. Sánchez-Barriga, E. V. Chulkov, A. F. Santander-Syro,

T. Imai, K. Miyamoto, T. Okuda, and D. V. Vyalikh, *"Cubic Rashba Effect in the Surface Spin Structure of Rare-Earth Ternary Materials"*, Phys. Rev. Lett. **124**, 237202 (2020).

[75] S. D. Stolwijk, A. B. Schmidt, M. Donath, K. Sakamoto, and P. Krüger, *"Rotating Spin and Giant Splitting: Unoccupied Surface Electronic Structure of* Tl/Si(111)*"*, Phys. Rev. Lett. **111**, 176402 (2013).

[76] K. Sakamoto, T.-H. Kim, T. Kuzumaki, B. Müller, Y. Yamamoto, M. Ohtaka, J. R. Osiecki, K. Miyamoto, Y. Takeichi, A. Harasawa, S. D. Stolwijk, A. B. Schmidt, J. Fujii, R. I. G. Uhrberg, M. Donath, H. W. Yeom, and T. Oda, *"Valley spin polarization by using the extraordinary Rashba effect on silicon"*, Nature Communications **4**, 2073 (2013).

[77] S. D. Stolwijk, A. B. Schmidt, K. Sakamoto, P. Krüger, and M. Donath, *"Valley spin polarization of Tl/Si(111)"*, Phys. Rev. Materials **1**, 064604 (2017).

[78] P. Garcia-Goiricelaya, I. G. Gurtubay, and A. Eiguren, *"Coupled spin and electron-phonon interaction at the Tl/Si(111) surface from relativistic first-principles calculations"*, Phys. Rev. B **97**, 201405 (2018).

[79] http://elk.sourceforge.net/ .

[80] B. Rousseau, A. Eiguren, and A. Bergara, *"Efficient computation of magnon dispersions within time-dependent density functional theory using maximally localized Wannier functions"*, Phys. Rev. B **85**, 054305 (2012).

[81] S. Maiti, V. Zyuzin, and D. L. Maslov, *"Collective modes in two- and three-dimensional electron systems with Rashba spin-orbit coupling"*, Phys. Rev. B **91**, 035106 (2015).

[82] G. Giuliani and G. Vignale, *Quantum Theory of the Electron Liquid*. Cambridge University Press, Cambridge, 2005.

[83] C. A. Rozzi, D. Varsano, A. Marini, E. K. U. Gross, and A. Rubio, *"Exact Coulomb cutoff technique for supercell calculations"*, Phys. Rev. B **73**, 205119 (2006).

[84] T. Nagao, T. Hildebrandt, M. Henzler, and S. Hasegawa, *"Dispersion and Damping of a Two-Dimensional Plasmon in a Metallic Surface-State Band"*, Phys. Rev. Lett. **86**, 5747–5750 (2001).

[85] E. P. Rugeramigabo, T. Nagao, and H. Pfnür, *"Experimental investigation of two-dimensional plasmons in a $DySi_2$ monolayer on Si(111)"*, Phys. Rev. B **78**, 155402 (2008).

[86] L. D. Landau, *"The Theory of a Fermi Liquid"*, Sov. Phys. JETP **3**, 920–925 (1956).

[87] M. Kang, S. W. Jung, W. J. Shin, Y. Sohn, S. H. Ryu, T. K. Kim, M. Hoesch, and K. S. Kim, *"Holstein polaron in a valley-degenerate two-dimensional semiconductor"*, Nature Materials **17**, 676-680 (2018).

[88] A. Damascelli, Z. Hussain, and Z.-X. Shen, *"Angle-resolved photoemission studies of the cuprate superconductors"*, Rev. Mod. Phys. **75**, 473–541 (2003).

[89] B. Farid, *Ground and Low-Lying Excited States of Interacting Electron Systems. A Survey and Some Critical Analyses*, pp. 103–261. Imperial College Press, London, 1999.

[90] H. Lehmann, *"Über Eigenschaften von Ausbreitungsfunktionen und Renormierungskonstanten quantisierter Felder"*, Il Nuovo Cimento **11**, 342-357 (1954).

[91] G. Onida, L. Reining, and A. Rubio, *"Electronic excitations: density-functional versus many-body Green's-function approaches"*, Rev. Mod. Phys. **74**, 601–659 (2002).

[92] A. Eiguren and C. Ambrosch-Draxl, *"Complex Quasiparticle Band Structure Induced by Electron-Phonon Interaction: Band Splitting in the* 1×1H/W(110) *Surface"*, Phys. Rev. Lett. **101**, 036402 (2008).

[93] A. Eiguren, C. Ambrosch-Draxl, and P. M. Echenique, *"Self-consistently renormalized quasiparticles under the electron-phonon interaction"*, Phys. Rev. B **79**, 245103 (2009).

[94] E. Piatti, D. De Fazio, D. Daghero, S. R. Tamalampudi, D. Yoon, A. C. Ferrari, and R. S. Gonnelli, *"Multi-Valley Superconductivity in Ion-Gated MoS_2 Layers"*, Nano Letters **18**, 4821-4830 (2018).

[95] T. Sohier, E. Ponomarev, M. Gibertini, H. Berger, N. Marzari, N. Ubrig, and A. F. Morpurgo, *"Enhanced Electron-Phonon Interaction in Multivalley Materials"*, Phys. Rev. X **9**, 031019 (2019).

[96] D. Novko, *"Broken adiabaticity induced by Lifshitz transition in MoS_2 and WS_2 single layers"*, Communications Physics **3**, 30 (2020).

[97] W. Press, B. Flannery, S. Teukolsky, and W. Vetterling, *Numerical Recipes in FORTRAN 77: The Art of Scientific Computing*. Cambridge University Press, Cambridge, 1993.

[98] P. O. Scherer, *Computational Physics*. Springer-Verlag Berlin Heidelberg, 2010.

[99] A. S. Alexandrov and J. T. Devreese, *Advances in polaron physics*, volume 159. Springer-Verlag Berlin Heidelberg, 2010.

[100] D. Emin, *Polarons*. Cambridge University Press, Cambridge, 2012.

[101] J. T. Devreese, *"Fröhlich Polarons. Lecture course including detailed theoretical derivations – 9th edition"*, arXiv:1611.06122 .

[102] C. Franchini, G. Kresse, and R. Podloucky, *"Polaronic Hole Trapping in Doped* $BaBiO_3$*"*, Phys. Rev. Lett. **102**, 256402 (2009).

[103] S. Kokott, S. V. Levchenko, P. Rinke, and M. Scheffler, *"First-principles supercell calculations of small polarons with proper account for long-range polarization effects"*, New Journal of Physics **20**, 033023 (2018).

[104] K. Miyata, D. Meggiolaro, M. T. Trinh, P. P. Joshi, E. Mosconi, S. C. Jones, F. De Angelis, and X.-Y. Zhu, *"Large polarons in lead halide perovskites"*, Science Advances **3**, (2017).

[105] M. Reticcioli, U. Diebold, G. Kresse, and C. Franchini, *"Small Polarons in Transition Metal Oxides"*, in *Handbook of Materials Modeling: Applications: Current and Emerging Materials*, W. Andreoni and S. Yip, eds., pp. 1–39. Springer International Publishing, Cham, 2019.

[106] W. H. Sio, C. Verdi, S. Poncé, and F. Giustino, *"Polarons from First Principles, without Supercells"*, Phys. Rev. Lett. **122**, 246403 (2019).

[107] W. H. Sio, C. Verdi, S. Poncé, and F. Giustino, *"Ab initio theory of polarons: Formalism and applications"*, Phys. Rev. B **99**, 235139 (2019).

[108] S. Moser, L. Moreschini, J. Jaćimović, O. S. Barišić, H. Berger, A. Magrez, Y. J. Chang, K. S. Kim, A. Bostwick, E. Rotenberg, L. Forró, and M. Grioni, *"Tunable Polaronic Conduction in Anatase* TiO_2*"*, Phys. Rev. Lett. **110**, 196403 (2013).

[109] C. Chen, J. Avila, E. Frantzeskakis, A. Levy, and M. C. Asensio, *"Observation of a two-dimensional liquid of Fröhlich polarons at the bare* $SrTiO_3$ *surface"*, Nature Communications **6**, 8585 (2015).

[110] Z. Wang, S. McKeown Walker, A. Tamai, Y. Wang, Z. Ristic, F. Y. Bruno, A. de la Torre, S. Riccò, N. C. Plumb, M. Shi, P. Hlawenka, J. Sánchez-Barriga, A. Varykhalov, T. K. Kim, M. Hoesch, P. D. C.

King, W. Meevasana, U. Diebold, J. Mesot, B. Moritz, T. P. Devereaux, M. Radovic, and F. Baumberger, *"Tailoring the nature and strength of electron–phonon interactions in the $SrTiO_3$(001) 2D electron liquid"*, Nature Materials **15**, 835-839 (2016).

[111] C. Chen, J. Avila, S. Wang, Y. Wang, M. Mucha-Kruczyński, C. Shen, R. Yang, B. Nosarzewski, T. P. Devereaux, G. Zhang, and M. C. Asensio, *"Emergence of Interfacial Polarons from Electron–Phonon Coupling in Graphene/h-BN van der Waals Heterostructures"*, Nano Letters **18**, 1082-1087 (2018).

[112] J. M. Riley, F. Caruso, C. Verdi, L. B. Duffy, M. D. Watson, L. Bawden, K. Volckaert, G. van der Laan, T. Hesjedal, M. Hoesch, F. Giustino, and P. D. C. King, *"Crossover from lattice to plasmonic polarons of a spin-polarised electron gas in ferromagnetic EuO"*, Nature Communications **9**, 2305 (2018).

[113] N. S. Gillis, *"Self-Consistent Phonons and the Coupled Electron-Phonon System"*, Phys. Rev. B **1**, 1872–1876 (1970).

[114] M. Springford, *Electrons at the Fermi Surface*. Cambridge University Press, New York, 2011.

[115] J. I. Mustafa, M. Bernardi, J. B. Neaton, and S. G. Louie, *"Ab initio electronic relaxation times and transport in noble metals"*, Phys. Rev. B **94**, 155105 (2016).

[116] P. B. Allen, *"Fermi-surface harmonics: A general method for nonspherical problems. Application to Boltzmann and Eliashberg equations"*, Phys. Rev. B **13**, 1416–1427 (1976).

[117] R. Heid, K.-P. Bohnen, R. Zeyher, and D. Manske, *"Momentum Dependence of the Electron-Phonon Coupling and Self-Energy Effects in Superconducting* $YBa_2Cu_3O_7$ *within the Local Density Approximation"*, Phys. Rev. Lett. **100**, 137001 (2008).

[118] B. Xu and M. J. Verstraete, *"First Principles Explanation of the Positive Seebeck Coefficient of Lithium"*, Phys. Rev. Lett. **112**, 196603 (2014).

[119] A. Eiguren and I. G. Gurtubay, *"Helmholtz Fermi surface harmonics: an efficient approach for treating anisotropic problems involving Fermi surface integrals"*, New Journal of Physics **16**, 063014 (2014).

[120] P. E. Blöchl, O. Jepsen, and O. K. Andersen, *"Improved tetrahedron method for Brillouin-zone integrations"*, Phys. Rev. B **49**, 16223–16233 (1994).

[121] M. I. Aroyo, D. Orobengoa, G. de la Flor, E. S. Tasci, J. M. Perez-Mato, and H. Wondratschek, *"Brillouin-zone database on the Bilbao Crystallographic Server"*, Acta Crystallographica Section A **70**, 126-137 (2014).

[122] J. R. Shewchuk, *"Triangle: Engineering a 2D Quality Mesh Generator and Delaunay Triangulator"*, in *Applied Computational Geometry: Towards Geometric Engineering*, M. C. Lin and D. Manocha, eds., volume 1148 of *Lecture Notes in Computer Science*, pp. 203–222. Springer-Verlag, Berlin, 1996.

[123] H. Si, *"TetGen, a Delaunay-Based Quality Tetrahedral Mesh Generator"*, ACM Trans. Math. Softw. **41**, (2015).

[124] M. Botsch, L. Kobbelt, M. Pauly, P. Alliez, and B. Lévy, *Polygon mesh processing*. AK Peters/CRC Press, Boca Raton, 2010.

[125] G. Pizzi, V. Vitale, R. Arita, S. BlÃ$\frac{1}{4}$gel, F. Freimuth, G. Géranton, M. Gibertini, D. Gresch, C. Johnson, T. Koretsune, J. Ibañez-Azpiroz, H. Lee, J.-M. Lihm, D. Marchand, A. Marrazzo, Y. Mokrousov, J. I. Mustafa, Y. Nohara, Y. Nomura, L. Paulatto, S. Poncé, T. Ponweiser, J. Qiao, F. ThÃ¶le, S. S. Tsirkin, M. Wierzbowska, N. Marzari, D. Vanderbilt, I. Souza, A. A. Mostofi, and J. R. Yates, *"Wannier90 as a community code: new features and applications"*, Journal of Physics: Condensed Matter **32**, 165902 (2020).

[126] J. Bardeen, L. N. Cooper, and J. R. Schrieffer, *"Theory of Superconductivity"*, Phys. Rev. **108**, 1175–1204 (1957).

[127] W. H. Butler and P. B. Allen, *"Gap Anisotropy and Tc Enhancement: General Theory, and Calculations for Nb, using Fermi Surface Harmonics"*, in *Superconductivity in d- and f-Band Metals: Second Rochester Conference*, D. H. Douglass, ed., pp. 73–120. Springer US, Boston, MA, 1976.

[128] G. M. Eliashberg, *"Interactions between electrons and lattice vibrations in a superconductor"*, Sov. Phys. JETP **11**, 696–702 (1960).

[129] F. Marsiglio and J. P. Carbotte, *"Electron-Phonon Superconductivity"*, in *Superconductivity: Conventional and Unconventional Superconductors*, K. H. Bennemann and J. B. Ketterson, eds., pp. 73–162. Springer Verlag Berlin Heidelberg, 2008.

[130] D. J. Scalapino, J. R. Schrieffer, and J. W. Wilkins, *"Strong-Coupling Superconductivity. I"*, Phys. Rev. **148**, 263–279 (1966).

[131] C. Heil, S. Poncé, H. Lambert, M. Schlipf, E. R. Margine, and F. Giustino, *"Origin of Superconductivity and Latent Charge Density Wave in* NbS_2*"*, Phys. Rev. Lett. **119**, 087003 (2017).

[132] M. Kawamura, R. Akashi, and S. Tsuneyuki, *"Anisotropic superconducting gaps in* YNi_2B_2C*: A first-principles investigation"*, Phys. Rev. B **95**, 054506 (2017).

[133] J. Kortus, I. I. Mazin, K. D. Belashchenko, V. P. Antropov, and L. L. Boyer, *"Superconductivity of Metallic Boron in* MgB_2*"*, Phys. Rev. Lett. **86**, 4656–4659 (2001).

[134] A. Y. Liu, I. I. Mazin, and J. Kortus, *"Beyond Eliashberg Superconductivity in* MgB_2*: Anharmonicity, Two-Phonon Scattering, and Multiple Gaps"*, Phys. Rev. Lett. **87**, 087005 (2001).

[135] H. J. Choi, D. Roundy, H. Sun, M. L. Cohen, and S. G. Louie, *"First-principles calculation of the superconducting transition in* MgB_2 *within the anisotropic Eliashberg formalism"*, Phys. Rev. B **66**, 020513 (2002).

[136] P. Giannozzi, O. Andreussi, T. Brumme, O. Bunau, M. B. Nardelli, M. Calandra, R. Car, C. Cavazzoni, D. Ceresoli, M. Cococcioni, N. Colonna, I. Carnimeo, A. D. Corso, S. de Gironcoli, P. Delugas, R. A. D. Jr, A. Ferretti, A. Floris, G. Fratesi, G. Fugallo, R. Gebauer, U. Gerstmann, F. Giustino, T. Gorni, J. Jia, M. Kawamura, H.-Y. Ko, A. Kokalj, E. Küçükbenli, M. Lazzeri, M. Marsili, N. Marzari, F. Mauri, N. L. Nguyen, H.-V. Nguyen, A. O. de-la Roza, L. Paulatto, S. Poncé, D. Rocca, R. Sabatini, B. Santra, M. Schlipf, A. P. Seitsonen, A. Smogunov, I. Timrov, T. Thonhauser, P. Umari, N. Vast, X. Wu, and S. Baroni, *"Advanced capabilities for materials modelling with QUANTUM ESPRESSO"*, Journal of Physics: Condensed Matter **29**, 465901 (2017).

[137] J. P. Perdew and A. Zunger, *"Self-interaction correction to density-functional approximations for many-electron systems"*, Phys. Rev. B **23**, 5048–5079 (1981).

[138] J. Nagamatsu, N. Nakagawa, T. Muranaka, Y. Zenitani, and J. Akimitsu, *"Superconductivity at 39 K in magnesium diboride"*, Nature **410**, 63-64 (2001).

[139] W. L. McMillan, *"Transition Temperature of Strong-Coupled Superconductors"*, Phys. Rev. **167**, 331–344 (1968).

[140] P. B. Allen and R. C. Dynes, *"Transition temperature of strong-coupled superconductors reanalyzed"*, Phys. Rev. B **12**, 905–922 (1975).

[141] P. Szabó, P. Samuely, J. Kačmarčík, T. Klein, J. Marcus, D. Fruchart, S. Miraglia, C. Marcenat, and A. G. M. Jansen, *"Evidence for Two Superconducting Energy Gaps in* MgB_2 *by Point-Contact Spectroscopy"*, Phys. Rev. Lett. **87**, 137005 (2001).

[142] S. Tsuda, T. Yokoya, T. Kiss, Y. Takano, K. Togano, H. Kito, H. Ihara, and S. Shin, *"Evidence for a Multiple Superconducting Gap in* MgB_2 *from High-Resolution Photoemission Spectroscopy"*, Phys. Rev. Lett. **87**, 177006 (2001).

[143] K. Chen, W. Dai, C. G. Zhuang, Q. Li, S. Carabello, J. G. Lambert, J. T. Mlack, R. C. Ramos, and X. X. Xi, *"Momentum-dependent multiple gaps in magnesium diboride probed by electron tunnelling spectroscopy"*, Nature Communications **3**, 619 (2012).

[144] D. Mou, R. Jiang, V. Taufour, S. L. Bud'ko, P. C. Canfield, and A. Kaminski, *"Momentum dependence of the superconducting gap and in-gap states in* MgB_2 *multiband superconductor"*, Phys. Rev. B **91**, 214519 (2015).

[145] Y. Li, J. Hao, H. Liu, Y. Li, and Y. Ma, *"The metallization and superconductivity of dense hydrogen sulfide"*, The Journal of Chemical Physics **140**, 174712 (2014).

[146] D. Duan, Y. Liu, F. Tian, D. Li, X. Huang, Z. Zhao, H. Yu, B. Liu, W. Tian, and T. Cui, *"Pressure-induced metallization of dense* $(H_2S)_2H_2$ *with high-Tc superconductivity"*, Scientific Reports **4**, 6968 (2014).

[147] A. P. Drozdov, M. I. Eremets, I. A. Troyan, V. Ksenofontov, and S. I. Shylin, *"Conventional superconductivity at 203 kelvin at high pressures in the sulfur hydride system"*, Nature **525**, 73-76 (2015).

[148] J. A. Flores-Livas, L. Boeri, A. Sanna, G. Profeta, R. Arita, and M. Eremets, *"A perspective on conventional high-temperature superconductors at high pressure: Methods and materials"*, Physics Reports **856**, 1 - 78 (2020).

[149] C. J. Pickard, I. Errea, and M. I. Eremets, *"Superconducting Hydrides Under Pressure"*, Annual Review of Condensed Matter Physics **11**, 57-76 (2020).

[150] I. A. Troyan, D. V. Semenok, A. G. Kvashnin, A. V. Sadakov, O. A. Sobolevskiy, V. M. Pudalov, A. G. Ivanova, V. B. Prakapenka, E. Greenberg, A. G. Gavriliuk, V. V. Struzhkin, A. Bergara, I. Errea, R. Bianco, M. Calandra, F. Mauri, L. Monacelli, R. Akashi, and A. R. Oganov, *"Anomalous high-temperature superconductivity in* YH_6*"*, arXiv:1908.01534 .

[151] P. P. Kong, V. S. Minkov, M. A. Kuzovnikov, S. P. Besedin, A. P. Drozdov, S. Mozaffari, L. Balicas, F. F. Balakirev, V. B. Prakapenka, E. Greenberg, D. A. Knyazev, and M. I. Eremets, *"Superconductivity up to 243 K in yttrium hydrides under high pressure"*, arXiv:1909.10482 .

[152] Y. Li, J. Hao, H. Liu, J. S. Tse, Y. Wang, and Y. Ma, *"Pressure-stabilized superconductive yttrium hydrides"*, Scientific Reports **5**, 9948 (2015).

[153] F. Peng, Y. Sun, C. J. Pickard, R. J. Needs, Q. Wu, and Y. Ma, *"Hydrogen Clathrate Structures in Rare Earth Hydrides at High Pressures: Possible Route to Room-Temperature Superconductivity"*, Phys. Rev. Lett. **119**, 107001 (2017).

[154] C. Heil, S. di Cataldo, G. B. Bachelet, and L. Boeri, *"Superconductivity in sodalite-like yttrium hydride clathrates"*, Phys. Rev. B **99**, 220502 (2019).

[155] J. P. Perdew, K. Burke, and M. Ernzerhof, *"Generalized Gradient Approximation Made Simple"*, Phys. Rev. Lett. **77**, 3865–3868 (1996).

[156] C. Hartwigsen, S. Goedecker, and J. Hutter, *"Relativistic separable dual-space Gaussian pseudopotentials from H to Rn"*, Phys. Rev. B **58**, 3641–3662 (1998).

[157] S. Goedecker, M. Teter, and J. Hutter, *"Separable dual-space Gaussian pseudopotentials"*, Phys. Rev. B **54**, 1703–1710 (1996).

[158] I. G. Gurtubay, A. Iturbe-Beristain, and A. Eiguren, *"Magnetic oscillations induced by phonons in non-magnetic materials"*, Communications Physics **3**, 22 (2020).

[159] F. Caruso, H. Lambert, and F. Giustino, *"Band Structures of Plasmonic Polarons"*, Phys. Rev. Lett. **114**, 146404 (2015).

[160] A. Sanna, S. Pittalis, J. K. Dewhurst, M. Monni, S. Sharma, G. Ummarino, S. Massidda, and E. K. U. Gross, *"Phononic self-energy effects and superconductivity in CaC_6"*, Phys. Rev. B **85**, 184514 (2012).

[161] Y. Nambu, *"Quasi-Particles and Gauge Invariance in the Theory of Superconductivity"*, Phys. Rev. **117**, 648–663 (1960).

[162] L. P. Gor'kov, *"On the Energy Spectrum of Superconductors"*, Sov. Phys. JETP **7**, 505–508 (1957).

[163] P. Morel and P. W. Anderson, *"Calculation of the Superconducting State Parameters with Retarded Electron-Phonon Interaction"*, Phys. Rev. **125**, 1263–1271 (1962).